

# Optimized Crenellation Designs for Fatigue Life Improvement of Metallic Airframe Structures

Vom Promotionsausschuss der  
Technischen Universität Hamburg-Harburg  
zur Erlangung des akademischen Grades  
Doktor-Ingenieur (Dr.-Ing.)

genehmigte Dissertation

von  
Jin Lu

aus  
Henan, China

2017

1. Gutachter: Herr Prof. Norbert Huber
  2. Gutachter: Herr Prof. Peter Horst
- Vorsitzender des Prüfungsausschusses: Herr Prof. Sören Ehlers  
Tag der mündlichen Prüfung: 24.05.2017

## Acknowledgements

Firstly, I wish to present my special thanks to my supervisor: Prof. Norbert Huber for providing this precious opportunity of doctor study at Helmholtz-Zentrum Geesthacht and for his much valuable guidance and encouragement during the past four years of my doctor study. I also would like to show my deep gratitude to my second supervisor: Dr. Nikolai Kashaev. His advices, help and sympathetic attitude at every point during my research were a landmark effort towards the success of my project. I also would like to show my warm thanks to the second reviewer of my dissertation: Prof. Peter Horst, who provided very valuable feedbacks regarding my doctor thesis.

In addition, I would like to thank all those colleagues, whose assistance proved to be a milestone in the accomplishment of my doctor project. I would like to give my whole-heartedly appreciation to Jürgen Knaack and to Karl-Heinz Balzereit for their constant and unfailing technical support and assistance, without which it is impossible to accomplish this project. Their very nice personalities also made the experimental work become a much joyful process. In addition I also would like to thank Dr. Volker Ventzke for the precious support in the texture analysis and to thank Anne Groth for sharing the very valuable data of laser heating experiments. I also would like to give my warm thanks to Falk Dorn, René Dinse, Stefan Riekehr and Manfred Horstmann for their strong support in the specimen preparation and data processing, and to Dr. Ingo Scheider for his very patient help with the simulation work.

Thirdly, I am very grateful to Hans-Martin Bauschke, who shared the same office with me. His very nice, friendly and joyfull attitude made the ordinary work life in the office become one of my most cherished and unforgettable memories. I also would like to thank all the other colleagues in the WMF department. Thank you for your support and friendship during the four years of my doctor study. It was a great time working with all of you!

Last but not least, I would like to especially thank my parents and my wife Mengjia Zhang. Their selfless love and support are my essential energy source for accomplishing my doctor study.



# Abstract

Fatigue of airframe structures is a critical concern for the safety of aircraft. Serious accidents due to the accumulation of fatigue damages in airframes are by no means rare cases in history. Nowadays to ensure the structural integrity of the aircraft periodic inspections are performed on the airframe structure to detect and repair fatigue cracks timely. The prescribed inspection frequency is determined by the speed of fatigue crack growth from an initial detectable length to a maximum allowable length. Therefore, there is a constant driving force in the aerospace industry to improve the fatigue crack resistance of airframe structures by different techniques to reduce the inspection frequency and thus the maintenance cost yet without any compromise on the safety issue.

Crenellation is such a promising fatigue crack retardation concept developed in recent years, in which the thickness of the fuselage skin is systematically varied while the structural weight remains unchanged. The variation of the thickness modulates the stress intensity factor profile and provides the retardation on fatigue crack growth. In previous studies, crenellations were only investigated in simplified cases, that is under uniaxial loads, with unitary material and with a single crenellation design based on experience. However, in order to apply crenellations in practice, the following questions are still needed to be answered. Firstly, does the service-related biaxial load have additional effects on the fatigue crack retardation of crenellation? Secondly, will the efficiency of the crenellation be influenced by the different materials applied in the structure? Thirdly, how can the crenellation geometry be optimized to maximize the fatigue crack retardation effects?

To systematically address those questions, this work was organized into an experimental part and a simulation part. In the experimental part, a large biaxial testing facility was used to imitate the biaxial fuselage load due to repeated cabin pressurization among flights. Two different candidate Al alloys for fuselage skin (Al-Cu alloy AA2139 and Al-Li alloy AA2198) were applied for the fabrication of specimens. The grain structure and texture of those alloys were characterized beforehand. Then, flat and crenellated square panels made of each material were fatigued under the same loading condition, during which the crack closure behaviors were continuously monitored by a removable  $\delta_5$  clip gauge placed at crack tips. Finally, the fracture surfaces of each specimen were examined after the tests. It is found that the fatigue life improvement by crenellations is significantly higher in the sharply textured AA2198 compared to the randomly textured AA2139. This accompanies with elevated crack opening loads and an extensive formation of sharp shear lips on the fracture surfaces of AA2198 especially in the crenellated

specimen. The profiles of measured crack opening loads indicates that it is the wedging at the sharp shear lips that contributes to the enhanced crack opening load and thus to the prolonged fatigue life. Such wedging is found to be further promoted by the out of plane movements of crenellated specimen under biaxial loads.

In the simulation part, the FEM model of the experimental setup was firstly validated in terms of its capacity in fatigue life prediction based on the calculated driving force (the  $\Delta K$  profile). Then the FEM model was coupled with a genetic algorithm for the optimization of the crenellation geometry. An automated optimization loop was constructed, which starts with a population of randomly generated crenellation patterns. Each of them is represented by a binary string called genotype, according to which the FEM model of the crenellation design can be automatically generated. After evaluating the fatigue performance of each design by running FEM simulations, the genotypes that represent the best designs are then selected and recombined to form strings corresponding to potentially better designs in next generation. By using this approach, it is found that the crenellation design with progressive increase of panel thickness from the stringer root towards the center of the bay provides the largest fatigue crack retardation. Such a design was verified by using a multi-objective optimization approach and its effectiveness was validated in experiments. The same approach was also applied to optimize the combined application of crenellation and laser heating technique, which shows the optimized configuration can lead to much larger fatigue life extension compared to the summation of their individual effects.

In conclusion, the study suggests that, in order to maximize the fatigue crack retardation in a crenellated structure, Al-Li alloys with sharp deformation texture like AA2198 and crenellation patterns with a stepwise increase and then decrease of local thicknesses should be used. By combining crenellation with laser heating technique in an optimized way, pronounced additional fatigue life gain can be expected.

# Zusammenfassung

Die Materialermüdung einer Flugzeugzelle ist ein kritischer Bereich für die Sicherheit eines Flugzeugs. Schwere Unfälle aufgrund von akkumulierten Schäden, die auf Materialermüdung zurückzuführen sind, stellen keineswegs Einzelfälle in der Geschichte dar. Heutzutage werden zur Gewährleistung der strukturellen Integrität des Flugzeugs periodisch Inspektionen der Flugzeugzelle durchgeführt, so dass Ermüdungsrisse rechtzeitig gefunden und repariert werden können. Die angegebenen Inspektionsintervalle richten sich nach der Wachstumsgeschwindigkeit der Ermüdungsrisse, und zwar von einer anfänglich erkennbaren Länge bis hin zu einer maximal zulässigen Länge. Daher besteht in der Luftfahrtindustrie ein beständiges Bestreben, die Widerstandsfähigkeit gegen Ermüdungsrisse in Flugzeugzellen zu verbessern, und mittels verschiedener Techniken die Inspektionshäufigkeit zu reduzieren, was wiederum die Wartungskosten verringert, ohne dass dabei Kompromisse zulasten der Flugsicherheit eingegangen werden müssen.

Krenelierung ist ein derart vielversprechendes Konzept zur Verlangsamung der Rissbildung, das in den letzten Jahren entwickelt wurde. Hierbei wird die Dicke der Rumpfhaut systematisch variiert, wobei das Konstruktionsgewicht gleich bleibt. Die Variation der Schichtdicke moduliert das Profil des Spannungsintensitätsfaktors und bietet die gewünschte Verlangsamung im Ermüdungsrissswachstum. In früheren Studien wurden Krenelierungen nur in vereinfachten Lastfällen (unter axialen Lasten) untersucht, wobei einheitliches Material verwendet, und ein erfahrungsbasierter Einzel-Krenelierungsaufbau angewendet wurde. Um Krenelierungen jedoch praktisch umsetzen zu können, müssen immer noch die im folgenden aufgeführten Fragen beantwortet werden. Erstens: Hat die biaxiale Beanspruchung im Zusammenhang mit dem Betrieb zusätzliche Auswirkungen auf die Ermüdungsrisssverlangsamung bei der Krenelierung? Zweitens: Können die verschiedenen, in der Konstruktion verwendeten Materialien die Effizienz der Krenelierung beeinflussen? Drittens: Wie kann die Krenelierungsgeometrie optimiert werden, damit die Effekte der Ermüdungsrisssverlangsamung maximiert werden?

Um diese Fragen systematisch zu bearbeiten, wurde diese Arbeit in einen experimentellen Teil und einen Simulationsteil unterteilt. Im experimentellen Teil wurde eine große Testeinrichtung für biaxiale Belastung verwendet, um die biaxiale Rumpfbelastung aufgrund von wiederholter Kabinendruckbeaufschlagung während Flügen zu imitieren. Für die Rumpfhaut wurden zwei verschiedene Testanwärter Al-Legierung (Al-Cu-Legierung AA2139 und Al-Li-Legierung AA2198) für die Herstellung der Prüfmuster verwendet. Das Korngefüge und die Textur dieser Legierungen wurden im Vorfeld charakterisiert. Dann wurden flache und krenelierte, quadratische Platten von jedem der beiden Materialien unter densel-

ben Lastbedingungen der Ermüdung ausgesetzt. Während dieses Prozesses wurde das Riss-Schließverhalten permanent von einem  $\delta_5$ -Clip Messgerät überwacht, das an der Risspitze angesetzt wurde. Schließlich wurden die Bruchoberflächen eines jeden Prüfmusters nach den Tests untersucht. Dabei stellte sich heraus, dass die Verbesserung der Ermüdungslebensdauer durch Krenelierungen bei dem stark strukturierten AA2198 im Vergleich zu dem wahllos strukturierten AA2139 erheblich höher ist. Das geht einher mit erhöhten Rissöffnungsbelastungen und einer extensiven Bildung von scharfkantigen Scherlippen auf den Bruchoberflächen bei AA2198, besonders bei dem krenelierten Prüfmuster. Die Profile der gemessenen Rissöffnungsbelastungen zeigen an, dass es die Verkantung bei den scharfen Scherlippen ist, die zu der erhöhten Rissöffnungsbelastung beiträgt, und somit auch zu längerer Lebensdauer. Des Weiteren stellte sich heraus, dass eine derartige Verkeilung noch stärker bei dem krenelierten Prüfmuster bei Bewegung außerhalb der Ebene unter biaxialer Belastung stattfand.

Im Simulationsteil, wurde das FEM-Modell des Versuchsaufbaus zunächst bezüglich seiner Kapazität in der Lebensdauervorhersage basierend auf der errechneten Triebkraft (das  $\Delta K$  -Profil) validiert. Dann wird das FEM-Modell mit einem genetischen Algorithmus zur Optimierung der Krenelierungsgeometrie gekoppelt. Es wird eine automatische Optimierungsschleife erzeugt, die mit einer Gesamtheit von zufällig erzeugten Krenelierungsmustern beginnt. Jedes davon wird von einem Binär-String genannt Genotyp repräsentiert, nach dem das FEM-Modell des Krenelierungsaufbaus automatisch erzeugt werden kann. Nach Auswertung des Ermüdungsverhaltens eines jeden Aufbaus durch Ausführung von FEM-Simulationen, werden dann die Genotypen ausgewählt, die den besten Aufbau darstellen, und neu kombiniert. So werden Strings gebildet, die dem potenziell besseren Aufbau in der nächsten Generation entsprechen. Durch Verwendung dieses Ansatzes wurde festgestellt, dass der Krenelierungsaufbau mit einem progressiven Anstieg der Plattendicke von der Stringer-Wurzel zum Joch-Zentrum die höchste Ermüdungsrissverlangsamung bietet. Ein derartiger Aufbau wurde mittels Verwendung eines mehrdimensionalen Optimierungsansatzes verifiziert, und seine Effizienz wurde mit Experimenten validiert. Derselbe Ansatz wurde auch zur Optimierung der kombinierten Anwendung von Krenelierung und Lasererwärmungstechnik angewendet, was zeigt, dass die optimierte Konfiguration im Vergleich zur Summierung ihrer Einzeleffekte zu einer erheblichen Verlängerung der Lebensdauer führen kann.

Zusammenfassend legt diese Studie nahe, dass zur Maximierung der Ermüdungsrissverlangsamung in einer krenelierten Struktur, Al-Li-Legierungen mit scharfkantiger Verformungstextur wie AA2198, und Krenelierungsmuster mit einem stufenweisen Anstieg und dann Reduzierung der örtlichen Dicke verwendet werden sollten. Durch optimiertes Kombinieren von Krenelierung mit Lasererwärmung, kann ein deutlicher, zusätzlicher Lebensdauergewinn erwartet werden.

# Contents

<b>1</b>	<b>Introduction</b>	<b>1</b>
1.1	Motivation . . . . .	1
1.2	Approaches . . . . .	3
1.3	Structure of the thesis . . . . .	4
<b>2</b>	<b>Theoretical Background</b>	<b>7</b>
2.1	Fatigue as a phenomenon in metals . . . . .	7
2.1.1	Fatigue crack initiation . . . . .	7
2.1.2	Propagation of long fatigue cracks . . . . .	11
2.1.3	Crack closure and its influence on fatigue crack growth . . .	16
	Plasticity induced crack closure (PICC) . . . . .	17
	Roughness induced crack closure (RICC) . . . . .	19
2.1.4	Influence of residual stresses on fatigue crack growth . . . .	21
	Origin of residual stresses in metallic structures . . . . .	21
	Fatigue crack growth in presence of residual stress field . . .	23
2.2	Optimization using genetic algorithm (GA) . . . . .	24
2.2.1	Brief introduction to GA . . . . .	24
2.2.2	The working principle of GA . . . . .	26
2.2.3	Choose suitable representation for GA . . . . .	30
2.2.4	Extension of GA to solve multiple objective optimizations .	32
	Fitness assignment scheme of NSGA-II . . . . .	33
	Elitist strategy of NSGA-II . . . . .	34
<b>3</b>	<b>Experimental</b>	<b>37</b>
3.1	Materials . . . . .	37
3.2	Microstructure and texture characterization . . . . .	37
3.3	Biaxial fatigue tests and FEM modeling of the experimen- tal setup . . . . .	37
3.4	Measurements of crack closure level . . . . .	40
3.5	Fracture surface observation . . . . .	41
<b>4</b>	<b>Influence of materials on the crenellation efficiency</b>	<b>43</b>

4.1	Results . . . . .	43
4.1.1	Microstructure and Texture . . . . .	43
4.1.2	Fatigue crack growth tests . . . . .	43
4.1.3	Fracture surface observation . . . . .	48
4.1.4	Observations on the deformation state of the panels under biaxial loads . . . . .	52
4.2	Discussion . . . . .	52
4.2.1	Influences of texture on the shear lip formation . . . . .	52
4.2.2	Influences of shear lips on the crack growth behavior . . . . .	57
4.2.3	The technical significance of sliding crack closure at shear lips in comparison with roughness induced crack closure . . . . .	59
4.3	Summary of this chapter . . . . .	62
<b>5</b>	<b>Optimization of crenellation geometry via genetic algorithm</b>	<b>63</b>
5.1	Validation of the FEM model used for fatigue life prediction	64
5.2	Implementation of the genetic algorithm in the present optimization problem . . . . .	66
5.2.1	Description of the optimization problem . . . . .	66
5.2.2	Encoding scheme . . . . .	66
5.2.3	Progressive refinement of the search space . . . . .	67
5.2.4	GA parameters used in the optimization . . . . .	67
5.2.5	The organization of the optimization process . . . . .	68
5.3	Optimization results . . . . .	69
5.4	Reviewing about the computational cost . . . . .	73
5.5	Verification and validation of the approach . . . . .	75
5.6	Optimizing the combination of crenellation with laser heating techniques . . . . .	78
5.6.1	Including residual stress field of laser heating in the FEM model . . . . .	78
5.6.2	Implementation of GA in the present optimization problem . . . . .	84
5.6.3	Results of the optimization . . . . .	87
5.7	Summary and suggestions for the FEM-GA coupled opti- mizations . . . . .	92
<b>6</b>	<b>Conclusion</b>	<b>97</b>
	<b>Appendix A Python scripts for the FEM-GA coupled optimization</b>	<b>99</b>

A.1 main.py . . . . .	99
A.2 grow.py . . . . .	108
A.3 k_values.py . . . . .	112
<b>Bibliography</b>	<b>115</b>



# 1. Introduction

## 1.1 Motivation

Fatigue is one of the utmost important concerns in the design of airframe structures. Statistics show that about 60% of failures in aircraft components are caused by fatigue damages [1]. The evolution of such damages encompasses two stages. Firstly, the fatigue cracks nucleate at defects or in highly stress-concentrated regions of airframe structures, which is actually an unavoidable process considering the long service life of the aircraft and normally can hardly be detected through non-destructive inspection procedures. Then the initiated fatigue cracks continue to grow into a macroscopic size under various service loads until the final failure occurs. Those macroscopic cracks, such as the ones initiated from rivet holes in fuselage skin, can be detected and repaired timely through a maintenance procedure. Thus, to safeguard the structural integrity of the aircraft, the damage tolerance approach is usually adopted. This approach permits the existence of fatigue damages to a certain extent and requires periodic inspections on the airframe structures to detect and to repair those small cracks before they grow into a threat to the safety of the aircraft. The growth speed of these cracks from a detectable size up to a maximum allowable size determines the necessary inspection frequency and the operational cost of the aircraft [2]. Therefore, there is a constant economic driving force to apply various approaches to retard the possible fatigue crack growth in service as much as possible.

In recent years the concept of crenellation has been proposed as a very promising local engineering technique in fuselage skin [3–8], which can improve the fatigue resistance of the structure without introducing extra weight. Compared to some other fatigue crack retardation techniques like the bonded crack retarders [9], which add up additional material to the structure, the crenellation concept is considered to be more advantageous from the point of view of light-weighted design and thus the reduction in fuel consumption of the aircraft.

As shown in Figure 1.1 a and b, in this concept systematic thickness variations are introduced in the fuselage skin, where the mass variation in the thickened and thinned areas counterbalances each other. Such thickness variations modulate the driving force for fatigue crack growth, that is, the stress intensity factor ranges  $\Delta K$  (as shown in Figure 1.1 c), which introduces retardation and acceleration regions of fatigue crack growth with respect to the uncrenellated structure. In a well-designed crenellation, the fatigue life gain in the retardation region is always much larger than the fatigue life loss in the acceleration region, which leads to an overall fatigue life improvement. This has been theoretically proved through

mathematic derivation by Uz in [7]. The actual effectiveness of the crenellation concept in fatigue life improvement has also been experimentally demonstrated with uniaxial fatigue tests both under constant amplitude loading and spectrum loading [7, 10].

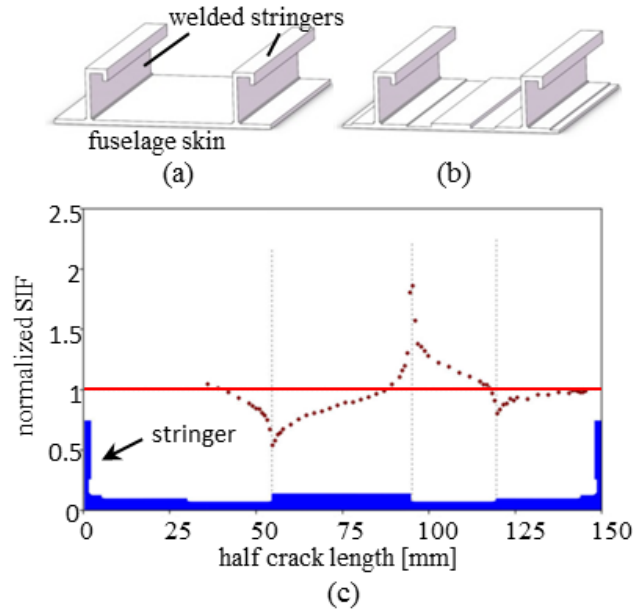


Figure 1.1. (a) Flat and (b) crenellated structure with the same weight, (c) stress intensity factor (SIF) profile of a through-thickness crack in crenellated stiffened panel normalized to the SIF values of a reference panel (continuous line) with the same structural weight (after [7]).

However, there are still several limitations in the aforementioned studies on crenellations.

Firstly the crenellation concept was only investigated under uniaxial loading conditions while in practice the fuselage skins are under more complex biaxial loads. For example, the repeated cabin pressurization among flights, which is considered as one major source of multiple site damage [11], leads to a typical biaxial stress state in fuselage skin with the stress in the hoop direction roughly 2 times of that in the axial direction [12]. So far it is still unknown if the more practical biaxial loading condition has some additional influences on the fatigue crack retardation in comparison with the uniaxial loading case.

In addition, besides the geometrical modification introduced by crenellation, the fatigue behavior of the material itself is another essential influence on the overall fatigue performance of the structure. With the development of new Al alloys with superior specific strength and damage tolerant behavior [13, 14], it is expected that future airframe structures will switch to those more advanced alloy systems for the purpose of reducing structural weight and maintenance cost. Therefore, it is essential to investigate if the change of materials in use can influence the effectiveness of the crenellation concept as well as to gain an in-depth understanding about which type of material is perhaps most beneficial to be applied together

with crenellations. However, so far this information is still missing in the previous studies.

Thirdly, since the modulation of  $\Delta K$  profiles as shown in Figure 1.1 c depends on the crenellation geometry, it is possible to maximize the resulting fatigue crack retardations by performing geometric optimizations of crenellation patterns. However, the previous study in this aspect is rather limited. Although Uz et al. have performed geometric optimizations based on artificial neural network (ANN) and FEM simulations [15], this method is computationally expensive due to the large number of simulations for achieving a good training quality of ANN. In addition, the optimization was performed under a restricted frame of a crenellation design with several of its dimensions as design variables. The lack of flexibility in defining crenellation geometries can potentially prevent from discovering the true design optimum.

Therefore the present study is aimed at the following objectives:

1. to testify the performance of the crenellation concept in fatigue crack growth life improvement under the service-related biaxial loading condition.
2. to investigate possible influences of materials on the effectiveness of crenellation.
3. to establish a flexible and efficient approach to optimize the crenellation geometry for the maximization of fatigue crack retardation.

## 1.2 Approaches

The aims mentioned above have been addressed by using a combined approach incorporating both experimental and numerical studies.

In the part of experimental study, the service-related loading condition is achieved by using a biaxial testing facility. The applied load is adjusted so that the stress level and biaxial stress ratio can well reflect the fuselage load due to repeated cabin pressurization and depressurization in a typical commercial airliner.

To examine the influence of materials on the crenellation efficiency two newly developed candidate alloys for fuselage skin, namely AA2139 and AA2198, are chosen. The two materials have close chemical compositions for most alloying elements. But there is one significant difference that AA2198 has about 1% addition of lithium in order to enhance the stiffness (by about 6%) and to reduce the density (by about 3%) [16]. AA2139 does not contain lithium at all but has a slightly higher Ag content for improving the weldability. The different alloy designs are also associated with different heat treatments (T3 for AA2198 and T351 for AA2139), which lead to distinct microstructural characteristics in terms of grain structure and texture. Such a significant intrinsic difference can have distinct impact on the fatigue life extension when the crenellation concept is applied.

In order to accurately capture the response of the specimens with different materials under the prescribed loading condition for the correct interpretation of the observed fatigue behaviors, a comprehensive monitoring of specimens was performed throughout the fatigue tests which took place at two different scales. At a global scale, the deformation state of the specimen was recorded by strain gauges

attached on specific positions of the specimen surface to verify if the aimed loading condition is achieved in the experiments. The measured strain gauge values also form the important database for the validation of FEM model in the subsequent numerical study. At a local scale the instantaneous displacements of the two crack surfaces near a crack tip were tracked by a modified removable  $\delta_5$  clip gauge, the aim of which is to probe the crack closure behavior during the cyclic loading.

The observed anomaly in fatigue crack growth rate and the profile of crack closure level are then correlated with the corresponding local morphology on the fracture surface after the fatigue tests, which help to achieve a comprehensive understanding about the observed fatigue behavior.

In the simulation part, FEM models of the experimental setup are established to calculate the nominal driving force for crack growth, namely the  $\Delta K$ , for all tested specimens. Based on that, one can get the theoretical estimation of the fatigue life improvement achieved by crenellation. To ensure the accuracy of the  $\Delta K$  calculation, the FEM models are firstly validated by using the strain gauge values measured from experiments. Then FEM model is also validated in terms of the accuracy in predicting the impact of geometrical modifications (crenellations) on the fatigue performance of the specimens. These validation steps form the foundation of the subsequent optimization step, which is purely based on FEM simulation.

In order to obtain the optimum or quasi-optimum crenellation design in a more efficient and reliable way, an automated optimization approach is developed, which couples FEM simulations with a genetic algorithm. This approach requires the encoding of each potential crenellation design with a series of binary code, which returns the optimized designs also in the form of binary code. In order to ensure that all the evolved designs of crenellation patterns have the same structural weight a constraint handling technique is developed. The application of such a technique is subsequently verified that it has no negative effects on arriving at the global or quasi-global optimum. To validate the its effectiveness the optimized design is also experimentally tested in terms of its fatigue performance. The required computational efficiency of this approach is also optimized by combining two different techniques for the reduction of the computational cost. Finally, the FEM-GA coupled approach is further performed on the optimization problem when the laser heating technique is combined into the crenellated structures with the aim of pushing the limit of fatigue life improvement that has been attained.

### 1.3 Structure of the thesis

In the following chapters, the thesis starts with a theoretical background for this study (chapter 2), which includes the most important phenomena in the fatigue of metallic structures as well as the optimization techniques that will be used. In chapter 3, the materials used for producing in specimens and the experimental procedures of this work are to be explained in detail. Chapter 4 is devoted to the experimental observations on the fatigue testing of specimens with two different alloys and to the examination on their fracture surfaces after tests. Discussions concerning the implications of the experimental results are present in the second half of the chapter. In chapter 5, a FEM-GA coupled optimization approach is

---

firstly introduced. After presenting the major optimization results, a brief discussion is made about the related computational cost. Then a verification of the applied technique for handling the constant-weight constraint and an experimental validation of the effectiveness of the optimization are provided. The chapter ends with a tentative study on the optimization of combinations between crenellation and laser heating technique. The key findings of this study are summarized in the concluding chapter (chapter 6). At the end of the thesis, the reader can also find the computer code developed in this study to perform the FEM-GA optimization, which is provided as Appendix.



## 2. Theoretical Background

### 2.1 Fatigue as a phenomenon in metals

The fatigue damage in metallic structures like in airframes originates from the irreversible cyclic slips that occur at a stress level far below the yield stress. The phenomenon starts with fatigue crack nucleation normally at the surface or at the inclusion sites near the surface, which is followed by a transient stage of microcrack growth and then the subsequent propagation of long cracks.

The fatigue crack nucleation and microcrack growth are more closely correlated with each other due to the fact that both of them are strongly affected by plane stress condition near the surface and local microstructural barriers. Therefore both stages together are generally termed as the period of fatigue crack initiation according to Schijve [17]. In contrast, the propagation of long cracks in most cases is hardly affected by either of the two factors. The behavior of the fatigue cracks of this stage mainly reflects the bulk properties of the materials.

Such a difference is strongly related with different characteristics of dislocation motions in each stage. This will be explained in more detail in following subsections on the stage of fatigue crack initiation and fatigue crack growth respectively.

After introducing the two stages of fatigue life, two special topics about the crack closure phenomenon and the residual stress in metallic structures, which has a big influence on the growth of long fatigue cracks, will be additionally discussed.

#### 2.1.1 Fatigue crack initiation

The accumulation of fatigue damage starts at stress levels much lower than the yield stress. Under such stresses microplasticity can occur in grains located at the free surface, where the plane stress condition prevails. This is because at the free surface the material is only present on the one side, which, compared to the interior of the material, exerts much less constraint on dislocation slips and the material flows especially in the direction out of the surface plane. At the microscale, the shear stress, which results in the microplasticity, is not homogeneously distributed but varies from grain to grain depending the shapes of the grains, their crystallographic orientation, the elastic anisotropic of the material and the presence of microscopic discontinuities like inclusions and pores.

As a result, the cyclic slip required for the fatigue crack nucleation is most probable to occur in surface grains with the highest shear stress level, which meanwhile have the best alignment between their easy sliding planes (i.e. the  $\{111\}$  planes of Al alloy) and the maximum shear stress plane (normally  $45^\circ$  inclined with the loading axis). As show in Figure 2.1, once slip occurs in one grain upon loading,

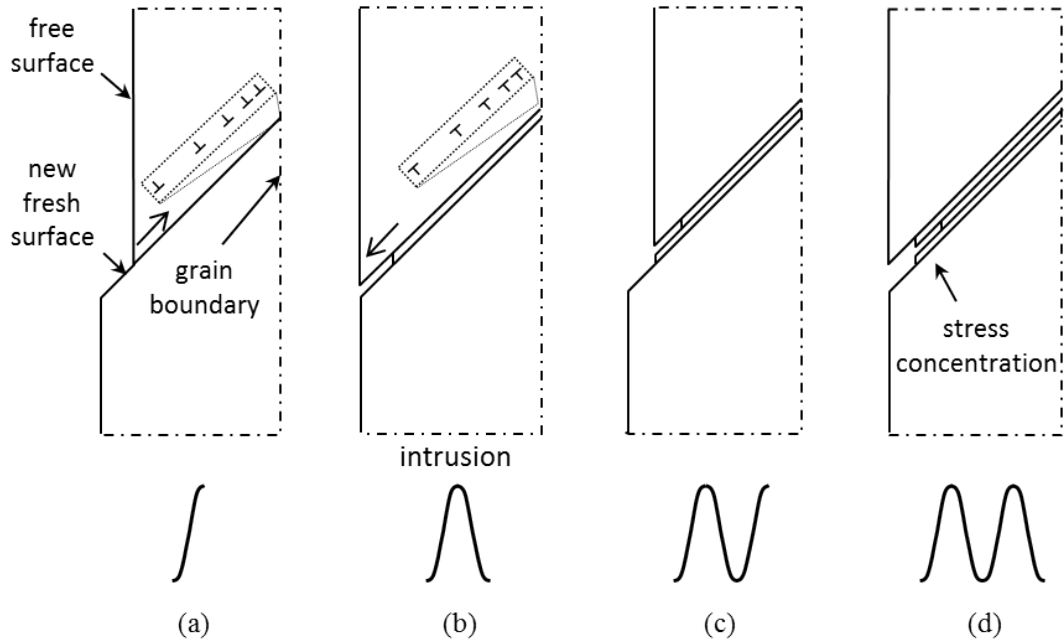


Figure 2.1. Cyclic slips lead to fatigue crack nucleation at the surface (after [17]).

a slip step will appear on the free surface as the outcome of series of dislocation motion along the slip band. The newly created fresh surface will be immediately covered by an oxide layer for metallic materials in most environments. During unloading, the pile-up of the dislocations that multiplied on the previous slip plane will result in a large shear stress along the same plane but in the reverse direction. However, the slip of those dislocations can not be fully reversed along the same slip plane due to the presence of the oxide monolayer at the slip step and due to the formation of obstacles to dislocation motions such as dislocation jogs [18]. As a result, the reversed slip takes place in the adjacent slip plane as marked by a series of dislocations with opposite Burgers vector in Figure 2.1 b, which creates an intrusion on the free surface. The intrusion functions as a micro-notch, which leads to stress concentration in the local area and promotes further penetration of the decohesion in the same slip band in subsequent load cycles. In this way a fatigue crack nucleates from the free surface.

The aforementioned mechanism means the speed of the fatigue crack initiation is governed by the magnitude of the plastic strain localized in the surface slip bands, which, according to [19], can be formulated as follows:

$$\gamma_p = r(1 - \nu) \frac{L}{h} \left(1 + \frac{L}{h}\right)^2 \frac{0.5\sigma - \tau_{crs}}{G} \quad (2.1)$$

where  $L$  is the length of the slip band, which usually takes the value of the grain size,  $r=1.9$ ,  $\nu$  is the Poisson's ratio,  $h$  is the thickness of the slip band,  $G$  is the shear modulus,  $\sigma$  is the applied stress (assuming a homogeneous stress distribution through the material) and  $\tau_{crs}$  is the critical resolved shear stress. The factor of 0.5 in front of  $\sigma$  comes from the highest possible Schmid factor where the slip band is  $45^\circ$  inclined to the loading axis. Since normally  $L/h \gg 1$  (in the order of 200

according to Pokluda [19]) the plastic strain can be considered to be proportional to the aspect ratio of slip bands as well as to the grain size. This equation implies that the nucleation of a fatigue crack is most probable in the largest surface grains, which have slip planes with the largest Schmid factor.

At a larger scale beyond those microstructural influences, the local stress concentration in the structure by various stress raisers plays a key role in the initiation of fatigue damage, which can multiply the applied stress  $\sigma$  in equation 2.1 locally by several times. For instance, in airframe structures, the fatigue cracks were frequently found to initiate from rivet holes and sharp corners of frames [12,20]. The root radius of notches is considered to be the most important variable for the level of stress concentration [17]. The surface roughness is also a significant influence on the nucleation of fatigue cracks, since the irregularities on a coarse surface can be considered as many micro notches that have sharp root radii [17].

After nucleation, the initial growth of the formed microcrack occurs along the same slip band in shear mode, which is also called stage I fatigue crack growth. The mechanism of the crack propagation in this stage is schematically shown using a single-slip model in Figure 2.2. In the first half load cycle, a series of edge dislocations are emitted from the crack tip along the direction of crack propagation, which leads to a shear displacement between the two crack flanks and creates a fresh surface on one flank of the crack (the lower one in Figure 2.2). The length of the new flank equals the number of dislocations times the Burgers vector. Upon unloading, the same amount of edge dislocations with the same Burgers vector return to the crack tip and generate a fresh surface on the other crack flank. At this stage, since the fatigue crack growth requires only single slip along the cracking plane, a very flat and featureless fracture surface is produced.

When the crack tip is approaching a microstructural barrier, such as a grain boundary, the emission of dislocations from crack tip and their further motion are greatly restrained. Thus a significant drop of crack growth rate is observed at the grain boundaries as observed by Blom et al. [21] in Al alloys.

At low stress levels, the formed microcracks can even be fully arrested in front of those barriers although their nucleation is not a problem under such stresses. Those cracks are also called non-propagation cracks [17] (see Figure 2.3). If only non-propagating cracks appear in the material, further cyclic loading will not lead to the failure. Thus the fatigue limit of material <sup>1</sup> should correspond to the stress under which the longest microcracks remain arrested [19]. The maximum size of those non-propagating cracks is determined by the spacing of the strongest barriers [19]. Thus the high strength alloys with finer microstructure is often observed to have a higher fatigue limit as well.

If the applied stress is above the fatigue limit, the surface cracks will penetrate the microstructural barriers like grain boundaries and grows deeper into the material. After the crack penetrates one or two grains, due to the increased constraints of neighbouring grains and the diminishing plane stress condition it becomes increasingly difficult to accommodate the shear displacement brought by the single slip on only one slip plane as depicted in Figure 2.2. Thus, slips on multiple slip

---

<sup>1</sup>Fatigue limit is the stress level, under which the material is assumed to have a quasi-infinite fatigue life.

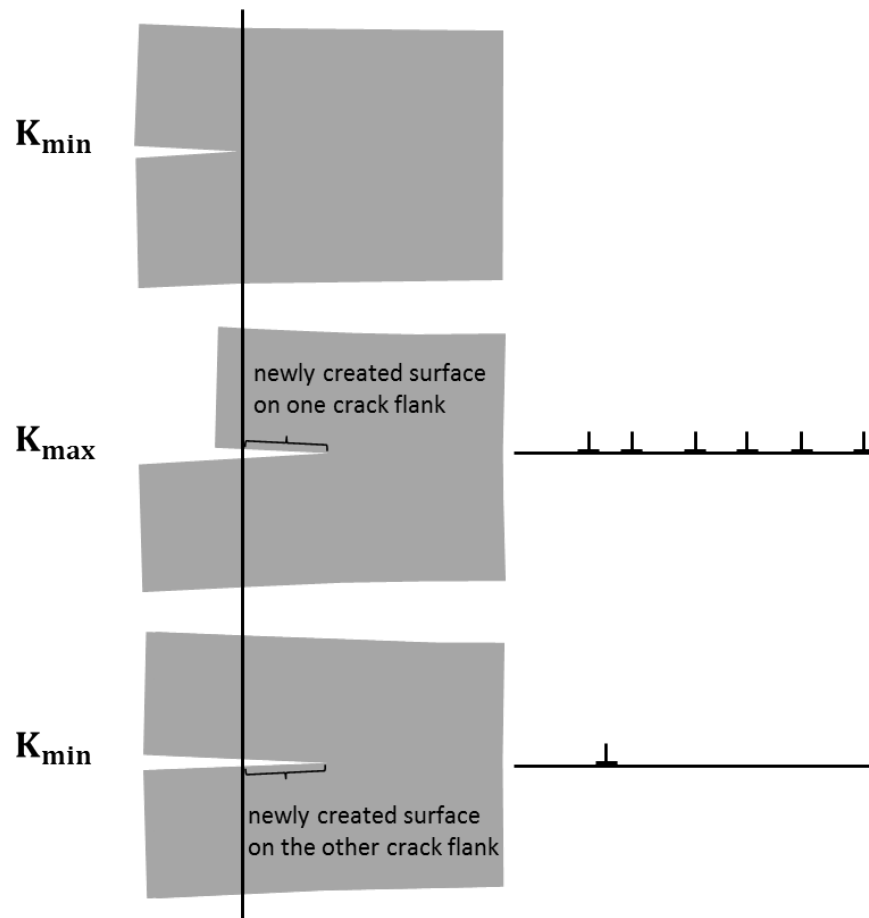


Figure 2.2. The single-slip model of stage I crack propagation (after [19]).

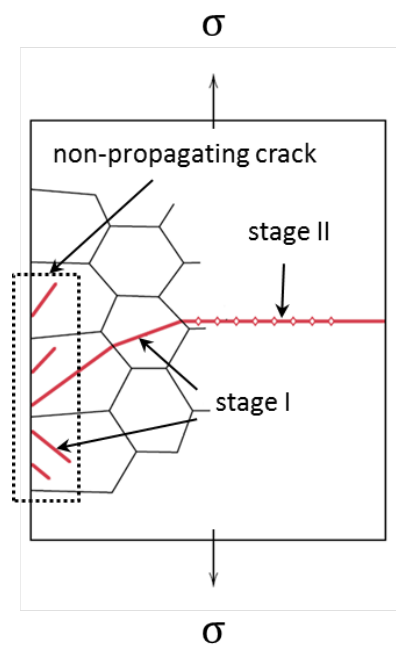


Figure 2.3. Arresting of microcracks at grain boundaries and the transition from stage I growth to stage II growth of a microcrack.

planes are required. In such a case, the microcrack begins to deviate from the initial direction along slip bands and becomes perpendicular to the loading axis (Figure 2.3), where the applied tensile stress can provide the largest driving force for crack growth.

With further increase of the crack size, when both the crack front and the plastically deformed region at crack tip, namely the plastic zone (see section 2.1.2), can envelop many different grains, the microcrack turns into a microstructurally long crack, the growth of which is hardly affected by discrete microstructural inhomogeneties but depends on the fatigue crack growth resistance of bulk material. The propagation of long crack occurs mostly in a stage II fashion, which is characterized by formation of striations on the fracture surface and a cracking plane perpendicular to the load axis as shown in Figure 2.3.

Although the nucleation and the very slow growth of a microcrack can take up the major part of the whole fatigue life [17], at this stage the initiated cracks remain invisible under various nondestructive inspection methods used in the maintenance of airliners. Thus the propagation of long cracks is of more technical importance for the damage tolerant design concept of airframe structures, which will be described in detail in the following section.

### 2.1.2 Propagation of long fatigue cracks

As mentioned in the previous section, the propagation of long cracks requires dislocation motion on multiple slip planes, which results in a macroscopic propagation direction perpendicular to the applied tensile load. The major growth mechanism at this stage can be schematically represented in Figure 2.4. As it can be seen for each load cycle that, the opening of the crack during uploading is accompanied with the blunting of crack tip, which comes from the motion of two symmetrical sets of dislocations with respect to the cracking plane. Those dislocations are emitted from the crack tip and slide along the two symmetrical planes with maximum shear stresses, which produces a shear on each flank of crack tip. At the same time the crack tip extends by a distance of  $\Delta a$  as shown in Figure 2.4. Upon unloading, the crack does not extend but a resharpening of crack tip occurs, which is due to the reverse slip of dislocations on the aforementioned two planes. However, since the previous shear deformation cannot be fully reversed due to mechanisms like strain hardening, a ridge of microplastic deformation is left on each flank of the crack. As the fatigue crack extends incrementally cycle by cycle, periodic patterns are produced on both crack surfaces as shown in Figure 2.5. Those patterns are called "striations", which are characteristic features of stage II fatigue crack growth.

The plastic deformation at the crack tip is actually not only confined to the two narrow stripes of slip for crack tip blunting as depicted in Figure 2.5, but also occurs in a much broader region as long as the local stress at the crack tip is high enough to cause the yielding of the material. The detailed shape of the plastic zone can be obtained by using finite element analysis of the cracked body with elastic-plastic material models [23]. As shown in Figure 2.6 the plastic zone of a tensile mode crack has a butterfly shape with its two "wings" symmetrical to the cracking plane. The shape and size of each wing depend on the stress state (plane

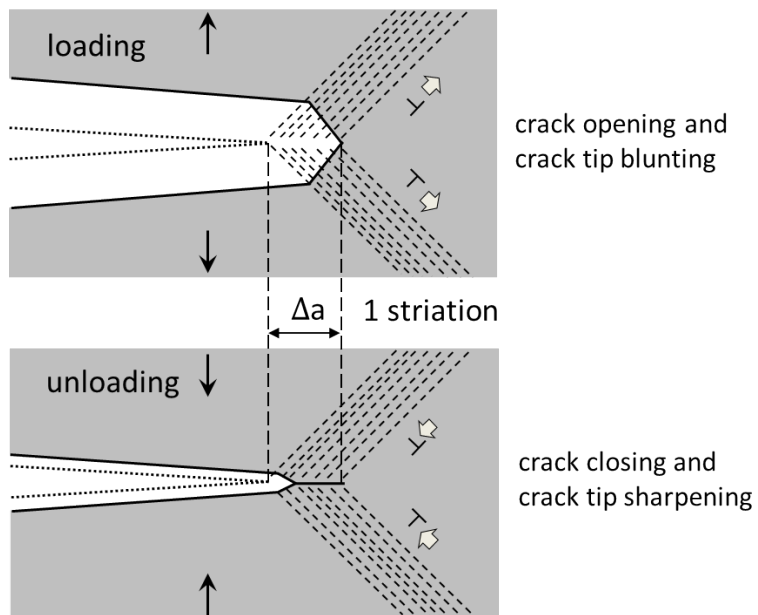


Figure 2.4. The model of stage II crack propagation (after [17]).

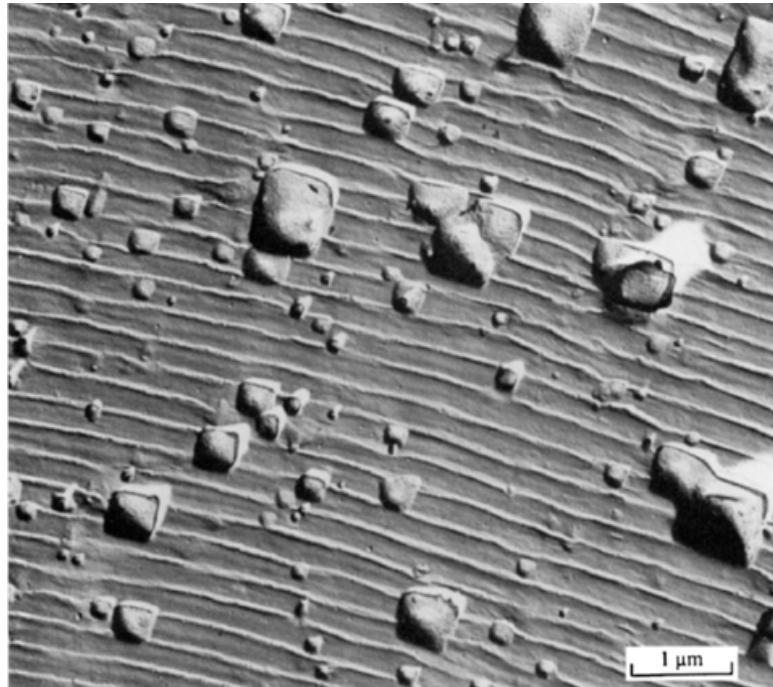


Figure 2.5. Fatigue striations on the etched failure surface in 2024-T3 aluminum alloy. (From [22]. Copyright ASM International. Reprinted with permission.)

stress or plane strain) and the strain hardening rate of the material, besides its yield stress.

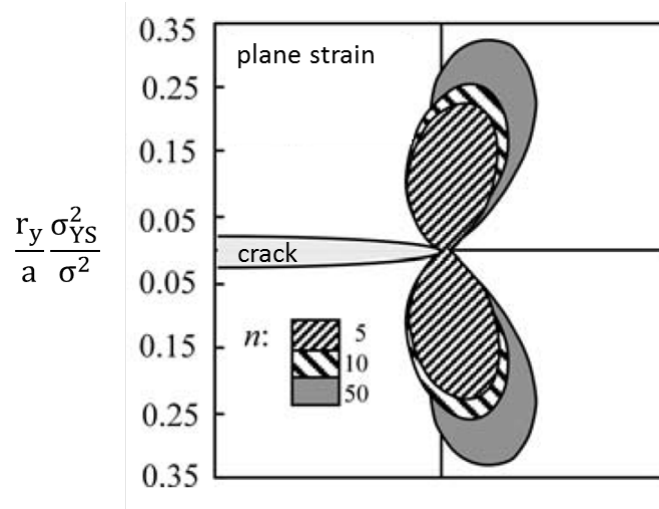


Figure 2.6. Shapes of plastic zones of a tensile mode crack in materials with different strain hardening rates (after [24]).

The cyclic plastic zone developed at the crack tip is essential for the fatigue crack propagation behavior, since the driving force of the fatigue crack growth is directly related with the range of cyclic plastic strain evolved at the crack tip [19]. However, to successfully estimate the growth rate of a long fatigue crack, it is ordinarily not necessary to adopt specialized elastic-plastic parameters for the characterization of the crack tip plasticity. In most cases the stress intensity factor  $K$ , which measures the severity of the stress distribution around the crack tip purely based on elasticity of the cracked body, can already well fulfill this aim. The range of stress intensity factor  $\Delta K$  ( $\Delta K = K_{\max} - K_{\min}$ ,  $K_{\max}$  and  $K_{\min}$  are the stress intensity factor at maximum and minimum load) during cyclic loading can be considered as the driving force of fatigue crack growth, which shows very good correspondence with the fatigue crack propagation rate as firstly found by Paris et al. [25, 26]. Their discoveries further led to the well-known principle of similarity. It states that if the same  $K$ -cycle (the same  $K_{\max}$  and  $K_{\min}$ ) is applied to cracks in the same material, the same growth rates will be expected irrespective of the size of the fatigue crack and the geometry of the cracked body. Thus, the fatigue crack growth rate in a metal can be considered as a function of the two parameters:

$$\frac{da}{dN} = f(K_{\max}, K_{\min}) \quad (2.2)$$

$K_{\max}$  and  $K_{\min}$  in the above equation can be expressed in terms of the range of stress intensity factor  $\Delta K$  ( $K_{\max} - K_{\min}$ ) and the load ratio  $R$  ( $K_{\min}/K_{\max}$ ). If  $R$  is kept constant,  $da/dN$  becomes the a function of  $\Delta K$  alone:

$$\frac{da}{dN} = f_R(\Delta K) \quad (2.3)$$

This relation forms nowadays the foundation of predicting long fatigue crack growth behavior in practice, based on the experimental data from laboratory. It should be noted, the  $da/dN$ - $\Delta K$  correlation of long fatigue cracks show much smaller scattering compared to microcracks [27, 28]. This is because the growth of the propagation of long fatigue cracks mainly reflects the macroscopic crack resistance of material, whereas the growth of microcracks is very sensitive to microstructural inhomogenities.

The successful correlation between the elastic parameter  $K$  with the fatigue crack growth rate lies in the fact that the size of plastic zone at the tip of a long crack is normally much smaller than the crack itself. Under such small-scale yielding condition [24], the formation of plastic zone leads to negligible stress redistribution in the  $K$ -dominated zone at the crack tip compared to the idealized model without plasticity.  $K$  is thus considered to uniquely characterize the crack tip conditions including the crack tip plasticity. This is because that, under the same severity of stress distribution as prescribed by  $K$ , the same plastic zone will be evolved near crack tip for the same material. It has been theoretically justified by Rice [29] that the small-scale cyclic crack tip plasticity that leads to fatigue crack growth is indeed controlled by the value of  $\Delta K$ .

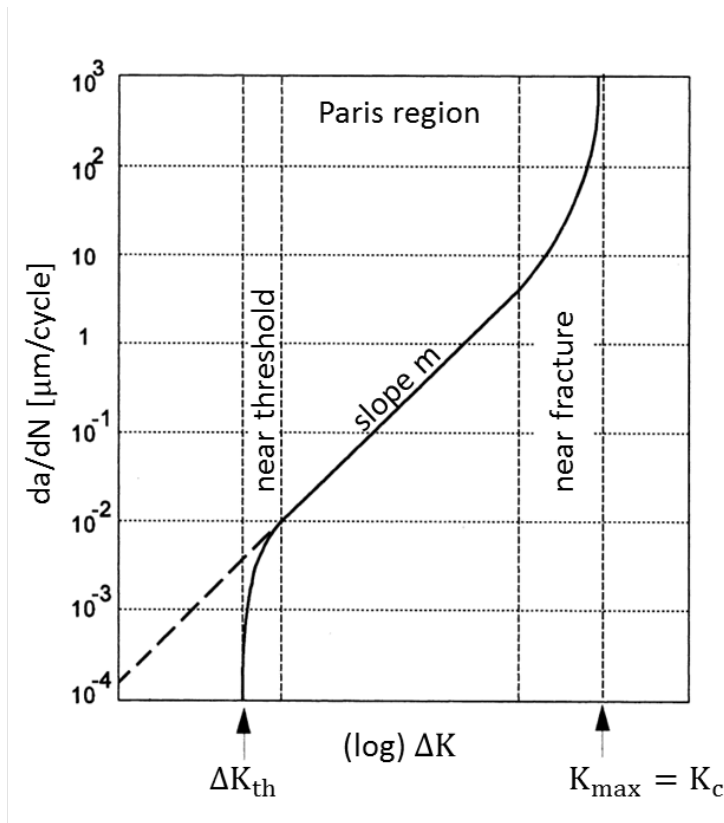


Figure 2.7. Schematic sketch of the three regions of  $da/dN$  versus  $\Delta K$  dependence for long fatigue cracks (after [19]).

With increasing  $\Delta K$ , the  $da/dN$  versus  $\Delta K$  dependence of long cracks shows a sigmoidal variation as schematically depicted in Figure 2.7, which can be divided into three regions: near threshold region, Paris region and near-fracture region.

At the lower extreme of  $\Delta K$  values is the near threshold region. In this region the averaged fatigue crack extension per cycle is normally smaller than the atomic spacing. The fatigue crack growth mechanism is also somewhat different from the model described in the beginning of the section, which will be explained in detail in section 2.1.3. When  $\Delta K$  decreases to  $\Delta K_{th}$ , the fatigue crack is considered to be stationary. At the other extreme is the near fracture region, where the  $K_{max}$  is close to the fracture toughness of the material  $Kc$ . The fatigue crack growth rate in this region is very high and the crack is found to propagate in a locally tearing fashion [17].

The Paris region has the broadest span covering the majority part of the  $\Delta K$  range in Figure 2.7. In this region,  $da/dN$  shows a linear dependence on  $\Delta K$  under double logarithm, which can be described by a power function, namely the Paris Law [26]:

$$\frac{da}{dN} = C\Delta K^m \quad (2.4)$$

where  $C$  and  $m$  are material dependent constants on the precondition that the load ratio  $R$  remains the same. The Paris region is of the greatest technical significance, since in most cases the growth of long fatigue cracks falls into this region. In addition, the Paris law provides a powerful tool for making a quantitative estimation about the long fatigue crack growth. Since the  $\Delta K$  values of a cyclically loaded cracked body with arbitrary geometry can be reliably obtained by using the finite element method, the growth rate of long cracks (under constant amplitude loads) can be predicted by equation 2.4 with rather satisfying accuracy based on material constants obtained from experiments.

However, the application of equation 2.4 assumes the load ratio  $R$  should be the same as the tests for fitting the Paris constants. Actually  $R$  is a significant influence on the fatigue behavior, which is not taken into account by the Paris equation. As shown in Figure 2.8, with increasing  $R$ , the whole  $da/dN$ - $\Delta K$  curve tends to move towards lower  $\Delta K$  ranges. The main reason of this shift will be explained in the section 2.1.3. To further consider the influence of  $R$  different empirical crack laws have been developed as an extension of the Paris law. The Walker equation [30] is such an empirical law with a rather simple form:

$$\frac{da}{dN} = C(\Delta K(1-R)^{n-1})^m \quad (2.5)$$

where there is an additional material constant  $n$  that needs to be obtained from experiments.

For Al alloys, the fatigue crack growth behavior in Paris region can be complicated by the formation of shear lips on the fracture surface [31–33]. As shown in Figure 2.9 shear lips are the slant regions of crack surface (mostly  $45^\circ$  inclined) where the tensile mode decohesion is replaced by the shear mode. Either single or double shear lips can occur at the surface, where the plane-stress state is dominant. After initiation they are broadened towards the center until a stable shear lip width  $t_s$  is achieved (if  $t_s$  is larger than half of the panel thickness, the whole fracture surface becomes slant). The formation of shear lips is found closely related with plane stress condition at crack tip, which is thus more pronounced

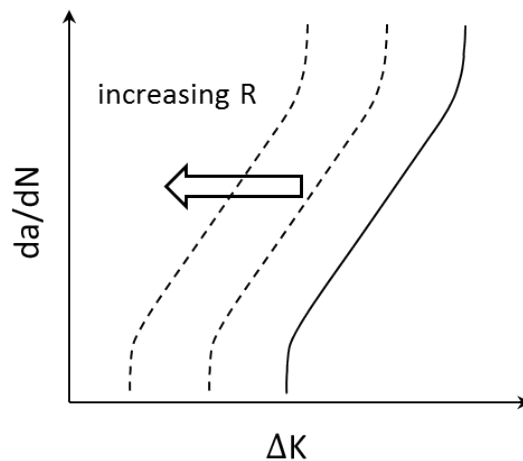


Figure 2.8. Effect of load ratio  $R$  on the fatigue crack propagation rate.

on the fracture surface of thin panels. In addition, the initiation of shear lips on fracture surface was found to entail a minimal fatigue crack growth rate [31].

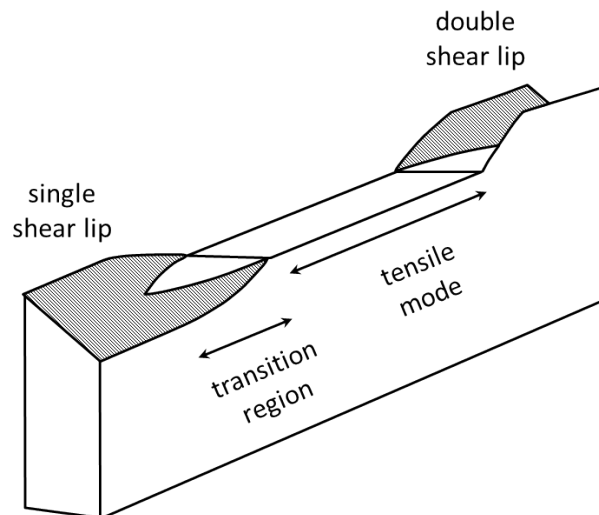


Figure 2.9. Formation of shear lips on the fracture surface (after [32]).

For fatigue crack propagation behavior, the formation of shear lips was found to affect the linearity of the  $da/dN$ - $\Delta K$  curve in the Paris region [32], where the local changes of slopes can be associated with the change in fracture surface morphology. Since shear lips are usually the highest points of fracture surfaces, which can promote the wedging of crack surfaces, the slope changes are very likely to be related with changes of the crack closure behavior, the definition of which will be specified in the following section.

### 2.1.3 Crack closure and its influence on fatigue crack growth

The phenomenon of crack closure was firstly discovered by Elber [34] in the sixties of last century. He found in the unloading phase of the fatigue test that,

far before the applied tensile load was reduced to zero the crack tip was already closed. Since the fatigue crack extension only occurs during the stage of crack tip blunting when the crack tip opens (see section 2.1.2), the range of  $\Delta K$  from  $K_{\min}$  to  $K_{\text{open}}$  (the nominal stress intensity factor at the opening load) does not contribute to the driving force for crack extension. Therefore the effective range of the stress intensity factor  $\Delta K_{\text{eff}}$  is actually from  $K_{\text{open}}$  up to  $K_{\max}$  as depicted in Figure 2.10.

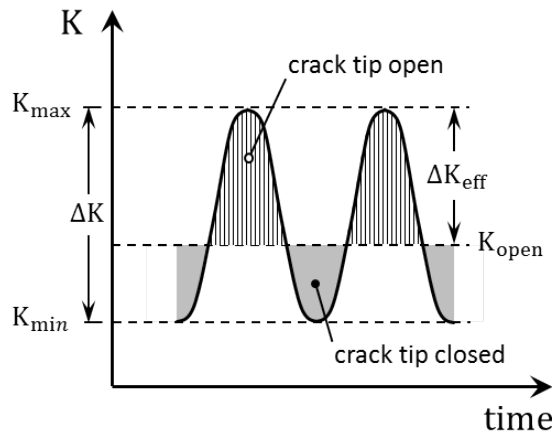


Figure 2.10. The effective range of stress intensity factor due to the presence of crack closure (after [17]).

The shift of  $da/dN$ - $\Delta K$  curves towards lower  $\Delta K$  values with increasing  $R$  as mentioned in the previous section can be explained by the crack closure phenomenon. Considering the case when  $R$  increases but  $\Delta K$  remains constant,  $K_{\max}$  and  $K_{\min}$  would increase with the same amplitude. As it can be seen from Figure 2.10, in such a case if  $K_{\text{open}}$  is assumed to be constant  $\Delta K_{\text{eff}}$  will increase with  $R$  until  $K_{\min}$  is larger than  $K_{\text{open}}$ . Thus, with increasing  $R$ , to attain the same fatigue crack growth rate a smaller  $\Delta K$  would be required. It was also experimentally proved that if the crack closure effect is taken into account by applying the effective range of stress intensity factor  $\Delta K_{\text{eff}}$ , the data points for different  $R$  values will collapse into the same scatter band as prescribed by Paris law [17].

The crack closure can occur with many different mechanisms. Among them plasticity induced crack closure and roughness induced crack closure are two mechanisms that have the major influence on the fatigue crack growth in Al alloys, which will be explained in detail in following paragraphs.

### Plasticity induced crack closure (PICC)

Plastic induced crack closure is an outcome of the cyclic plastic deformation at the crack tip. As mentioned in section 2.1.2 during the uploading phase, a plastic zone develops at the crack tip. The highly concentrated tensile stress at the crack front elongates the material in the plastic zone in the direction perpendicular to the cracking plane. During the unloading phase, since the plastic zone is extended in the loading axis, a compression load will be developed within it. This causes a smaller zone with reverse plastic deformation as shown in Figure 2.11. According

to Schijve [17], the size of the reverse plastic zone is in the order of 1/4 of the plastic zone evolved in the loading phase. Since the majority area of plastic zone outside the zone of reversed plasticity is under monotonic tension as indicated by Figure 2.11 residual plastic deformation is left in this region with permanent elongation along the loading axis. The residual plastic deformation also accumulates cycle by cycle as the crack is growing through the plastic zone of previous cycles. Finally, a field of plastic wake is left, which wraps the crack tip and the two crack flanks. The permanent elongation in the plastic wake provides a combined contact and zone shielding according to Richie [35], which is the origin of PICC.

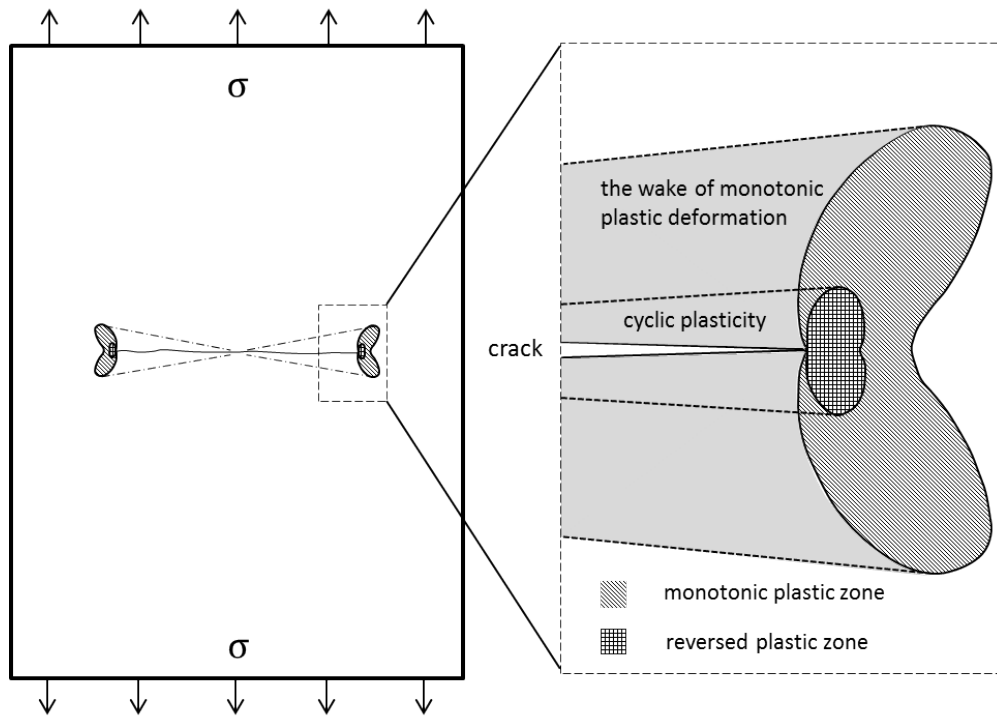


Figure 2.11. Schematic sketch of the plastic wake with residual elongation in the loading direction left behind a growing crack tip (after [17]).

For the condition of constant amplitude loading, the crack closure level due to PICC is considered to be a rather stable parameter, which is insensitive of materials [19]. However, it can be influenced by the stress state (plane stress/strain) at the crack tip and the cyclic load ratio  $R$ . It was found PICC is most pronounced under plane stress condition [36] and under low  $R$  values.

In addition, if overload cycles are applied, an increased crack closure level can be observed afterwards, the influence of which will then gradually diminish in the subsequent several millimeters of fatigue crack growth. The transient increase of crack closure level comes from the enhanced PICC due to the larger plastic zone size of the overload cycle. The accompanied fatigue crack retardation after overloads is one important reason of the load history effects in fatigue under variable-amplitude loading.

### Roughness induced crack closure (RICC)

The roughness induced crack closure [12], as its name implies, is due to the premature contact on the asperities of rough fracture surfaces. For precipitate hardened Al alloys, it commonly occurs in the underaged state, where the planar slip is promoted due to the coherent and shearable precipitates. In contrast with PICC, which plays a major role in the middle and high  $\Delta K$  range in Paris region, the roughness induced crack closure becomes dominating in low  $\Delta K$  ranges especially in the near-threshold region, where the maximum plastic zone size is smaller than the dimension of grain diameter. In such a case restraints on cyclic slips due to the presence of grain boundaries are much reduced, which promotes fatigue crack propagation by a single shear mechanism (much like the stage I fatigue crack growth as mentioned in section 2.1.1) along the most advantageous slip system [12]. As a result, the fatigue cracks in the near threshold region usually show serrated or zig-zag paths [37,38] (Figure 2.12) as well as facet-like asperities on the fracture surfaces. Due to the different crystallographic orientations among grains. The size of those asperities were found to depend on the grain size [39–41], which can range from several micrometers to hundreds of micrometers [38]. Besides grain boundaries, phase boundaries such as those of pearlites in steels can play the same role in resulting in the rough and facet-like fracture surface in near threshold region [41].

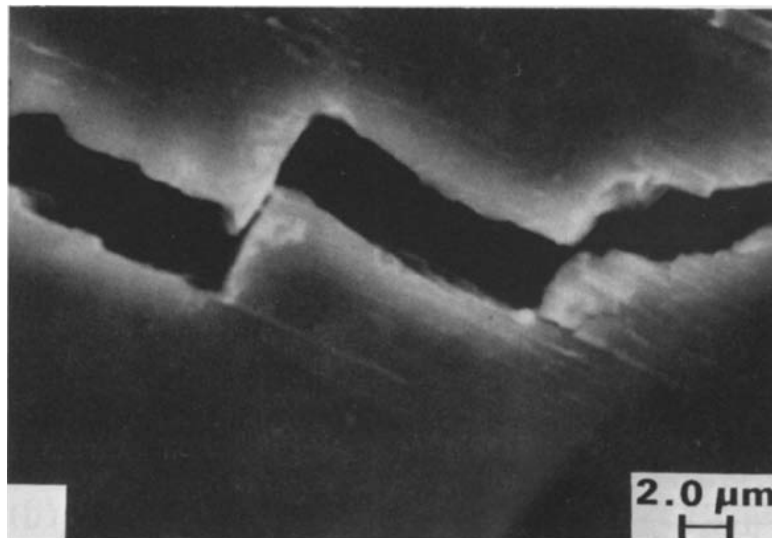


Figure 2.12. Zig-zag crack path morphology in Al-Li alloy 2090-T8E41. The fracture surface contact on asperities promotes roughness induced crack closure. (From [35]. Copyright Elsevier. Reprinted with permission.)

The wedging mechanism of RICC on the aforementioned asperities can be described by the simplified 2 dimensional model as sketched in Figure 2.13, where the asperities due to the zig-zag crack path are idealized to be of triangle cross sections with equal size. In the unloading phase, a relative shear displacement between the two crack surfaces occurs. The resulting mismatch leads to premature surface contact when the crack flanks are still wedged open by a normal displacement  $\delta_{c1}$ . Given the small crack opening in the near-threshold region,  $\delta_{c1}$  can be a

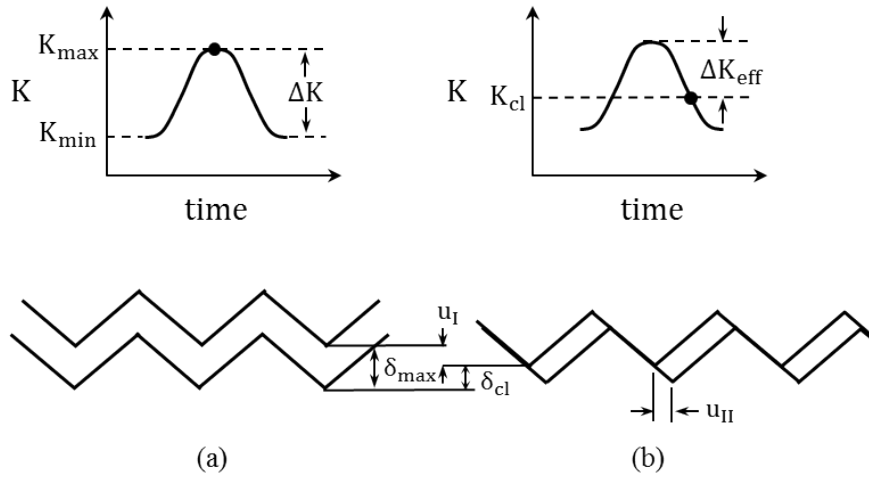


Figure 2.13. Simplified 2 dimensional model illustrating the mechanism of RICC. (a) The position of crack flanks at the maximum load. (b) The position of crack flanks when crack closure occurs.  $\delta_{\max}$  and  $\delta_{cl}$  are the crack opening displacements at the maximum load and at the crack opening load respectively,  $u_I$  and  $u_{II}$  are the mode I and mode II displacements of crack flanks at the crack opening load compared to the case of maximum load. (after [37])

considerable fraction of the maximum crack tip opening displacement  $\delta_{\max}$ , which indicates a pronounced crack closure phenomenon.

The residual shear displacement that is essential for RICC is traditionally considered to result from the slip irreversibility at the crack tip [12] and from the single shear mechanism of crack extension. However, Pippan et al. [42] points out that the asymmetric arrangement of geometrically necessary dislocation in the crack wake can also lead to asymmetric displacements of the two crack surfaces. In contrast with the prior mechanism, such a crack surface mismatch is considered to be long-ranged and thus can explain the crack closure that occurs at a distance from the crack tip.

Based on this simplified model, the closure stress intensity factor at the point of asperity contact can be derived [37]:

$$K_{cl} = K_{\max} \left( \frac{2\gamma X}{1 + 2\gamma X} \right)^{1/2} \quad (2.6)$$

where  $\gamma$  is a measure of roughness on the fracture surface and  $X$  is the ratio of mode II to mode I crack tip displacements ( $u_{II}/u_I$  in Figure 2.13). Although the aforementioned model is only a first-order approximation, equation 2.6 agrees reasonably well with experimental observations in a range of ferrous and non-ferrous alloys. From the equation it can be seen that the extent of RICC is determined both by the degree of the fracture surface roughness and by the magnitude of the relative shear displacement of the crack surfaces.

This can explain the frequently observed phenomenon that the near-threshold

fatigue crack growth rates in alloys with coarse grain structures are normally much lower compared to alloys with fine microstructure. This is because the larger grain sizes lead to more pronounced deflections along the serrated crack path, which in turn increase the roughness on the fracture surface. On the other hand, according to Pippan et al. [42] the long-range mismatch of crack surfaces due to the asymmetric crack wake plasticity also increases with the grain size. Based on the two points and equation 2.6, it can be expected that RICC is much enhanced in the coarse-grained materials. However, it should be noted the improved near-threshold fatigue performance by a coarse grain structure usually accompanies with a reduced fatigue limit, since the maximum size of the non-propagating fatigue crack is confined within grain size as mentioned in section 2.1.1.

Besides the grain size, the propensity of planar slip in the material is another significant impact on the extent of RICC. Take aluminium-lithium (Al-Li) alloys as an example, the shearable nature of the coherent strengthening phase  $\delta'$  ( $\text{Al}_3\text{Li}$ ) leads to strong tendency of planar slip and intense slip band formation in the materials. This is considered as the origin of its exceptionally rough fracture surfaces of the fatigue crack. Since the  $\text{Al}_3\text{Li}$  precipitates remain coherent even in the peak-aged conditions [43], slip planarity still prevails at those tempers. As a result, crystallographically tortuous fatigue crack paths and significant RICC can still be observed in artificially aged Al-Li alloys [44] with peak strength, which are normally inhibited at the same temper in other Al alloys due to the presence of semi- or incoherent hardening phases.

In addition, Al-Li alloys are usually used in the form of cold rolled plate in practical applications. The sharp deformation texture can further enhance the slip planarity. This is because the small misorientations between adjacent grains make grain boundaries weak obstacles for the development of slip bands. The slip-band fatigue cracking can easily penetrate different grains along quasi-straight path with nearly no deflections [45]. This results in extreme fracture surface tortuosity with asperities size much larger than the mean grain size [43, 46–48], which can still produce significant wedging at relatively large cyclic crack tip openings with increasing  $\Delta K$ . It was also found, due to the enhanced slip planarity, the fracture surface tortuosity can be preserved at large  $\Delta K$  values well above the threshold region [43, 47]. As a result, the crack tip shielding due to RICC can be extended to middle and even high  $\Delta K$  ranges in those alloys, where the crystallographically rough crack path should have already been replaced by the flat mode I crack path.

Therefore, the strong tendency of planar slip of Al-Li alloys leads to much enhanced RICC under different ageing states and in a broader  $\Delta K$  range compared to conventional Al alloys. The resulting superior resistance to long fatigue crack growth combined with their lower density and higher elastic modulus make Al-Li alloys very attractive materials for airframe applications.

## 2.1.4 Influence of residual stresses on fatigue crack growth

### Origin of residual stresses in metallic structures

Besides the crack closure another significant influence on the fatigue crack growth in metallic structures is the presence of residual stress field [17]. By def-

initiation, it is the stress distribution that remains in the structure even when no external load is applied. The source of residual stresses in metallic structures is the residue of inhomogeneous plastic deformation left in the structure, which can be introduced by various mechanical and thermal processes.

For instance, considering the uniaxial tension of a panel with a center notch at a moderate load as shown in Figure 2.14 a, yielding only occur in the small region at the root of the notch, where the concentrated local stress ( $K_t\sigma$ ,  $K_t$ : stress concentration factor) is higher than the yield stress of the material ( $\sigma_{0.2}$ ). Upon unloading since the majority part of the panel remains elastic, the whole structure tends to return its original geometry. However, the plastically stretched material in the plastic zone has a certain residual elongation in the direction of tension. The geometric mismatch between the plastic zone and its surrounding in the unloaded state leads to a compressive stress distribution inside the plastic zone and a tensile stress distribution in its ambient areas as shown in Figure 2.14 b, which enforces the geometric compatibility between the two parts. In this way, the residual stresses are developed after the load cycle. The tensile residual stresses and compressive residual stresses always occur in pairs in the structure, which balance with each other.

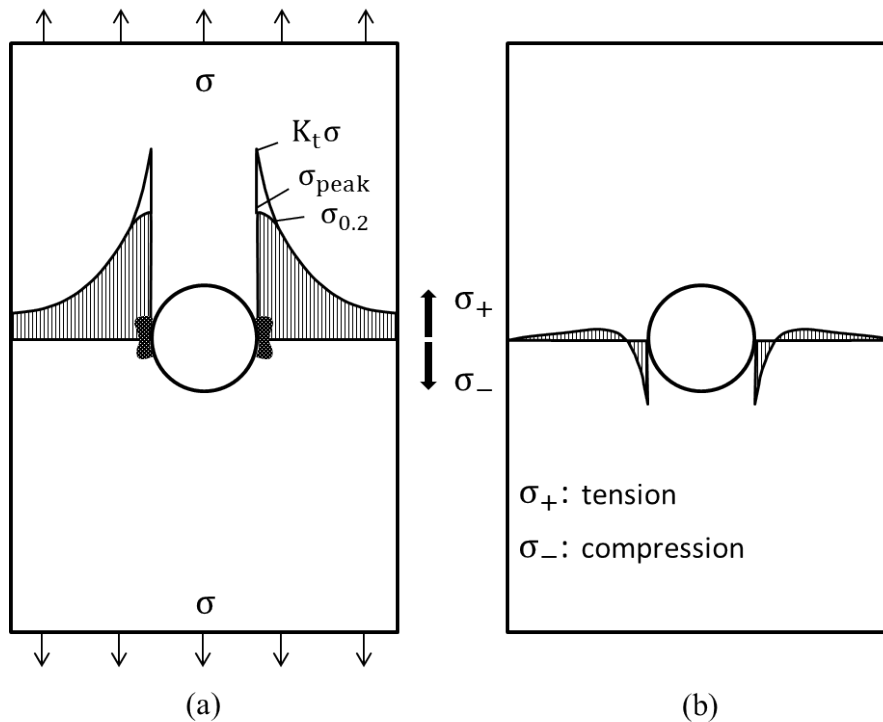


Figure 2.14. (a) Stress distribution in a center notched specimen under tensile load. (b) Residual stress distribution developed after unloading. (after [17])

Similarly, the inhomogeneous plastic deformation can also be introduced by a thermal cycle with sufficient temperature gradient in the structure (e.g. by the welding process). During the thermal cycle, compressive thermal stresses are firstly developed in the regions with the highest transient temperatures due to

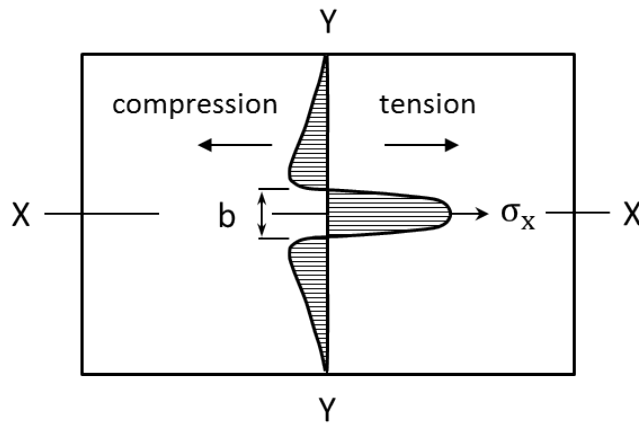


Figure 2.15. Schematic sketch of the residual stress profile developed after the welding process. The welding line is situated on the X axis.  $b$  is the width of the stripe that contains the residue compressive plastic deformation after the thermal cycle of welding (after [49]).

their relatively larger thermal expansions, which are confined by ambient materials with lower temperatures. Since the yield strengths of metallic metals can be much reduced at elevated temperatures, local yielding can occur under such compressive thermal stresses. After the thermal cycle, since the yielded region has been plastically compressed in a certain dimension, it needs to be stretched to keep the geometrical compatibility with its surroundings. As a result, tensile residual stresses need to be developed in this region, which are balanced by the compressive residual stresses in ambient areas. Figure 2.15 schematically shows the residual stress field evolved during a welding process, the development of which follows the general principle described above.

### Fatigue crack growth in presence of residual stress field

Residual stress field alone does not constitute to the nominal driving force for fatigue crack growth. However, it can significantly modify the effective driving force resulting from the externally applied cyclic stresses. The response of a cracked body under both the residual stress field and the applied stress field follows the rule of linear superposition as long as the material is within the elastic range. Thus, the maximum and minimum of the effective cyclic stresses, which drives the fatigue crack growth, can be written as:

$$\sigma_{\text{eff, max}} = \sigma_{\text{external load, max}} + \sigma_{\text{residual}}$$

$$\sigma_{\text{eff, min}} = \sigma_{\text{external load, min}} + \sigma_{\text{residual}}$$

It can be seen that the introduction of a residual stress field does not change the range of the cyclic stresses. However, it changes the mean value. If the local residual stress is positive, the enhanced stress level tends to open the non-propagating microcracks in an intact structure or to open the macrocracks in a cracked body, which leads either to a lower fatigue limit or to a shorter fatigue

crack growth life respectively. In contrary, if the crack is present in compressive residual stresses, the smaller crack opening will lead to a higher fatigue limit and to a longer fatigue life.

Therefore, by properly introducing compressive residual stress in specific regions, the fatigue performance of the structure can be potentially improved. There are several different techniques to introduce beneficial residual stresses in metals [50]. Based on the magnitudes of introduced compressive stresses and the affecting phases of fatigue life, they can be generally divided into the two categories, which will be detailed in following paragraphs.

If the introduced local compressive residual stress is very large it is possible that the crack is still closed under the maximum external load, that is  $\sigma_{\text{eff, max}} < 0$ . In such a case, although the cyclic stress range is none zero, no fatigue crack growth is possible. This phenomenon has been utilized by the techniques of plastic hole expansion and shot peening. In both processes, the surface layer of the material is plastically stretched, either along the surface of the hole by pulling a tapered pin through the undersized hole or along the peened surface by the impact of high speed shots. Consequently, very high compressive residual stresses develop within this surface layer. As the mentioned in beginning of the section, fatigue cracks mainly initiate from the surface. The purposely introduced compressive residual stress in those processes thus can effectively inhibit the fatigue crack initiation either from rivet holes or from the shot peened component surfaces.

With moderate compressive residual stress, it is possible that  $\sigma_{\text{eff, max}}$  is still positive whereas  $\sigma_{\text{eff, min}}$  becomes negative. In such a case, the effective stress range for fatigue crack growth  $\Delta\sigma_{\text{eff}}$  is actually from 0 up to  $\sigma_{\text{eff, max}}$ . Although the fatigue crack can further propagate, its growth rate is reduced in presence of compressive residual stress field due to the reduction of  $\Delta\sigma_{\text{eff}}$ . For long crack growth, since the governing Paris law is a strong power law (the Paris constant  $m$  normally lies between 2 and 4 [12]), even a moderate decrease in the amplitude of cyclic stress can lead to pronounced reduction of fatigue crack growth rate. Thus, if long crack grows continuously in the field of compressive stress significant retardations can be achieved. Laser heating [51, 52] is such a technique, which utilizes the widely spreaded compressive residual stress field surrounding the heating line to retard the growth of long fatigue cracks in airframe structure. This technique will be discussed in more detail in section 5.6.

## 2.2 Optimization using genetic algorithm (GA)

### 2.2.1 Brief introduction to GA

Genetic algorithm is a robust optimization technique mimicking the species evolution process in nature, which shows high performance in a wide spectrum of problems [53–55]. It is especially capable of coping with complex fitness landscapes (high dimensional, multimodal, discrete), where conventional methods usually fail. Compared to the gradient-based methods, it is easier to be implemented without any need of derivative information. In addition, as a global optimizer it is unlikely to get stuck in a local optimum as gradient-based methods do.

The strategies of nature to evolve highly fit species can be generalized into four

aspects:

1. Population-based: the evolution process takes place based on a population of the species.
2. Encoding: all the properties or characteristics of each individual in the population are encoded in the set of its chromosomes that contain the genetic information.
3. Natural selection: the fitter individuals have larger chance to survive and thus are able to produce more offspring. Less fit individuals will have less or no offspring.
4. Reproduction: it includes both processes of crossover and mutation. Crossover is the recombination of the genetic material of parent chromosomes to form the chromosomes of offspring, which enables them to inherit good traits from both parents. Mutation is a small and random change of a genetic information in the chromosomes of a offspring at low rates, which can introduce new traits that belongs to neither of its parents.

In following paragraphs, the canonical GA (binary encoding, single point crossover and bit flipping mutation) is used as an example to show the application of these four strategies in the optimization technique.

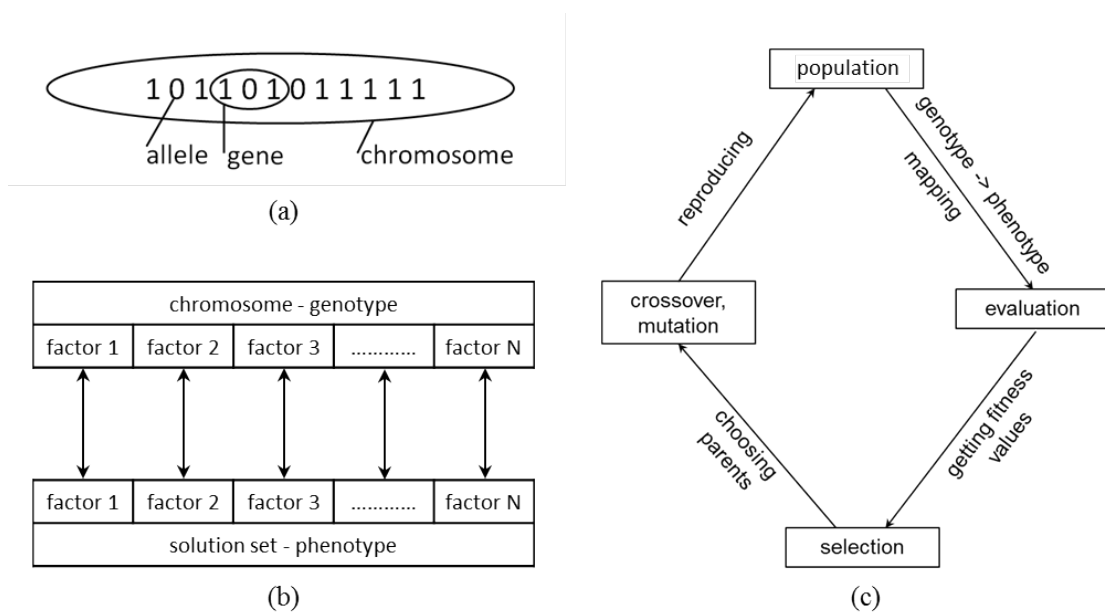


Figure 2.16. (a) Schematic sketch of the genotype of an individual (after [56]). (b) Mapping from genotype to phenotype (after [57]). (c) The loop of the optimization process based on genetic algorithm.

Firstly, GA works on a population of candidate solutions. Each candidate solution is represented by a code (usually a binary string), which is considered as the chromosome or the genotype of the solution. As shown in Figure 2.16 a, each digit

in the genotype is called an allele. Several alleles form a gene that can be decoded into a specific part (e.g. a parameter) of the solution (Figure 2.16 b). The solution itself is also called the phenotype. As shown in Figure 2.16 a, the optimization starts with a population of randomly generated genotypes. After mapping them into the corresponding phenotypes, each solution is evaluated on its success in solving the problem and is assigned with a fitness value accordingly. In the following selection step, the genotypes of the solutions with higher fitness values are selected to form a mating pool. The most frequently used selection schemes are roulette wheel selection and tournament selection. In the roulette wheel selection scheme, the possibility of an individual being selected for reproduction is proportional to its fitness. In the tournament selection scheme, a prescribed number of individuals (normally 2) are randomly chosen from the population to form a tournament, the winner of which will enter the mating pool. The aforementioned selection procedures are performed repeatedly until the mating pool is full.

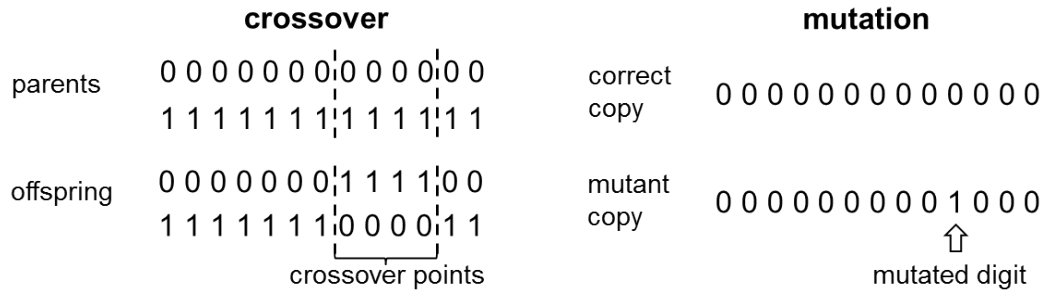


Figure 2.17. Schematic illustration of the crossover and mutation process in GA.

In the reproduction step, the process of crossover - the partial swapping of genetic information (Figure 2.17 a) - takes place with a prescribed probability (crossover rate) among the randomly formed pairs of genotypes in mating pool. Then the mutation occurs at a much lower probability (0.001-0.05) among all the newly formed genotypes, which is simply a bit flipping for the case of binary representation as shown in Figure 2.17 b. After the reproduction, a new population is formed for the next round of evaluation and selection. This process runs in loops, during which better and better solutions are evolved.

## 2.2.2 The working principle of GA

The high performance of GA in a wide spectrum of problems has attracted numerous previous researchers in the past four decades to perform rigorous analysis on its functioning mechanism. Nowadays it is generally accepted that GA works by exploiting the similarities among the solutions. The ability of GA to evolve better solutions is based on the association of the observed high fitness in population with those similarities. The representation of solutions by their corresponding genotypes is just for the purpose of comparison among different solutions. For example, the representation of solutions using chromosome with N digits is equal to decomposing the solution into N aspects, each of which can be compared among different solutions.

The similarities of chromosomes mentioned above can be expressed using the notion of schema (plural: schemata) according to Holland [53]. Schema is a template for a specific pattern matching in the binary string of genotype, which has the following form:

$$h = (h_1, h_2, \dots, h_l), h_i \in \{0, 1, *\} \quad (2.7)$$

where  $h_i$  is the  $i$ -th digit of a schema  $h$ ,  $l$  is the length of the genotype string,  $*$  denotes the unfixed digits. For example the schema  $*1*00*1$  can have the following instances: 1110011, 0110001, and 0100011. The order of a schema  $h$ ,  $o(h)$ , and its defining length,  $\delta(h)$ , are two important attributes, which can influence its propagation among generations.  $o(h)$  is defined as the number of fixed digits and  $\delta(h)$  refers to the distance between the two outermost fixed bits. It can be seen that during reproduction the schemata with large defining lengths are more likely to be disrupted by the crossover operation and those with high orders are prone to be disrupted by the mutation operation. This point will be discussed later.

During the optimization process, the different schemata can either propagate or decay in subsequent generations of populations depending on their nominal fitness, that is, the average fitness of all its instances:

$$f(h) = \frac{1}{||h||} \sum_{x \in h} f(x) \quad (2.8)$$

with respect to the average fitness of the population. Here,  $f$  is the genotype-/schema  $\rightarrow$  fitness mapping function,  $x$  is the genotype of one candidate solution in the search space,  $||h||$  is the number of individuals in the search space that are instances of schema  $h$ . Holland [53] and De Jong [54] formulated the variation of the number of instances of a schema in two adjacent generations  $t$  and  $t+1$ , when using a standard GA with proportionate selection, one-point crossover and bit-flip mutation:

$$m(h, t+1) \geq m(h, t) \frac{f(h, t)}{\bar{f}(t)} \left(1 - p_c \frac{\delta(h)}{l-1} - p_m o(h)\right) \quad (2.9)$$

where  $m(h, t)$  is the number of instances in the population that belong to schema  $h$  at generation  $t$ ,  $f(h, t)$  is the nominal fitness of the schema  $h$  (defined in equation 2.8) at generation  $t$ ,  $\bar{f}(t)$  is the averaged fitness of the whole population at generation  $t$ ,  $\delta(h)$  is the defining length of schema  $h$ ,  $p_c$  is the crossover rate,  $p_m$  is the mutation rate,  $l$  is the string length of the genotype,  $o(h)$  is the order of schema  $h$ .

The terms  $p_c \frac{\delta(h)}{l-1}$  and  $p_m o(h)$  in equation 2.9 are the possibility of disrupting a schema by crossover and mutation operation respectively. The equation above implies that the short, low order schemata with their fitness  $f(h, t)$  far above the average fitness of the population  $\bar{f}(t)$  will have a quasi-exponentially increasing occurrence in subsequent generations.

Such highly fit schemata are considered as containing parts of the optimum solutions. This can be visually illustrated by a simple case of a two-variable fitness function  $f(X, Y)$  (Figure 2.18). Here we use direct representation, that

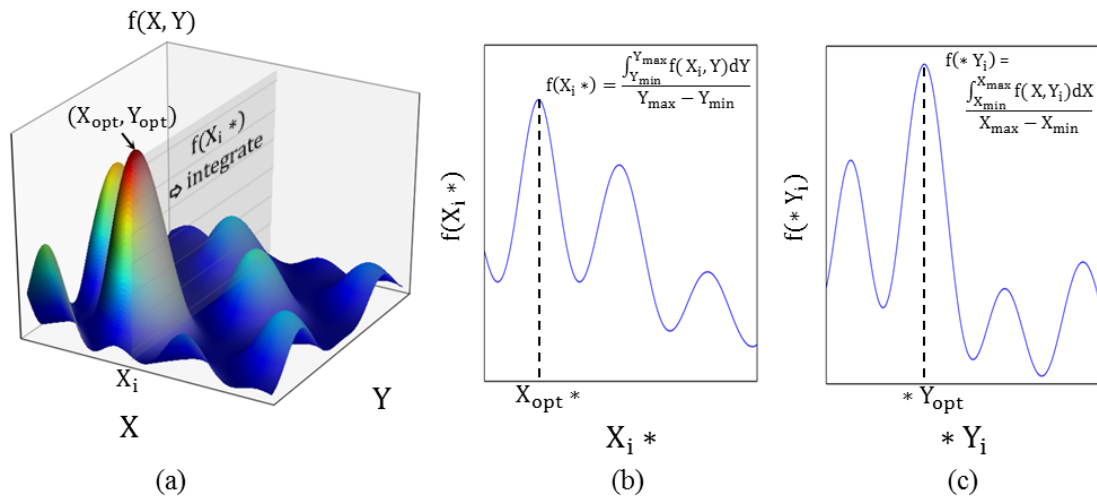


Figure 2.18. (a) The fitness landscape of a two-variable fitness function. (b) The fitness of schemata in the form of  $X_i *$ . (c) The fitness of schemata in the form of  $* Y_i$ .

is, the genotype is exactly the solution itself  $XY$ . So totally there are two forms of schemata  $X*$  and  $*Y$ . The fitness of a specific schema, let's say  $X_i *$  ( $X_i \in (X_{min}, X_{max})$ ), is actually proportional to the integration of the fitness function across the search space along the line  $X = X_i$  as shown in Figure 2.18. As we can see, the schemata  $X_{opt} *$ , which contain the part of the optimum solutions ( $X_{opt}, Y_{opt}$ ), will have the highest fitness values among all the competing schemata and thus the fastest propagation in subsequent generations. The same is true for the form of schemata  $*Y$ .

This simple example also implies the relative growth and decay among a set of competing schemata of the same form over generations actually reflects the "projected" fitness landscape along a certain direction through the search space (as the integration shown in Figure 2.18). The population of GA even with a medium size ( $N$  individuals) actually processes a large amount of schemata, which is in the order of  $N^3$  according to Holland [53]. As a result, the numerous schemata with different forms provides GA a multiple perspective through the search space by projecting the fitness landscape along different directions. It is this global view that enables GA to reliably determine the region of the global optimum inside the search space. Since the processing of a huge amount of schemata occurs simultaneously in the population, the convergence towards the global optimum is highly efficient. This property of GA is also referred as the implicit parallelism of GA [55] in comparison with the its explicit parallelism, that is, simultaneous exploring  $N$  points of search space in each generation.

Besides propagation of specific schemata by the selection process, the process of crossover plays a key role in the convergence of GA towards the global optimum. As mentioned above, the short and highly fit schemata can probably contain fragments of the optimum solution, which are thus also referred to as "building blocks" in the building block hypothesis [55]. According to this hypothesis, with their multiplication in succeeding populations due to repeated selections, these initially

well-distributed fragments of the optimum solution are meanwhile recombined and assembled by the crossover operator to form potentially highly-fit chromosomes, which become more and more similar to that of the global optimum.

In this process the random aspect of GA plays a rather positive role in the fast convergence towards the global optimum. As shown in Figure 2.19 since the first population is randomly generated, the enrichment of building blocks usually occurs at different locations of the chromosomes. The recombination of such two chromosomes by crossover operator can thus lead to a leap in terms of the fraction of the "correct genetic information" with respect to the optimum solution (in the most ideal case, it can double in the offspring generation). This is especially true in the first few generations where the genetic diversity among individuals is rather high. If the fitness of an individual is assumed to generally scale with the enrichment of building blocks in its chromosome, a leap of fitness value of the best solution would be expected in the first few generations.

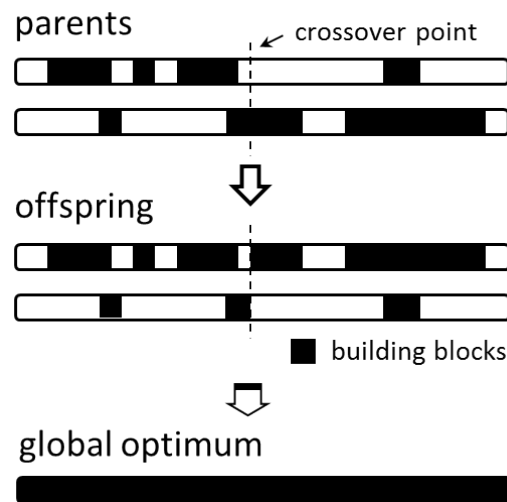


Figure 2.19. The enrichment and depletion of building blocks in offspring chromosomes after crossover.

It should be noted that crossover not only leads to the enrichment of building blocks in one of the two offspring chromosomes but also leads to a depletion of building blocks in the other (Figure 2.19). Thus, during each crossover two trial solutions with different searching direction will be generated: one towards the potential optimum and one towards the opposite direction. This property is very important for the robustness of the GA in solving the so called deceptive problem, which is considered to be the most difficult category of problems for GA. In such a problem, the optimum solution is usually surrounded by the worst solutions in the space of genotype<sup>2</sup>. The schemata that are associated with high fitness in the beginning actually have very little similarity with the true optimum. Thus it is assumed that the processing of schemata will mislead GA towards a point that is far away from the true optimum. However, it was found by different researchers

<sup>2</sup>In fact, deceptive problems are also considered to be more difficult than other problems for most of optimization methods except random search.

that those deceptive problems are usually not GA-hard [55, 56]. It is very likely that each trial solution after crossover, in which the fake building blocks are largely depleted, can help discover the possible global optimum hidden in the cluster of worst solutions.

Although repeated selection and crossover gives GA the bulk of processing power in the efficient exploration and exploitation of the search space, mutation is also a necessary auxiliary operator for the high performance of GA. The need of mutation operator is mainly due to fact that the populations of GA in many real applications are limited. As mentioned above the propagation of a schema requires an above-average fitness value, which is approximated by the average fitness of all its instances in the current population. However, when the population size is small, such an approximation can significantly fluctuate around the true fitness depending on the fitness distribution of its limited instances in the population. There can be a large chance that the real fitness of an advantageous schema is considerably underestimated and it becomes actually disadvantaged in the evolution. Even if it is indispensable for evolving the global optimum, it can probably die out in the first few generations before the selection pressure can act on it correctly. Such a loss of genetic diversity due to this stochastic nature of the evolution process is called genetic drift [56]. In some worst cases, the loss of important genetic information can lead to premature convergence to a local optimum. Mutation can be considered as an insurance policy against this premature loss of genetic information in population, since any lost schema can in principle be brought back to the population by this random modification of alleles of different chromosomes in the population.

In addition, mutation also plays an important role in the stage of local search. According to Deb [58], the process of GA search can be divided into a global search stage and a local search stage. In the global search stage, where the diversity of the population remains high, GA depends on the repeated selection and crossover to locate the region of interests. After this stage, the genotypes of the whole population are brought together in the search space and the stage of local search starts. In the local search, the genetic difference among the population is rather small, selection and crossover can hardly provide sufficient gradient to drive the GA towards the global optimum. Further improvement of fitness mainly depends on mutation, which provides a random work in the vicinity of the already obtained high quality solutions. However, this process can take rather long time before the optimum point is found. This is known as the problem of slow finishing of GA [59]. As a result, GA is usually coupled with a local search (LS) technique to form a memetic algorithm [60–62], which combines the robustness and high efficiency of GA in the global search and the effectiveness of LS in fast locating the optimum point in the region of convergence.

### 2.2.3 Choose suitable representation for GA

The understanding about the functioning mechanism of GA can help us apply GA in the most effective way. The key aspect for the implementation of GA is choosing a suitable representation scheme to encode candidate solutions into genotypes, which can fully lever the processing power of GA. Previous researchers

have made different suggestions for GA users. Some of the first recommendations come from Goldenberg [55], which contains two parts:

1. Principle of meaningful building blocks: "The user should select a coding so that short, low-order schemata are relevant to the underlying problem and relatively unrelated to schemata over other fixed positions"
2. Principle of minimal alphabet: "The user should select the smallest alphabet that permits a natural expression of the problem."

The first principle is directly motivated by the theorem of schemata, since the short, low-order schemata, which are less likely to be disrupted by crossover and mutation, form the foundation of the processing power of GA as mentioned in section 2.2.2. Those highly fit and short schema known as building blocks are interpreted by Rothlauf [56] as partial solutions to the small subproblems that can be decomposed from the original problem. As a result, this principle implies that, in order to make the applied GA most efficient, the user should try to decompose the solution into small and relatively independent sections or aspects, each of which can be represented with less number of alleles.

The second principle actually favors the use of bit string representation, which has the minimum members of the alphabet (i.e. 0 and 1). According to Goldenberg, the smallest alphabet maximizes the number of schemata per bit of information. As a result, the bit string representation is supposed to be most effective in correlating the high fitness with the similarities among genotypes. Another advantage of using bit string representation is that the user can easily apply the canonical genetic operators (i.e. one/two-point crossover and bit-flipping mutation) with well-understood and reliable performance.

In addition to the recommendations from Goldenberg, Palmer et al. [63] suggested that the encoding should possess locality, which means small changes in the genotype should result in small changes in the phenotype. Rothlauf also made a quite similar suggestion regarding the allocation of redundant representations [56] when more genotypes needed to be mapped into fewer phenotypes. Although the redundancy of representation can potentially decrease the performance of GA, they can hardly be avoided when encoding discrete-valued variables using the binary representation scheme, since the binary alleles provide much more restricted number of variations (that is  $2^m$  variations for a  $m$ -bits binary encoding) compared to the possible number of candidate values to be encoded, which can be of any amount. To handle this redundancy, Rothlauf suggested that the genotypes that represent the same phenotype should also possess good neighbourhood in the space of genotype. Both the two suggestions above are based on the fact that GA works by exploiting the similarities of solutions via their genotypes (section 2.2.2). As a result, the neighbourhood between different solutions should be well preserved in their genotypical expressions.

## 2.2.4 Extension of GA to solve multiple objective optimizations

For many complex engineering optimization problems, the quality of a solution is not evaluated with a single criterion but with a series of different design objectives (i.e. maximize the performance, minimize the cost and structural weight, maximize the reliability, and etc.). For such multi-objective optimization problems, the different design objectives usually contradict with each other, which means the optimizing with respect to one objective can unavoidably lead to the degradation of performance in some other objectives. Thus, in such a situation decision makers often need a set of good solutions instead of a single optimum, which can tell the best trade-off between those conflicting design objectives. Such solutions are also called Pareto optimum solutions, which are not be dominated by any other feasible solutions [64,65].

The relation of domination between two feasible solutions can be mathematically formulated as follows. A solution  $x$  is said to be dominated by another solution  $y$  for the case of minimization, if and only if, the following two requirements hold simultaneously [64]:

1.  $z_i(x) \geq z_i(y)$  for  $i = 1, 2, \dots, K$
2.  $z_j(x) > z_j(y)$  for at least one objective function  $j$

where  $z_i(x^*)$  ( $i = 1, 2, \dots, K$ ) are the set of objective functions to be minimized. Such domination relation between two solutions can be clearly illustrated in the objective space of a simple optimization problem with two objectives (Figure 2.20). Both the objectives  $z_1$  and  $z_2$  are to be minimized. As shown in Figure 2.20, solution  $b$  is said to be dominated by solution  $a$  since solution  $a$  is located in the lower left quadrant of  $b$  in the objective space, which is bounded with the black dash lines. For  $a$ , there is no other feasible solution in its lower left quadrant in the objective space. As a result,  $a$  is said to be a Pareto optimum solution or a non-dominated solution. All the feasible non-dominated solutions form the so-called Pareto front in the objective space. The solutions behind the Pareto front are all dominated solutions as shown by the red dots in Figure 2.20.

The aim of multi-objective optimizations is to identify a set of diverse solutions on the Pareto front, which should be uniformly distributed and should cover the whole spectrum of the Pareto front. As a population-based approach, GA is considered as an ideal tool to achieve this aim. The characteristic of GA in exploring different regions of search space simultaneously make it capable of finding a diverse set of non-dominated solutions in a single run. The crossover operator also facilitates GA to exploit the structure of good solutions with respect to different objectives and to find non-dominated solutions in the unexplored regions of the Pareto front. Various approaches have been proposed to further extend GA to solve the multi-objective optimization problems [66–70].

The non-dominated sorting genetic algorithm II (NSGA-II) is one of the most well tested and widely used procedure. In this method GA is modified in terms of fitness assignment scheme and elitist strategy for the task of multi-objective optimization.

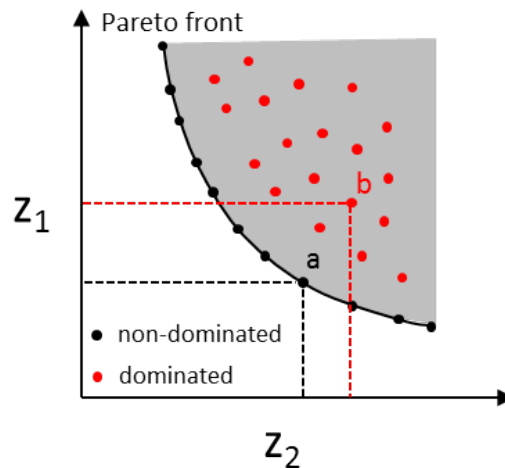


Figure 2.20. Schematic sketch of the positions of non-dominated solutions (black dots) and dominated solutions (red dots) in a two-dimensional objective space. The shaded area indicates the feasible region in the objective space.  $z_1$  and  $z_2$  are the objectives to be minimized.

### Fitness assignment scheme of NSGA-II

Since in multi-objective optimization each candidate solution is evaluated against a series of criteria, the original strategy of GA to differentiate solutions using a single scalar fitness will not work. In NSGA-II, the solutions are compared at two different levels. The first level is based on non-dominated ranking of the population. In a first step, all the non-dominated solutions are identified. Then those non-dominated solutions are copied to the set  $F_1$  (the first non-dominated front) and are meanwhile removed from the population (Figure 2.21). In the next step, all non-dominated solutions in the rest of the population are identified and moved to the set  $F_2$  (second non-dominated front). This procedure continues until all the member of the population are subsumed under their corresponding non-domination rank. When comparing two solution e.g. in the binary tournament selection, the solution with the lower non-domination rank will win.

However, if both solutions come from the same rank of non-dominated front, then they will be compared at the second level based on the crowding distance. The crowding distance of a solution is defined as the sum of the normalized distances between its two neighbouring solutions in the objective space with respect to different objectives (Figure 2.21 b). It is a measure of the objective space around a solution, which is not occupied by any other solution from the same non-dominated rank. Thus the comparison based on crowding distance will favor the solutions located on the relatively loose sections of the non-dominated front. This strategy helps to preserve the diversity of solutions during the course of the evolution and also can achieve an uniformly distributed non-dominated solutions along the best-known Pareto front.

In summary, after evaluating the whole population with respect to the multiple objectives each candidate solution  $i$  is assigned with two attributes of fitness

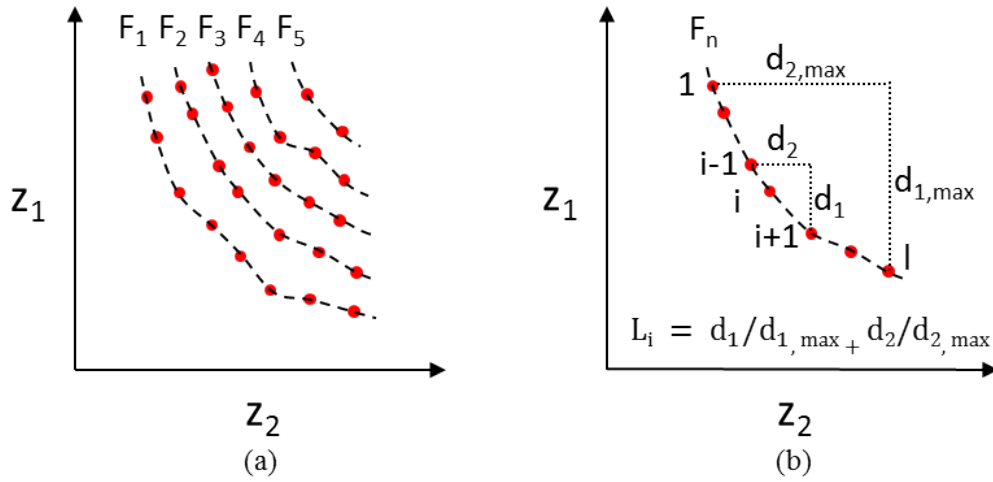


Figure 2.21. (a) Non-dominated ranking of the population into different sets non-dominated fronts  $F_1 - F_5$ . (b) Definition of crowding distance  $L_i$  at a solution  $i$  in non-dominated rank  $F_n$  in a two-dimensional objective space. Solutions  $1$  and  $l$  are the two outermost solutions of  $F_n$ , which have infinite crowding distance.  $z_1$  and  $z_2$  are the objectives to be minimized.

based on its relative location in the objective space: the non-dominated rank  $i_{rank}$  and the crowding distance  $i_{distance}$  as described above. When comparing two solutions  $a$  and  $b$ ,  $a$  is considered to be fitter than  $b$  only if either of the two following conditions is met:

1.  $a_{rank} < b_{rank}$ .
2.  $a_{rank} = b_{rank}$  and  $a_{distance} > b_{distance}$ .

### Elitist strategy of NSGA-II

The elitist strategy in GA means the best solutions of the present generation will be preserved in the next generation. Numerous researchers reported that the application of elitism in multi-objective GA can achieve better convergence and higher overall performance. [65, 71–74]. However, the implementation of elitism in multi-objective optimizations is not as straightforward as single objective optimizations, in which the best solution is simply copied to the new generation. This is mainly due to the large size of non-dominated solutions evolved in the population. If they are directly copied to the next generation as elite solutions, there can be little room for the newly evolved solutions in the next generation.

In order to conquer this problem, NSGA-II uses a combined population of both parent and offspring generations to maintain a group of the non-dominated solutions as large as the original population without the need of reducing the number of newly evolved solutions at each generation. This strategy is schematically shown in Figure 2.22. At a time point  $t$ , after the reproduction of offspring generation  $O_t$  from a parent generation  $P_t$ , both generations are combined to form a population with a double size. Then this combined population is sorted into different ranks of non-dominated fronts ( $F_1 - F_6$  in Figure 2.22) using the method specified in

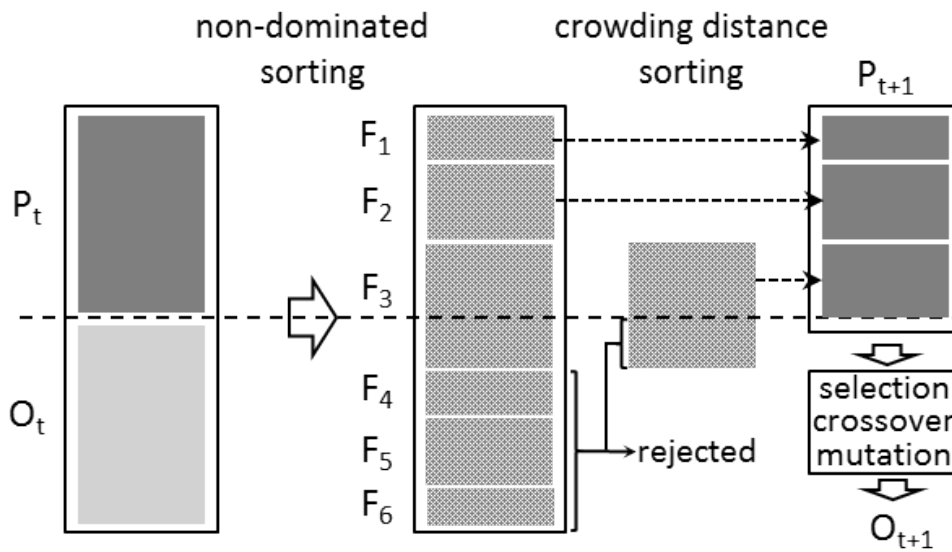


Figure 2.22. The elitist strategy used in NSGA-II (after [70]).

the previous section. A new generation of parent  $P_{t+1}$  is created by filling the population with the sorted non-dominated fronts starting with the lowest ranks. However, if the free space of the population is not enough to accommodate the whole non-dominated front of a specific rank (e.g.  $F_3$  in Figure 2.22), this non-dominated front will be sorted in descending order with respect to the crowding distances of its members. Then the solutions with the largest crowding distances will be included in the rest of the population  $P_{t+1}$ . After that, a new generation of offspring  $O_{t+1}$  can again be generated through the selection, crossover and mutation process. In this way, the solutions with highest qualities are always preserved in the parent population and meanwhile the newly evolved solutions in the offspring population can ensure a significant exploration of the search space at each generation.

With the two aforementioned modifications of GA, NSGA-II can reliably solve a wide spectrum of multi-objective optimization problems showing outstanding performance in terms of the convergence, uniformity and span of solutions as well as the time efficiency [70].



## 3. Experimental

### 3.1 Materials

Metal sheets of the materials AA2139 (4.5 mm thick, T351 heat treatment condition) and AA2198 (5 mm thick, T3 heat treatment condition) were investigated in this study. The nominal compositions of both materials are given in Table 3.1:

Table 3.1. Chemical composition of AA2139 and AA2198 (wt%) [13, 75].

AA2139							
Cu	Mg	Ag	Mn	Zn	Fe	Ti	Si
4.5-5.5	0.2-0.8	0.15-0.6	0.2-0.6	≤0.25	≤0.15	≤0.15	≤0.1

AA2198								
Cu	Li	Mg	Ag	Mn	Zn	Zr	Si	Fe
2.9-3.5	0.8-1.1	0.25-0.8	0.1-0.5	≤0.5	≤0.35	0.04-0.18	≤0.08	≤0.01

### 3.2 Microstructure and texture characterization

The grain structure and texture of both materials were investigated using optical microscopy and EBSD analysis. Samples for metallographic observation were sectioned parallel to the longitudinal/transverse (L-T) plane, the normal/longitudinal (N-L) plane and the normal/transverse (N-T) plane respectively. The EBSD analysis was performed on N-L sectioned specimens so that the possible variation of texture in the through-thickness direction resulting from the rolling process can be examined. The Kikuchi patterns were measured using an EDAX Pegasus XM4 system incorporated in a JEOL JSM-6490LV SEM. The magnification at SEM during the EBSD analysis was 500x for AA2198 and 100x for AA2139. The collected data was processed using the software package TSL OIM Data Collection 5.31 and OIM Analysis 5.31.

### 3.3 Biaxial fatigue tests and FEM modeling of the experimental setup

To investigate the variation of the effectiveness of crenellations with different materials, fatigue tests were carried out on flat and crenellated panels made of the two materials respectively. Square-shaped specimens (560 mm x 560 mm, as shown in Figure 3.3) representing parts of fuselage panels were cyclically loaded

in two perpendicular directions, which is aimed at imitating the periodic fuselage load due to the repeated cabin pressurization and depressurization among flights (Figure 3.1). The specimens were cut from the metal sheets of both materials. The outer part of the specimens has the original thickness of the sheet, while the inner region (400 mm x 400 mm) was machined to be either flat (thickness: 2.9 mm, machined symmetrically from both surfaces) or crenellated (machined only on one side of surface).

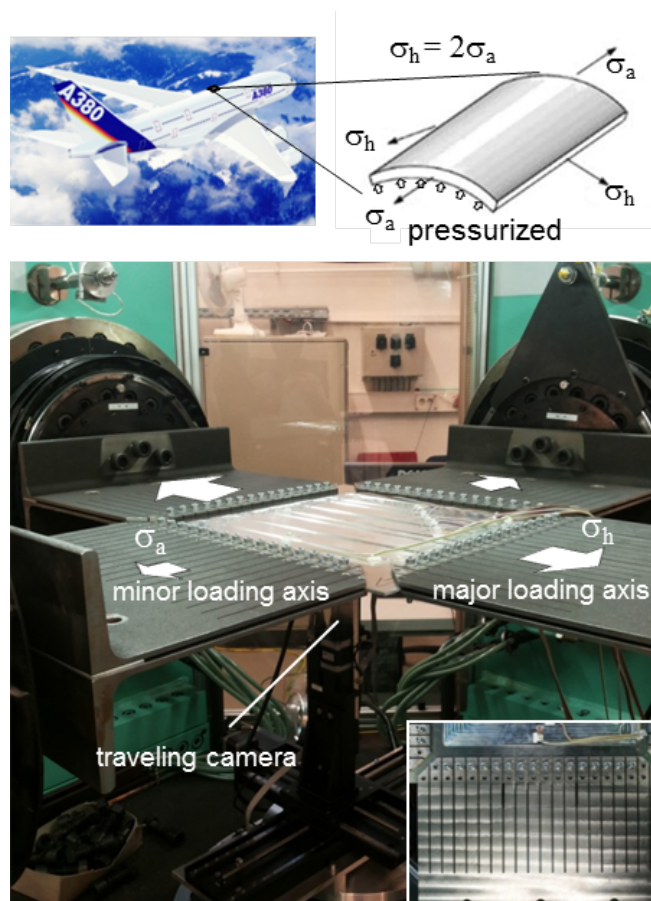


Figure 3.1. Experimental setup of biaxial fatigue testing.

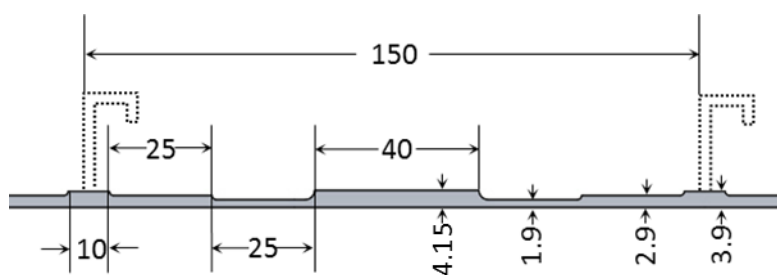


Figure 3.2. Geometries of crenellation pattern investigated in this study. Unit: millimeter.

The crenellation pattern investigated in this study is equivalent in weight to

a reference sheet with a thickness of 2.9 mm, the detailed geometry of which is shown in Figure 3.2. This crenellation pattern is exactly the same as the one examined by Uz [7] under uniaxial loading conditions. In the bay between every two adjacent stringers, a centered thickened region with a thickness of 4.15 mm is designed for crack retardation. The extra weight of this pad-up is compensated by two thickness reduction regions (1.9 mm) located on both sides. Each crenellated specimen contains two such bays of crenellations. The positions of the three stringers are marked by red lines in Figure 3.3. The fatigue crack is assumed to initiate at the root of the middle stringer. In order to focus on the sole effect of the crenellation itself, the stringers were not welded.

The specimens were horizontally fixed in a biaxial servo-hydraulic testing machine with specially designed clamping device. The finger-like parts of clamping devices are aimed at distributing the exerted load evenly through the specimens (Figure 3.1). The ends of those "fingers" of each clamping device were connected to a row of 16 rivet holes along one side of specimen. Constant amplitude cyclic loading was applied in both axes of the machine in phase ( $F_{\text{major,max}} = 112.4$  kN,  $F_{\text{minor,max}} = 56.2$  kN) with a R-ratio of 0.1 and a frequency of 3 Hz. The fatigue cracks were initiated at both tips of a 12 mm center notch (tip radius: 0.15 mm), which align perpendicular to the major loading direction and parallel to the rolling direction of the sheet materials. Every time the crack had an approximately 1.5 mm extension at both crack tips, the cyclic loading was halted and the positions of crack tips were recorded using a traveling camera under the specimen.

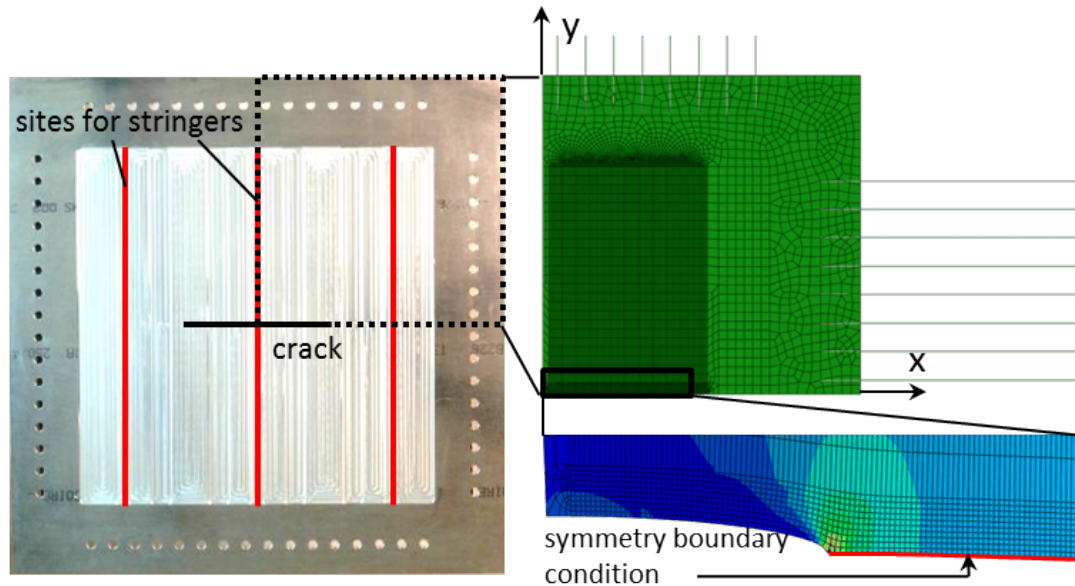


Figure 3.3. Specimen and FEM modeling of the experimental setup.

A quarter FEM model for this experimental setup was established using the commercial code ABAQUS (version 6.14) (Figure 3.3). Quadrilateral 4-node shell elements with reduced integration were applied to model the panel. The clamping device with finger-like features was modeled as a series of beams using quadratic 3-node beam elements. The beam ends on one side were tied to the respective

positions of rivet holes with untied degree of rotations. On the other side, they are kinematically coupled to a reference point, on which the load of the clamping device was applied. The global mesh size of the panel was 8 mm. Along the crack path, which was situated at the lower edge of the quarter model, the mesh was refined to 1 mm. The growth of the crack was realized by sequentially releasing the symmetrical boundary condition applied at the old crack tip node by node. The stress intensity factor at the maximum load of cyclic loading for a given crack length was obtained through the calculation of the energy release rate  $G$  using the virtual crack closure technique (VCCT) [76]. As shown in Figure 3.4, when the maximum load was applied in the FEM model, the reaction force ( $P_y$ ) at the crack tip node and the displacement ( $u_y$ ) of the node directly after the crack tip were extracted respectively from the ODB file of the simulation. According to the virtual crack closure technique (VCCT), the mode I energy release rate  $G_I$  is calculated by the following equation [76]:

$$G_{I,\max} = \frac{P_y u_y}{\Delta a t} \quad (3.1)$$

where  $\Delta a$  is equal to the element size along crack path (1 mm) and  $t$  is the local thickness of the panel. If the plane stress condition is assumed  $G_{I,\max}$  can be converted into the mode I stress intensity factor  $K_{I,\max}$  by the following equation [24]:

$$K_{I,\max} = \sqrt{G_{I,\max} \cdot E} \quad (3.2)$$

Then, the driving force for fatigue crack growth, namely the stress intensity factor range  $\Delta K$ , is calculated by:

$$\Delta K_I = K_{I,\max} - K_{I,\min} = (1 - R)K_{I,\max} = 0.9K_{I,\max} \quad (3.3)$$

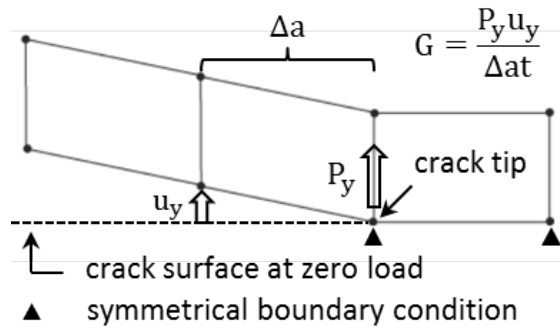


Figure 3.4. Calculate the energy release rate using the virtual crack closure technique. (based on the description in [76])

### 3.4 Measurements of crack closure level

The crack opening load was measured by a  $\delta_5$  clip gauge mounted at one crack tip (Figure 3.5 a), which is the same as used by Heerens et al. [77]. However, in

contrast with the stationary clip gauge in their work, the clip gauge in this study was remounted to the new crack tip every time when the crack extended 10 mm further. To facilitate the remounting of clip gauge magnetic supports were used, which can be conveniently fixed at proper positions either on the ferrous clamping device or on the specimen surface with the help of bottom magnets placed on the other side of the panel. During the remounting of clip gauge, two indents with 5 mm distance were firstly made above and below the crack tip respectively by using the tool shown in Figure 3.5 b. After fitting the two tips of the clip gauge into the indents, fast glue Z70 from the HBM Company was applied to both tips to ensure a good attachment to the specimen surface. The glue was afterwards dissolved using a commercial acetone EMSURE<sup>®</sup> before the next remounting. During the fatigue test, the measurement of the crack closure level took place at every 2-3 mm of crack extension. In each measurement 200  $\delta_5$  values and the corresponding instantaneous loads in a complete load cycle were recorded with equal time intervals. The data in the uploading phases were used to extract the crack opening load using the compliance method [78]. As shown in Figure 3.6 a, the load- $\delta_5$  curve in the uploading phase was divided into many partially overlapping sections. Each section had a span covering about 10% of the total load range and the adjacent sections had an overlap about 50% with respect to each other. Then, the local compliances of each small section were fitted, which were compared with the overall compliance in the upper quarter of the curve with linear response. Their offsets relative to the overall compliance were plotted in Figure 3.6 b. A B-spline curve was fitted through those points, which had a continuous increasing trend of offset values with decreasing load. Then, the crack opening load was determined from the fitted curve, where the offset value was equal to 5%.

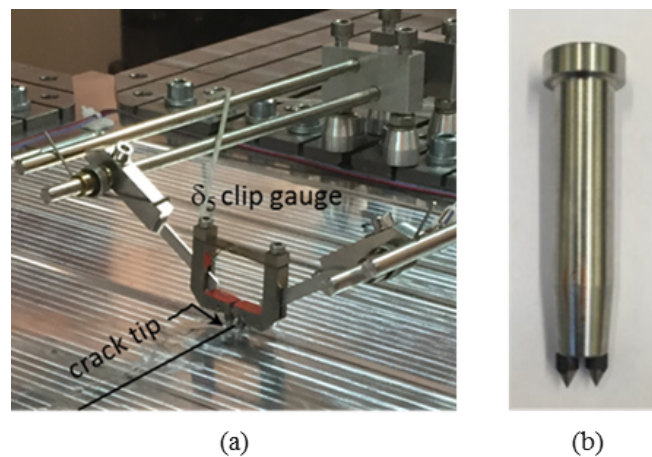


Figure 3.5. (a) Mounting of  $\delta_5$  clip gauge at the crack tip. (b) Tool for making 2 indents at crack tip with a spacing of 5 mm.

### 3.5 Fracture surface observation

After the fatigue tests, an investigation on fracture surface was performed to better understand the observed fatigue crack growth behavior. Firstly, a stripe

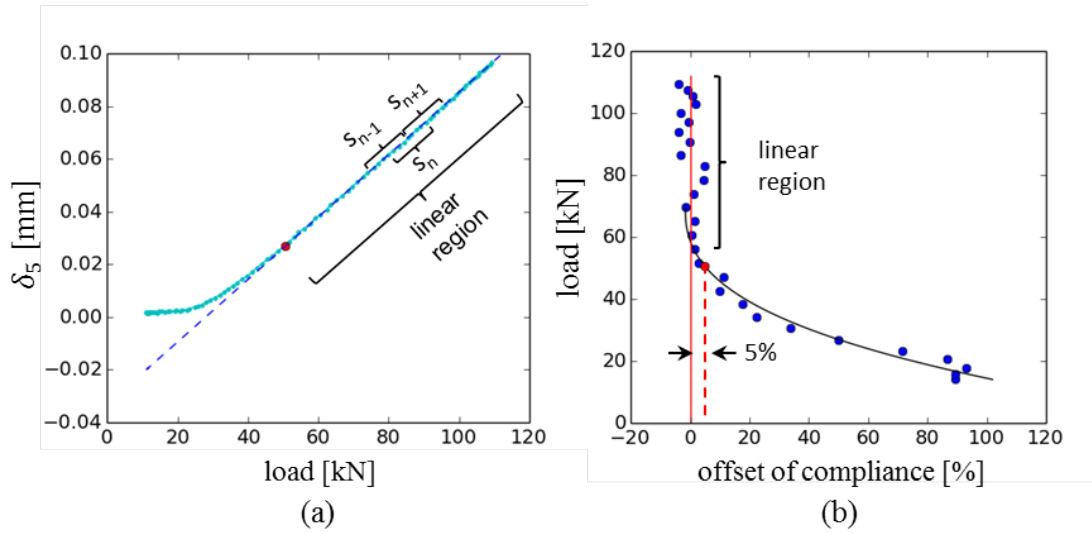


Figure 3.6. Determination of crack opening load by the compliance method. (a)  $\delta_5$  vs. load curve recorded instantaneously during cyclic loading. (b) The offsets of local compliance fitted at different small sections ( $s_1, s_2, \dots, s_n, \dots$ ) compared with the overall compliance in the linear region.

of material (about 300 mm x 40 mm) that contains the crack was cut out from each specimen, which was subsequently sawed into several small parts for the convenience of handling. The revealed fracture surface was then examined under a magnifier lens. The 3D morphology of the fracture surface was also measured using a VK-9700 Keyence color 3D laser microscope. The angle between the shear lip plane and the fracture plane was measured on the reconstructed 3D morphology model using the software VK Analyzer 2.5.0.1. A close examination on the fracture surface was carried out using a JEOL JSM-6490LV SEM.

## 4. Influence of materials on the crenellation efficiency

In this chapter the possible influence of materials on the effectiveness of crenellations is investigated. Two candidate alloys for future airframe structures: AA2139 and AA2198 are used in this study for their significant inherent difference. Firstly the grain structure and texture of the two materials were characterized. Then, the fatigue behaviors of flat and crenellated panels made of each material were examined. Possible clues to understand the observed fatigue behavior were obtained through the crack closure measurement during the tests as well as the subsequent fracture surface examination.

### 4.1 Results

#### 4.1.1 Microstructure and Texture

The grain structures of the two materials are compared in Figure 4.1. The material AA2139 has slightly elongated grains in the rolling direction. The averaged grain sizes in the rolling direction and in the normal direction are  $45.5\ \mu\text{m}$  and  $24.3\ \mu\text{m}$  respectively. In contrast, AA2198 has highly elongated grains, which form a pancake-like structure. The averaged grain size in the normal direction is  $3.7\ \mu\text{m}$  whereas in the rolling direction the grain size can exceed 1 mm. The aspect ratio is more than 400:1. The two materials also show distinct textures as shown in Figure 4.2. AA2139 has nearly random orientation of grains with very weak cubic texture component. No variation in terms of texture in the thickness direction is found. AA2198 shows very sharp Brass texture in the center of the panel, whereas near the sheet surface strong S texture components appear. The nature of the random or sharp texture in the two materials is well reflected by the respective colour coded mapping of [100] inverse pole figures (Figure 4.3). As it can be seen the adjacent grains in AA2139 have distinct orientations whereas in AA2198 the misorientation between neighboring grains is rather small.

#### 4.1.2 Fatigue crack growth tests

The results of the fatigue tests (Figure 4.4 a) show that, under the same loading condition, panels made of AA2198 generally have higher fatigue resistance than the panels of the material AA2139. The fatigue life improvement by crenellations in the material AA2198 is two times of that in the material AA2139. The crack propagation rates calculated using a 5-points-polynomial fitting method [78] were plotted against the corresponding stress intensity factor ranges from the FEM

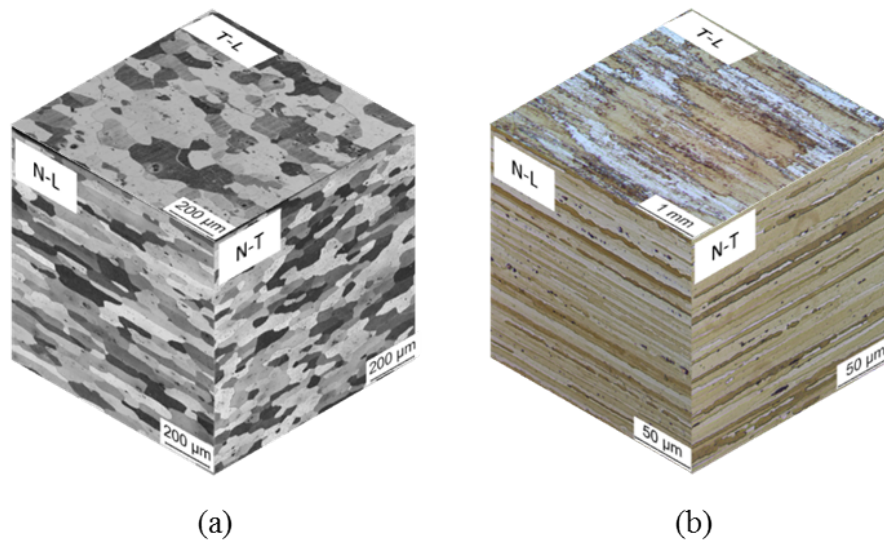


Figure 4.1. Microstructures of (a) AA2139 and (b) AA2198.

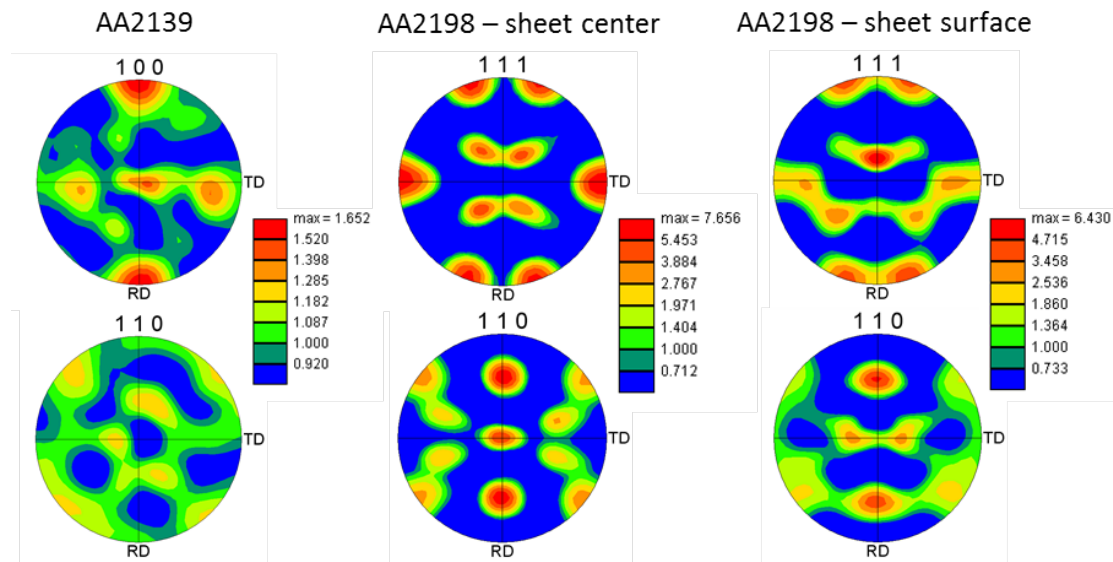


Figure 4.2. Variation of texture in different materials and at different positions of the panel.

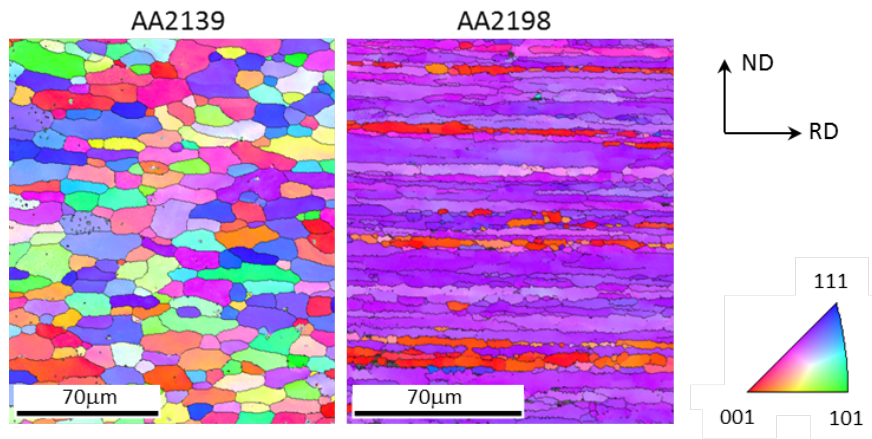
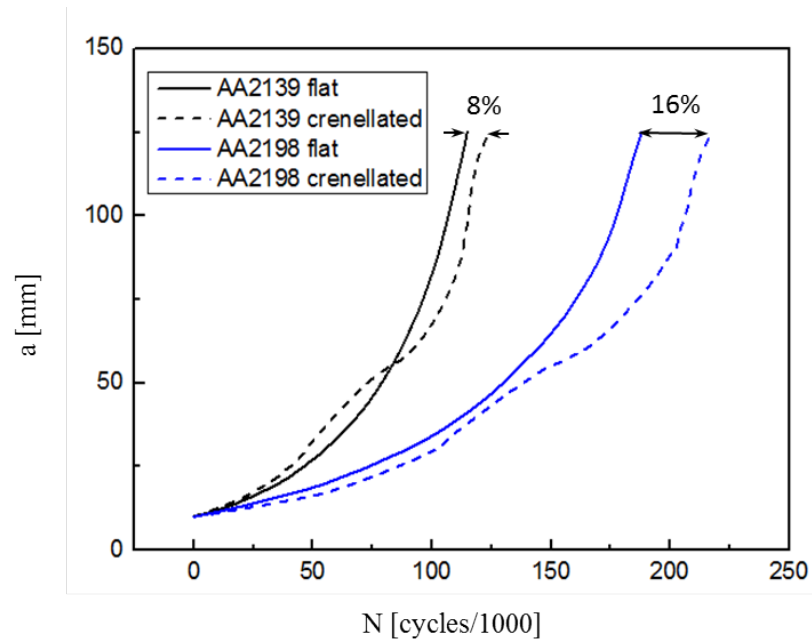


Figure 4.3. Color coded mapping of [100] inverse pole figures in both materials.

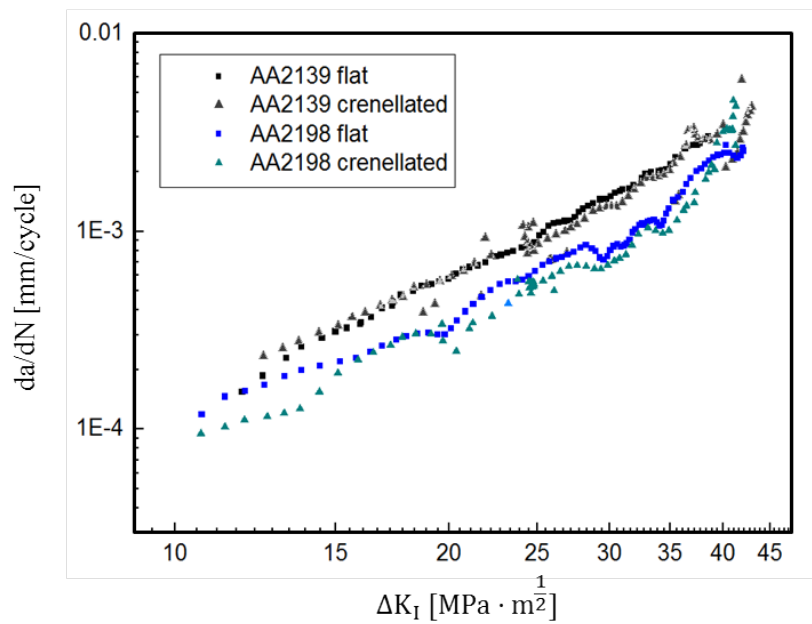
simulations in double logarithm form (Figure 4.4 b). The data points of both flat and crenellated panels of AA2139 fall into the same linear band as characterized by Paris Law whereas the data points for panels of AA2198 deviate significantly from this linear relation. In addition, there is a gap between the data points of flat and crenellated specimens, which is more pronounced at smaller values of  $\Delta K$ . The crenellated panel of AA2198 generally has lower crack propagation rates (the  $da/dN$  values) at the same  $\Delta K$  compared to the flat panel. In the low  $\Delta K$  range ( $< 15 \text{ MPa} \cdot \text{m}^{1/2}$ ), the  $da/dN$  values of AA2198 flat panel tend to be the same as those of the panels of AA2139. The same trend is also found in the high  $\Delta K$  range ( $> 35 \text{ MPa} \cdot \text{m}^{1/2}$ ) where the  $da/dN$  values of all the panels tend to be the same.

During the fatigue tests, the crack opening load was measured along the crack path with a spacing of about 2 mm. Figure 4.5 a summarizes the averaged crack opening load measured in the flat and crenellated specimens of both materials, and the standard deviations of the data are shown in error bars. As it can be seen, both the flat and crenellated panels of AA2139 have the same averaged crack opening load of 46 kN. In comparison the flat specimen of AA2198 has a slightly increased crack opening load, whereas that of the AA2198 crenellated specimen is significantly higher. The scattering of the data is much larger in the AA2198 specimens compared to the AA2139 specimens.

The detailed variations of crack opening loads with half crack lengths of tested specimens are shown in Figure 4.5 b. Since the AA2139 flat and crenellated specimens have nearly the same trend of variation, only the data of the flat specimen is presented as reference for the clarity of the figure. As it can be seen, in the beginning ( $a < 30 \text{ mm}$ ) the crack opening loads of both flat specimens of AA2139 and AA2198 were at the same level, whereas in the same range that of the AA2198 crenellated specimen is significantly higher. When the half crack length exceeds 30 mm, the crack opening load of the AA2198 flat specimen increases dramatically up to the level of the AA2198 crenellated specimen. In the AA2198 crenellated specimen, there is a periodic variation of measured crack opening loads with the repeated repositioning of  $\delta_5$  clip gauge at the newest crack tips (P.1, P.2, P.3 . . . in



(a)



(b)

Figure 4.4. (a) The fatigue performance of flat and crenellated panels with different materials. (b)  $da/dN - \Delta K$  plot of the four tested specimens.

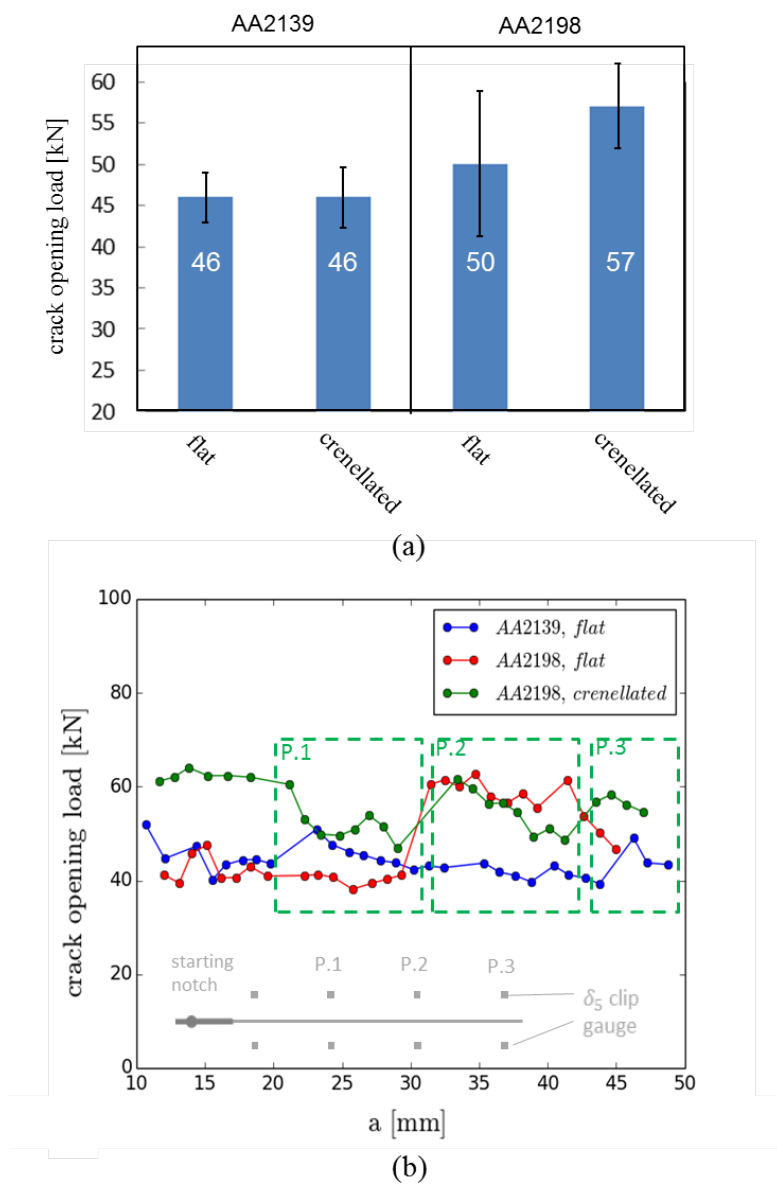


Figure 4.5. (a) Comparison of average crack opening load in the flat and crenellated specimens with AA2139 and AA2198 respectively. (b) The profiles of crack opening load measured along the crack path.

Figure 4.5 b), which is schematically sketched in the lower part of the figure. When the clip gauge is just repositioned, the measured crack opening loads are among the highest values. Then with further extension of crack, the crack opening loads are observed to decrease significantly. Such a decrease of measured crack opening loads with increasing distance from the crack tip is also observed in the AA2198 flat specimen when the half crack length exceeds 40 mm. In the AA2139 flat specimen, the measured crack opening loads are relatively stable. No significant influence of the repositioning of the clip gauge is observed.

### 4.1.3 Fracture surface observation

Figure 4.6 compares the fracture surfaces of AA2139 and AA2198 panels at macroscopic scale. Both of the two AA2139 panels show flat crack surfaces with smooth single shear lips. The shear lips started to develop at positions marked by the white arrows and become stabilized in morphology at positions marked by the black arrows, where the whole section of the fracture surface is  $45^\circ$  inclined. In the panels of AA2198, the fracture surface is much more tortuous due to the development of complex shear lip morphology. In the flat panel double shear lips firstly initiated at a half crack length of 30 mm, which are accompanied by a deviation of crack path around  $10^\circ$ . In contrast with the gradual rotation of the crack plane during the shear lip development in AA2139 specimens, abrupt changes of the shear lip plane are usually observed in AA2198 specimens as marked by the squares in Figure 4.6. In the crenellated panel, those abrupt changes are usually found associated with the thickness steps in the crenellations. In the crenellated panels very sharp shear lips are found along the crenellated side since the beginning of the fatigue tests. Those very sharp shear lips are less than 1 mm wide with the local crack surface about  $70^\circ$  inclined to the original crack plane. At large crack lengths ( $a > 95$  mm) stable single shear lips are observed in both flat and crenellated panels as those observed in the AA2139 panels.

The fracture surfaces of both materials can be generally divided into regions of tensile mode decohesion and regions of shear mode decohesion as shown in Figure 4.7. The shear mode decohesion is found always initiated at the specimen surface. In AA2139 specimens, after the initiation, the shear mode decohesion is found constrained in narrow stripes near both surfaces of the specimens for a considerable distance of crack extension. Meanwhile, with further extension of crack the whole crack surface becomes gradually inclined, which in the end has an angle about the  $45^\circ$  with respect to loading direction. During this period, the distinction between regions of tensile mode decohesion and regions of shear mode decohesion also becomes obscured. In contrast, in AA2198 specimens the shear mode decohesion, once it is initiated, will extend quickly across the whole crack surface except those very sharp shear lips formed along the crenellated side at small crack lengths. The borders between the tensile mode and shear mode decohesions are also much more distinct. In addition, in AA2198 specimens the inclination angles of the shear mode decohesion zones are usually found larger than in AA2139 specimens.

A closer examination of the crack surface in the tensile mode region under SEM shows a flat crack surface at the microscopic scale in both materials, which

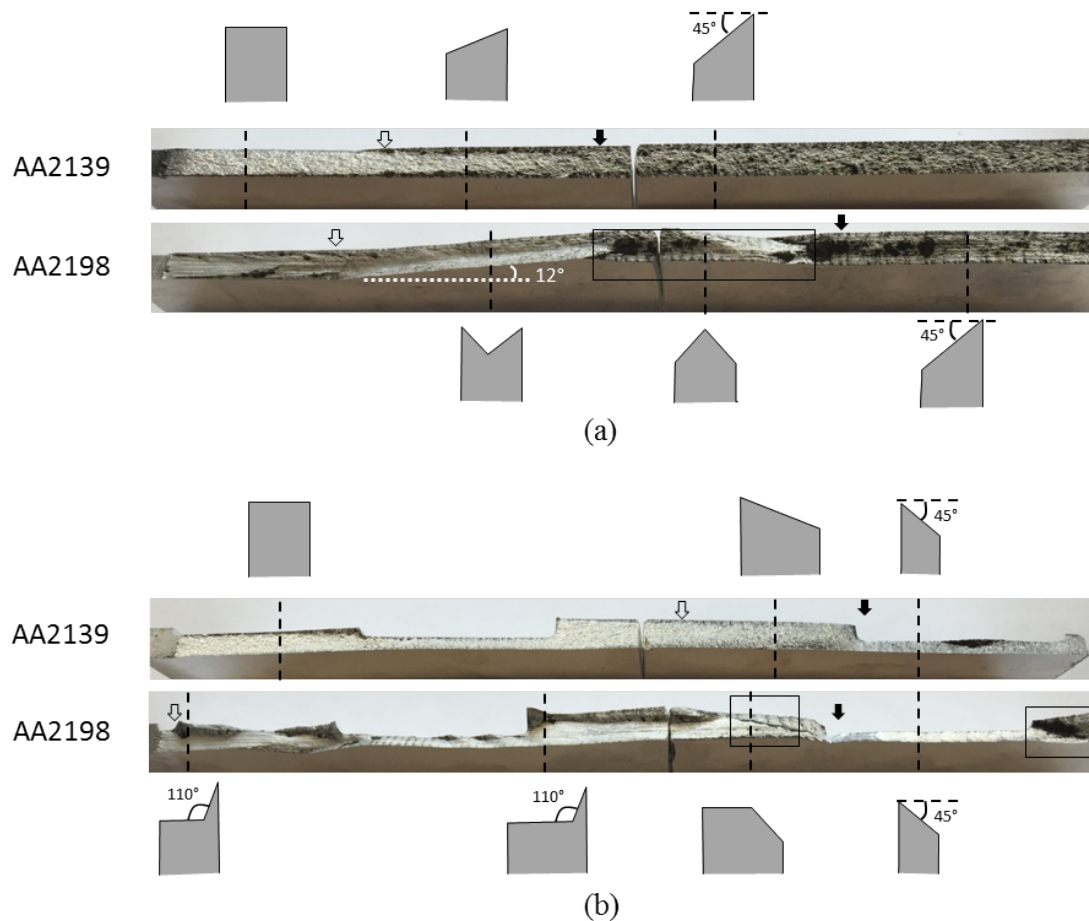


Figure 4.6. Fracture surface of (a) flat panels and (b) crenellated panels and the different morphology of shear lips developed at different positions. Schematic sketches of the transverse slice of fracture surface are placed right above or below the positions where they are cut. The start point of shear lips and the position where they have been fully developed are marked by white and black arrows respectively. The abrupt changes of cracking plane are marked by rectangles.

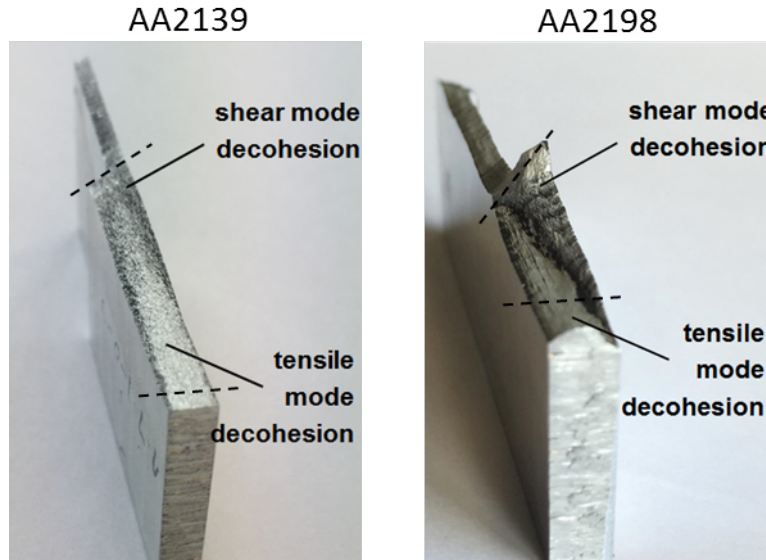


Figure 4.7. The transitions from tensile mode decohesion to shear mode decohesion on the fracture surface of AA2139 and AA2198. The dashed lines indicate the local inclination of the fracture surface.

are compared with the corresponding microstructures revealed under the optical microscope (Figure 4.8). The irregularities on the surface are found mostly correlated with the positions of grain boundaries as indicated by the optical micrograph. Within the grains the crack surface shows smooth appearance with visible striations, the normal of which is found aligned well with the major loading direction.

Despite both materials show amorphous appearance in the shear mode region (the shear lips), there are two significant differences. Firstly, as shown in Figure 4.9, abrasion zones near the sharp shear lips are usually observed in the AA2198 crenellated specimen, which are characterized by straight scratches in the direction perpendicular to the crack propagation direction. However, such abrasion zone is never seen in AA2139 specimens.

Secondly, in specimens made of AA2139, isolated islands of shear mode decohesion can be found in the region of tensile mode decohesion (Figure 4.10). Those islands have higher density near the specimen surfaces and relatively lower density towards the center of the panels. With increasing crack length, the area fraction of those islands of shear mode decohesion increases. Then, instead of being small isolated regions they begin to form large bands, which finally dominate the whole fracture surface. This process accompanies with the gradual increase of inclination angle of the fracture surface at the macroscopic scale. When the inclination angle is approaching  $45^\circ$ , the fracture surface is dominated by shear mode decohesion with several islands of tensile mode decohesion distributed in between. In specimens of AA2198, such embedded distribution of shear mode decohesion are hardly seen, where the regions of different modes of decohesion are clearly separated with a distinct border.

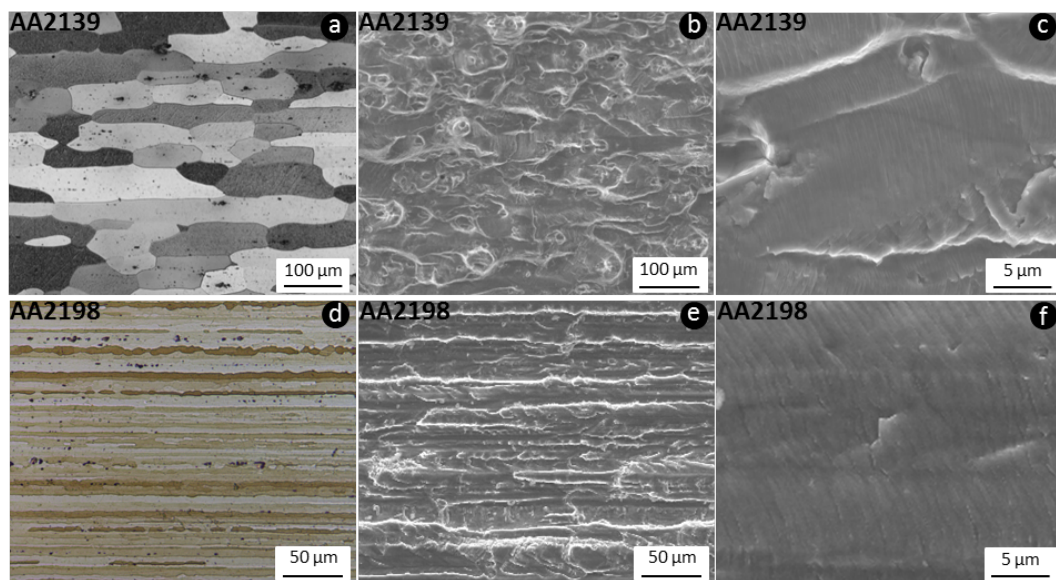


Figure 4.8. SEM micrographs of crack surfaces (b, c, e, f) of the two materials where the fatigue cracks grow in tensile mode and the comparison of crack surface morphology with the corresponding base material microstructure (a, d).

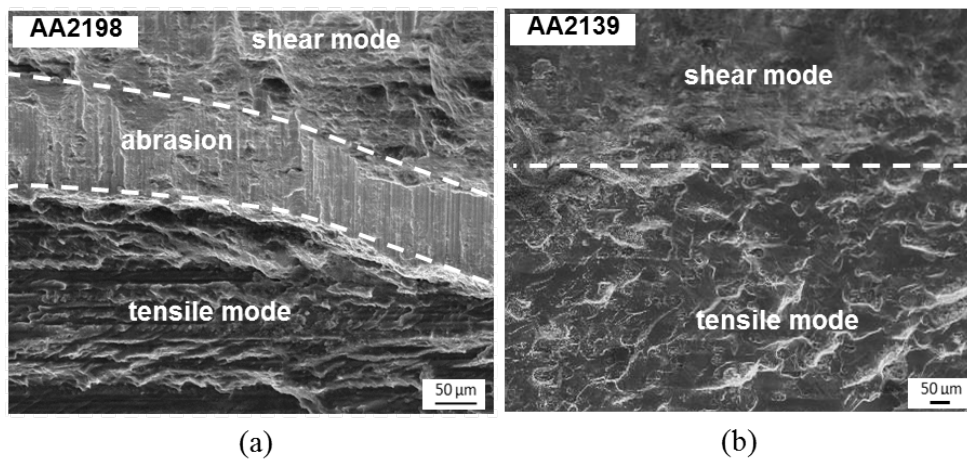


Figure 4.9. SEM micrographs of the transition regions between the shear mode decohesion and the tensile mode decohesion on the crack surface of AA2198 (a) and AA2139 (b).

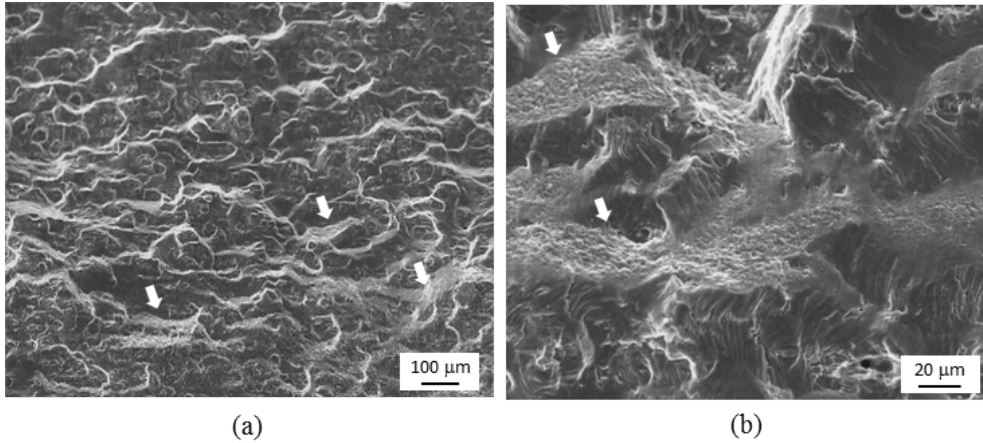


Figure 4.10. (a) Local shear mode decohesions (marked by arrows) occur in the tensile mode decohesion region on the crack surface of AA2139. (b) detailed view of the local shear-mode decohesions.

#### 4.1.4 Observations on the deformation state of the panels under biaxial loads

FEM simulations of biaxially loaded crenellated specimens show that there is an increasingly pronounced out of plane bending of the panels with increasing biaxial load ratio as shown in Figure 4.11. However, this phenomenon is found to be absent in simulations of flat panels. Considering the geometric symmetry of flat and crenellated specimens, the out of plane bending should be due to the reduced stiffness at the crenellated side in a direction perpendicular to the crenellations. Thus, when the minor load is applied in this direction as shown in the experimental setup (Figure 3.1), the crenellated side has a larger elongation compared to the opposite side and thus promotes the out of plane bending. In experiments, out of plane movements were actually observed in flat specimens due to the slight sinking of the panel center under gravity during the unloading phase. However, its magnitude is found to be much smaller than that in the fatigue tests of crenellated panels.

## 4.2 Discussion

### 4.2.1 Influences of texture on the shear lip formation

The distinct textures of the two materials are related with the different heat treatment conditions. The T351 heat treated AA2139 is only slightly stretched to 1-2% after the solution treatment whereas the T3 heat treatment of AA2198 involves large amount of cold working [79]. The very sharp Brass texture observed in AA2198 is very typical for cold rolled FCC metals [80]. The strong S texture components near the surface of the plate are due to the increasing degree of deformation caused by the direct contact with rollers. The large amount of cold working in AA2198 is also reflected by the pancake grain structure shown in Figure 4.1.

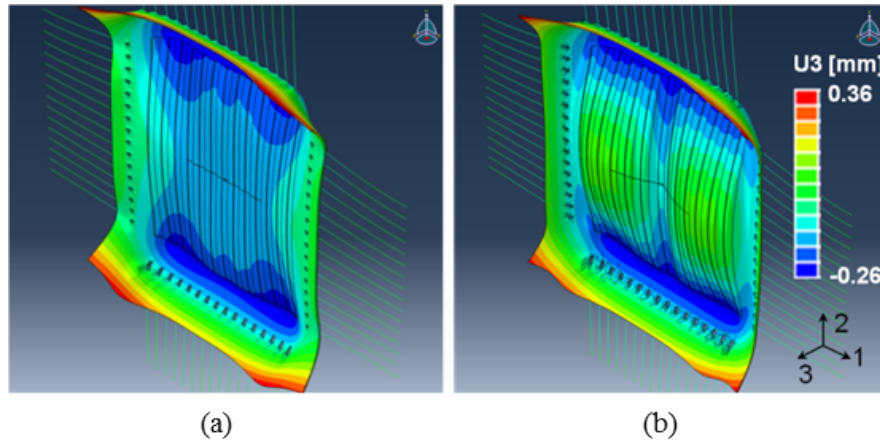


Figure 4.11. Out of plane bending of crenellated panels indicated by FEM simulation, which are loaded under 2 different biaxial load ratios:  $\chi = 0.1$  (a) and  $\chi = 0.5$  (b).

The distinct textures of the materials can significantly influence the development of shear lips. This has been revealed by the experiments of several previous researchers. Pook and Greenman [81] found that in Mg alloy sheets with strong rolled texture, where the base slip systems well align with rolled plane, the shear lips, which usually present along  $45^\circ$  inclined planes, were totally suppressed. Tchorzewski and Hutchinson found the width of shear lips was strongly influenced by the orientation of the fracture plane in the textured Ti-6Al-4V alloy [82]. However, to the best knowledge of the author a systematic analysis concerning the correlation between texture and the development of shear lips has not yet been made.

The detailed influences of texture can be analyzed in 2 aspects: on the shear lip initiation and on the morphology of the developed shear lips.

### Influences of texture on shear lip initiation

When the shear lips start to initiate, according to Schijve [33], the initial tensile mode decohesion of materials is locally overruled by the shear mode decohesion normally along the plane of maximum shear stress with a  $45^\circ$  inclination to the external load. This process is accompanied with a significant change in dislocation motion at the crack tip. It involves much enhanced movements of specific slip systems, the slip planes of which have good alignment with the plane of shear decohesion. This has been revealed by the asymmetric plastic zone shape at shear lips as observed by Zuidema using a special pretreatment of specimens with photographic lacquer [83]. In the strong textured material AA2198, the easy sliding planes - the  $\{111\}$  planes of the grains are not randomly orientated but concentrate in specific orientations. If they have a good alignment with maximum shear stress planes, they can contribute a lot to the slip that is necessary for the shear lip formation. In the opposite, if all the easy sliding planes of sharply textured materials concentrate along a certain plane that has the largest deviation from the planes of maximum shear stress like rolled Mg plates, the formation of

shear lips can be suppressed as observed in the experiments of Pook and Greenman [81].

For the sharply textured AA2198 specimens, the ideal orientations of the  $\{111\}$  planes with respect to the sample frame can be determined based on the EBSD texture analysis (see section 4.1.1). In Figure 4.12 they are schematically sketched within the frame of the specimen. As it can be seen that the  $(11\bar{1})$  plane coincides with the initial crack plane in tensile mode while the other three  $\{111\}$  planes form a regular tetrahedron above the crack plane with one corner pointing to the opposite of the crack growth direction. The idealized  $(\bar{1}11)$  and  $(1\bar{1}1)$  planes of the material have good alignment with the  $45^\circ$  inclined planes of maximum shear stress. Therefore considering the abundance of slip systems that can be easily activated for the shear mode decohesion, AA2198 should potentially favor the formation of shear lips.

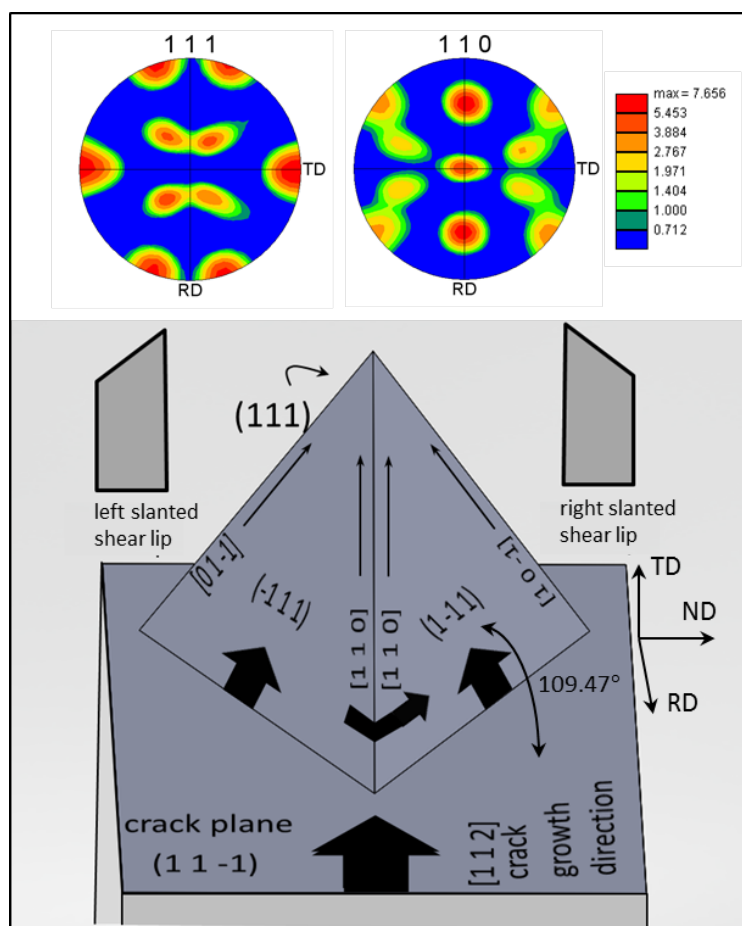


Figure 4.12. The correlation of shear lip morphology with the texture of AA2198.

In addition, for Al-Li alloys, to which AA2198 belongs, sharp deformation textures were often reported to promote crystallographic cracking along the  $\{111\}$  close-packed planes [43, 47, 48, 79, 84]. Normally such crystallographic cracking mostly occurs in the lower  $\Delta K$  range [38], where the constraint for planar slip is small due to the small plastic zone size (comparable to grain size). In textured Al-Li alloys such slip planarity is much enhanced not only due to the coherent

hardening phases [85] but also due to the weakened grain boundary, which is one major barrier for planar slip. Since in sharp textured material the misorientations between the close packed  $\{111\}$  planes of adjacent grains are small, the slip bands developed along those planes can cross several grains and offer a preferential crack path [45]. This tendency of shear mode cracking along  $\{111\}$  planes of sharp textured Al-Li alloy probably has strong influence on the formation of shear lips. Because as shown in Figure 4.6 in the crenellated AA2198 specimen the angle between the tensile-mode crack plane and that of shear mode is frequently observed to be roughly  $110^\circ$ , which is the dihedral angle between different  $\{111\}$  planes as shown in Figure 4.12. Furthermore, shear lips normally initiate from the surface of the specimens. It is also the location, where the cracking along  $\{111\}$  planes are most likely to occur due to the low constraints for planar slip. It should be noted that, as shown in Figure 4.6, those  $110^\circ$  inclined shear lips disappear at large crack lengths, where the  $45^\circ$  inclined shear lips are observed as in AA2139 specimens. This is probably due to that in the beginning the formation of shear lips heavily depends on the slip systems on  $\{111\}$  planes with most advantageous orientations, whereas at large crack lengths the large  $\Delta K$  can activate cyclic slips on more slip systems, which then favor the shear mode decohesion along the plane of maximum shear stress.

Therefore, considering the favorable orientations of  $\{111\}$  easy sliding planes and the intrinsic tendency of crack formation along such planes in sharp textured AA2198, shear lips should initiate more easily in the AA2198 specimens compared to the AA2139 specimens. This is supported by the experimental observations. For flat specimens, as shown in Figure 4.6, the first shear lip of the AA2198 panel initiates at a crack length, which is about 10 mm shorter than in the AA2139 panel. According to Zuidema [32], for the initiation of shear lips during fatigue cracking a minimum  $\Delta K_{\text{eff}}$  must be reached. Considering the same geometry and loading condition as well as the similar crack closure level in both specimens at the beginning of the tests (see Figure 4.5 b), the minimum  $\Delta K_{\text{eff}}$  required for shear lip initiation is therefore reduced in the AA2198 panel, which indicates an easier initiation of shear lips.

For crenellated specimen, such a trend is even more obvious. As shown in Figure 4.6, the first shear lip is found only 1-2 millimeters from the starting notch in AA2198 panel. This unexpected early formation of shear lips is attributed to the concentrated shear along the  $45^\circ$  inclined plane at the edges of the buckling cracking surface [31], when the out-of-plane bending of crenellated specimens is promoted under biaxial loads (section 4.1.4). However, under the same favorable condition, the initiation of shear lip dose not occur at the same crack lengths in AA2139 crenellated specimen, which is on the contrary delayed towards much larger crack lengths due to the significantly reduced  $\Delta K_{\text{eff}}$  by crenellations.

### Influences of texture on shear lip morphology

The distinct morphology of shear lips developed in AA2139 and AA2198 specimens should have their origins in their different textures. As shown in Figure 4.6 shear lips in sharply textured AA2198 specimens have a sharp and tortuous morphology whereas in non-textured AA2139 the development of shear lips are rather

smooth, which show a gradual transition of crack plane from the perpendicular orientation to the  $45^\circ$  inclined orientation.

The first impact of texture is considered to be on the sharpness of the shear lips. As explained in section 4.2.1, the  $\{111\}$  easy sliding planes provide favorable conditions for the formation of shear lips. In the sharply textured AA2198, since misorientations between neighbouring grains are small, once the shear mode decohesion is initiated at surface along the most advantageous easy sliding plane it can propagate quickly towards the interior of the specimen as shown in Figure 4.7 creating a sharp transition of orientations in the local crack plane with a distinct border between the tensile mode and shear mode decohesion regions.

In the randomly-textured AA2139, the propagation of shear mode decohesion towards the interior of the material can be largely inhibited by the presence of large amount of grains with unfavorable orientations. As a result, the shear decohesion zone is confined in a very narrow strip along both margins of crack surface as shown in Figure 4.7. However, near the surface but inside the tensile mode region shear mode decohesion can also be initiated at discrete sites due to the plane stress condition near the surface and the advantageous orientations of some discrete grains. With increasing crack length, both the enhanced plane stress condition due to the enlarged plastic zone size and the increased  $\Delta K_{\text{eff}}$  can promote the shear mode decohesion deeper inside the materials and in more grains with relatively less advantageous orientations. Therefore, with increasing crack length shear mode decohesion should occur in more "islands" across the fracture surface. In addition, the higher the fraction of the shear mode decohesion region is, the larger the inclination of the local crack surface becomes. As a result, as shown in Figure 4.7 with the propagation of the crack a smooth transition of the crack surface orientation is observed from the tensile mode to a complete shear mode.

Besides the sharpness of the shear lips, another difference between the two materials is that the orientations of shear mode decohesion plane are often observed to change abruptly in AA2198, which is never observed in AA2139. This difference can be understood by a detailed analysis of the activation of slip systems in AA2198. As shown in Table 4.1, the Schmid-Factors of the 12 slip systems on the four  $\{111\}$  planes were calculated based on the previous texture analysis presuming a tensile stress field perpendicular to the original crack plane. It can be seen that 6 slip systems of them are more advantageous to be activated. Since  $(-111)$  and  $(1-11)$  planes have the best alignment with the maximum shear stress planes, which are  $45^\circ$  inclined to the side surfaces of the panels, the activation of slip systems  $(-111)[01-1]$ ,  $(-111)[110]$ ,  $(1-11)[10-1]$  and  $(1-11)[110]$  will probably have the greatest contribution to the shear lip formation. The co-activation of slip systems  $(-111)[01-1]$  and  $(-111)[110]$  will favor shear decohesions along the  $(-111)$  plane and will finally generate a left-slanted shear lip; the co-activation of slip systems  $(1-11)[10-1]$  and  $(1-11)[110]$  will favor shear decohesions along the  $(1-11)$  plane and will finally generate a right-slanted shear lip. As shown in Figure 4.12 the  $(-111)$  and  $(1-11)$  planes are symmetric and equally advantageous in initiating shear lips. If shear lips are initiated along both planes but on different sides of panel surface then a double shear lip forms as observed in the AA2198 flat panel. This equality of  $(-111)$  and  $(1-11)$  planes also implies there can be a competition of activated

slips along those planes. Local disturbances can probably disadvantage the shear mode decohesion along one  $\{111\}$  plane that is initially favored and promote shear mode cracking on the other  $\{111\}$  plane. For instance, abrupt changes of the orientations of shear lip planes were frequently observed at the crenellation steps, where the sudden changes of thickness are considered as significant disturbances.

Table 4.1. Schmid-Factors of different slip systems in the strong textured AA2198 panels subjected to tensile stress field that is perpendicular to the initial cracking plane.

Slip System	Schmid-Factor	Slip System	Schmid-Factor
(111) [-110]	0	(1-11) [110]	0
(111) [-101]	0.272	(1-11) [-101]	0.272
(111) [01-1]	0.272	(1-11) [011]	0.272
(-111) [110]	0.272	(111) [-110]	0
(-111) [101]	0	(111) [101]	0
(-111) [01-1]	0.272	(111) [011]	0

In summary, the sharp texture of AA2198 specimens promotes an early and extensive formation of shear lips with sharp and tortuous morphology. In contrast, smooth shear lips were formed in AA2139 specimens due to the random nature of grain orientations in the material.

#### 4.2.2 Influences of shear lips on the crack growth behavior

The experimental results indicates there is an intimate correlation between the development of sharp shear lips and the change in fatigue crack growth rate. In AA2138 specimens, since there is no formation of sharp shear lips, the  $da/dN$  values of both flat and crenellated specimens form a straight line in the  $da/dN$ - $\Delta K$  plot (Figure 4.4 b). In contrast, in AA2198 specimens, the formation of sharp shear lips shows large impact on the  $da/dN$  values. As seen in Figure 4.4 b in the low  $\Delta K$  range ( $\Delta K < 15 \text{ MPa} \cdot \text{m}^{1/2}$ ), where the shear lips in AA2198 flat specimens are still not fully developed, the  $da/dN$  values tend to be close to those of AA2139 panels, in which the cracks also grow in tensile mode. In contrast, sharp shear lips have already formed in AA2198 crenellated specimen in the same  $\Delta K$  range. Accordingly, the  $da/dN$  values are found significantly lower. Such a discrepancy of  $da/dN$  values between the AA2198 flat and crenellated specimens is observed to be reduced significantly after the initiation of shear lips in the AA2198 flat specimen. Then with further increasing  $\Delta K$ , large fluctuations of  $da/dN$  values are observed in both AA2198 flat and crenellated specimens, which are probably attributed to the abrupt change of local shear lip planes such as those at the crenellation steps as shown in Figure 4.6. In the high  $\Delta K$  range ( $\Delta K > 40 \text{ MPa} \cdot \text{m}^{1/2}$ ), when such tortuosity of shear lips disappears as mentioned in section 4.2.1, the  $da/dN$  values of both specimens are observed to tend to approach those of the AA2139 specimens again.

Based on the above description, it can be seen that when the complication of a

varying shear lip morphology does not exist like in the low and high  $\Delta K$  ranges, fatigue cracks in both material grow at very similar rate. This is in agreement with the observations of previous researchers that the intrinsic resistance of many Al alloys to fatigue crack growth are very close to each other in the Paris region and their actual fatigue performance generally scale with the corresponding crack closure level [44, 86, 87].

Therefore, it is quite possible that the superior fatigue performance of AA2198 is mainly attributed to the enhanced crack closure brought by the sharp shear lips. The impact of shear lips on crack closure behavior have been reported by different researchers, which considered shear lips as favorable sites for surface contact during the process of crack closure [36, 88–91]. In our experiments, black fretting traces are usually found at the cuspidate shear lips and at the ridges of the abrupt change of shear planes as shown in Figure 4.6. Such fretting product has been considered by Schijve as the evidence for sliding contacts at shear lips [17]. The variation of crack opening load measured along crack path is also in good accordance with the local shear lip morphology. As shown in Figure 4.5, before the development of sharp shear lips in AA2198 flat specimen ( $a < 30$  mm), the crack opening loads are roughly the same as in AA2139 specimens, where the crack surfaces are also flat and smooth. In contrast, in the same range of half crack lengths the crack opening load in AA2198 crenellated specimen is significantly higher, which can be correlated with the early formation of rough shear lips.

Such crack closure at shear lips can be classified into the category of contact shielding due to wedging mechanism according to Ritchie [35]. The magnitude of the wedging effect depends on both the degree of asperity of the crack surface and the extent of mismatch between the mating surfaces, which can originate from in-plane or anti-plane shear movement of the two surfaces. In our case, this mismatch should be mainly provided by the anti-plane displacement of crack surfaces due to the lower out-of-plane constraint in thin shell structures. This is also supported by the observed traces of abrasion, which is perpendicular to the crack growth direction as shown in Figure 4.9. Since the out-of-plane movement is enhanced in the crenellated specimens due to asymmetric geometry at the two sides as shown in Figure 4.11, the sliding crack closure is expected to be higher in the crenellated specimen. This is in good agreement with the observed higher averaged crack opening load and generally lower positions of data points in the  $da/dN - \Delta K$  plot (Figure 4.4 b) compared to AA2198 flat specimen. The relations between the presence of sliding crack closure and the shear lip morphology as well as the deformation mode of specimens are summarized in Table 4.2.

In summary, the additional fatigue life improvement observed in AA2198 crenellated specimen compared to the case of AA2139 is attributed to the enhanced crack closure level due to a relatively early formation of sharp shear lips as well as an enhanced sliding contact at the shear lips due to the out of plane bending movement under biaxial loads.

Table 4.2. Influences of shear lip morphology and the deformation state of the structure on crack closure behavior.

	<b>flat</b>	<b>crenellated</b>
AA2139	smooth shear lip; no out of plane bending => no sliding crack closure	smooth shear lip; out of plane bending => no sliding crack closure
AA2198	sharp and tortuous shear lip; no out of plane bending => small sliding crack closure	sharp and tortuous shear lip; out of plane bending => large sliding crack closure

### 4.2.3 The technical significance of sliding crack closure at shear lips in comparison with roughness induced crack closure

There are several significant differences between the sliding crack closure at shear lips and the conventional roughness induced crack closure (RICC), although both of them depend on similar wedging mechanism for toughening. The first difference lies in the magnitude of fracture surface asperities. Since the coarse fracture surface in RICC is primarily due to the crystallographic crack growth in the low  $\Delta K$  range [37], the sizes of asperities are at the same magnitude of grain sizes and are normally around tens of micrometers. Although the asperity size can be further enhanced in material systems with propensity of planar slip and by the sharp material texture [43, 47], they can hardly exceed the magnitude of hundreds of micrometers. In contrast, the formation of sharp and tortuous shear lips lead to huge surface asperities with sizes of millimeters, which are at least one magnitude larger.

The second difference lies in the relative displacement that leads to the mismatch of the mating surfaces. RICC mainly depends on mode II (in-plane shear) crack surface displacement either due to the kinematic irreversibility of the single shear displacement of the crack tip in the local stage I crack growth [38] or due to the asymmetric plastic deformation between the plastic wakes of the upper and lower crack surfaces [42]. Such a displacement was found to be only a portion of the asperity size. Furthermore, its magnitude is normally homogeneous along the crack path. In contrast, the sliding crack closure at shear lips depends on the mode III (anti-plane shear) displacement as explained in section 4.2.2. Such anti-plane shear around the crack tip leads to increasing mismatch between the two crack surfaces as the distance to the crack tip increases. As a result, the mismatch of the sliding crack closure at shear lips is considered to be much larger than that in RICC especially at a distance from the crack tip.

These two differences lead to the fact that for RICC and for sliding crack closure at shear lips the crack closure actually occurs in different regions of crack surfaces. For RICC, the region of crack closure is observed to be concentrated in a small zone near the crack tip (normally within 1 mm) [92]. This is due to the dramatic increase of the crack opening with increasing distance from the crack tip, which turns out to be much larger than the asperity height. For the sliding crack closure

at shear lips due to both the huge surface asperities and the characteristic of an increasing mismatch of the mating surfaces with increasing distance, the surface contact can occur at a considerable length from the crack tip. Zuidema and Krabbe [83] have observed the wedging at sharp shear lips in a range between 3 mm and 10 mm away from the crack tip. Such an extended closure range can be reflected by the measured profile of crack opening load with highly sensitive near-tip gauges as reported by some previous researchers [93,94]. This is also observed in this study. As shown in Figure 4.5, for the AA2198 crenellated specimen, where there is an extensive formation of sharp shear lips, a periodic variation of measured crack opening load with the change of  $\delta_5$  clip gauge positions has been observed. When the  $\delta_5$  clip gauge was just applied at the crack tip, the highest crack opening loads were observed. Then with further extension of the crack, there was an apparent decrease of the measured values. Such a position dependence of the measured results originates from the fact that the loss of surface contact upon loading occurs in a progressive way towards the crack tip [88,95], especially when the crack surface is wedged by shear lips over a large distance as mentioned above. The closer the clip gauge is with respect to the crack tip, the later the loss of surface contact will proceed to the position of clip gauge upon uploading. In such a case, a later transition from the nonlinear to linear relation in the displacement-load curve is observed and thus a higher measured crack opening load is obtained as explained in Figure 4.13. For AA2139 specimens, due to the absence of sharp shear lips there is no apparent variation of crack opening loads with the measuring positions.

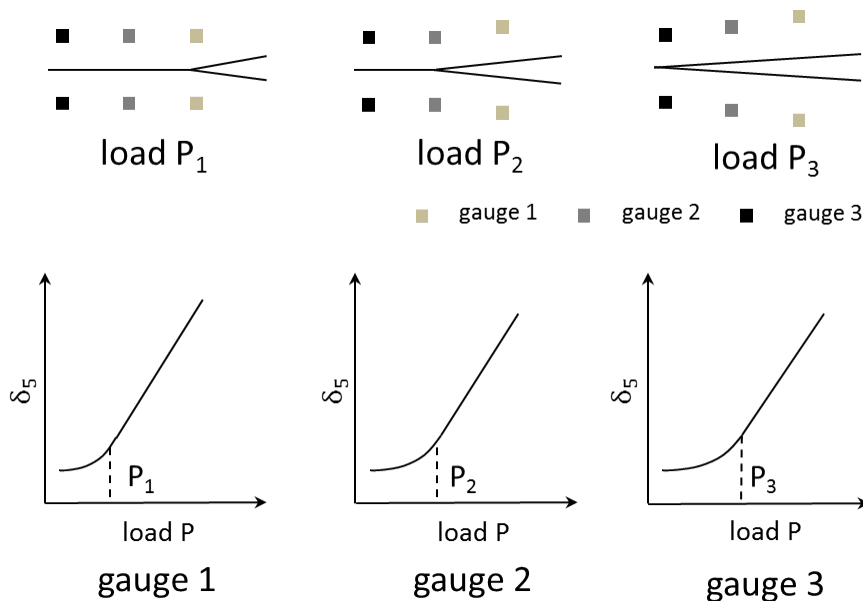


Figure 4.13. The influence of the clip gauge position on the measured crack opening load due to the extensive wedging on sharp shear lips.

The much extended wedging area of the sliding crack closure on shear lips leads to an enhanced crack closure in relatively high  $\Delta K$  ranges in comparison with RICC. According to Suresh [37] the RICC is mostly significant in the low

$\Delta K$  range. With increasing  $\Delta K$  the crack closure level of materials with RICC is significantly reduced, which was found dependent on the fracture surface roughness [96] in different age-hardened Al alloys as shown in Figure 4.14. When  $\Delta K$  is above a critical value (e.g.  $5.5 \text{ MPa} \cdot \text{m}^{1/2}$  for alloy 1 with the smoothest crack surface and about  $20 \text{ MPa} \cdot \text{m}^{1/2}$  for alloy 3 with the roughest crack surface), the initial difference in crack closure level between different alloys disappears and their  $da/dN$ - $\Delta K$  curves tend to converge into a single curve. Borrego et al. [96] consider that above the aforementioned critical  $\Delta K$  value RICC diminishes and plasticity induced crack closure (RICC) becomes dominant, which remains basically constant at different  $\Delta K$ . The diminishing of the RICC with increasing  $\Delta K$  has two origins. Firstly, it results from the more enhanced crack tip opening at larger  $\Delta K$ , which makes the wedging at the crack tip more difficult. Secondly, it is due to the greatly reduced fracture surface roughness after the transition from crystallographic crack growth into stage II crack growth [38], where the plastic zone can encompass many grains. In our case, the plastic zone size at the beginning of our tests are estimated to be around  $100 \mu\text{m}$  [97], which is significantly larger than the grain sizes of both materials shown in section 4.1.1. This is in good agreement with the observed flat crack surface in tensile mode decohesion zone, which is characteristic for stage II crack growth. Thus the influence of RICC had already diminished in both materials since the start of the tests.

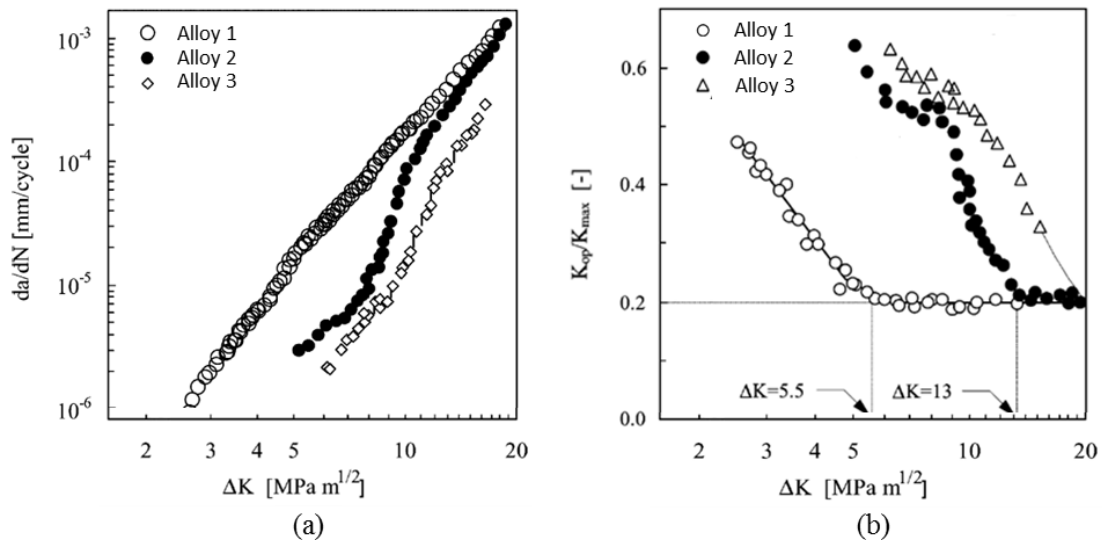


Figure 4.14. Fatigue crack growth rates (a) and crack closure data (b) at various  $\Delta K$  values for different age-hardened Al alloys with different fracture surface roughnesses (alloy 1 and alloy 3 have the smallest and largest roughness on the fracture surface respectively). (after [96])

In contrast, the influence of sliding closure on shear lips can span a broad  $\Delta K$  range in the Paris region (up to  $40 \text{ MPa} \cdot \text{m}^{1/2}$  as shown in Figure 4.4 b). This is due to the fact that unlike RICC, in which the rough crack surface disappears with increasing  $\Delta K$ , the tortuous morphology introduced by sharp shear lips remains stable in a wide range of the Paris region. Most important, the extended wedging

on the surface due to the large asperity size and the large mismatch of crack surfaces makes it insensitive to the increased crack tip opening with increasing  $\Delta K$ .

In summary, compared to RICC which is normally only pronounced in low  $\Delta K$ , the sliding closure at shear lips is considered to be more relevant and potentially more beneficial to the damage tolerant designs of fuselage structures, since the growth of macroscopic cracks considered by this design principle lies mostly in the Paris region, where this type of crack closure has significant effects.

### 4.3 Summary of this chapter

The main points of the chapter are summarized as follows:

1. The materials used in the crenellated structures can significantly influence the effectiveness of crenellations. Fatigue life improvement via crenellations doubles in the strong textured material AA2198 compared to the randomly textured material AA2139.
2. Random texture leads to a smooth shear lip morphology, whereas strong brass texture leads to a tortuous shear lip morphology. Especially, in the crenellated specimens with strong texture, the formations of very sharp shear lips along the crenellation side are promoted, the orientations of which are found correlated well with those of  $\{111\}$  planes according to the texture analysis.
3. The out of plane movement of crenellated panels under biaxial loads also favors an enhanced crack surface interference at those rough shear lips.
4. The accompanying sliding crack closure contributes to the additional fatigue life improvement observed in the AA2198 crenellated panel.

## 5. Optimization of crenellation geometry via genetic algorithm

If the complications of shear lips detailed in the previous chapter do not need to be considered such as in material AA2139,  $da/dN$  is linearly correlated with the nominal driving force - the stress intensity factor range under double logarithm as characterized by Paris Law as shown in Figure 4.4 b (section 4.1.2). In such a case, by calculating the stress intensity factors at different crack lengths and under various external loads using FEM simulation, the fatigue performance of crenellation designs with different geometries can be predicted with rather good accuracy. Therefore it is possible to find out the optimum geometries of crenellations that can provide the largest fatigue crack retardation based on the modulation of the driving force with the help of FEM simulation. This chapter provides an automated and reliable approach to fulfill this aim by coupling the FEM simulation with an optimizer. Here a genetic algorithm is chosen as the most ideal optimizer for the following reasons. Firstly, it does not need any pre-knowledge or mathematic formulation of the optimization problem. It can work well fully dependent on the feedback from FEM simulations. Secondly, as a global optimizer the genetic algorithm is quite robust to local optimums, which is very suitable to deal with multimodal optimization problems with high dimensionality. Thirdly, as a population-based approach, the genetic algorithm is also very capable of dealing with the more practical multi-objective optimizations, the results of which provide the best tradeoff between conflicting design objectives such as increasing fatigue performance and decreasing structural weight in our case (to be addressed in section 5.5). Finally, the algorithm is capable of dealing with both continuous and discrete variables or a hybrid of them. This property enables the user to include a broad spectrum of design variables with distinct characteristics in the optimization problems (to be addressed in section 5.6).

In following sections, the accuracy of the FEM model and its capacity for fatigue life prediction will be firstly demonstrated using experimental observations. When this is on the solid ground the implementation of the genetic algorithm in the present optimization problem will be explained in detail. Subsequently, the optimization results will be presented and analyzed together with a discussion about the computational cost. In the next step, the optimized designs are verified by a different approach of optimization with multiple design objectives. The effectiveness of the optimized design in the fatigue life improvement is further experimentally validated. Finally, a tentative study is made to perform an incorporated optimization hybridizing crenellations with the laser heating technique

with the aim of further pushing the limits of fatigue life improvements when using either of the two techniques.

## 5.1 Validation of the FEM model used for fatigue life prediction

The FEM model described in the material and method part was validated by the fatigue tests of flat and crenellated specimens with the material AA2139. The purpose is to confirm that the impact of the geometrical changes on the fatigue performance due to the application of crenellation can be correctly predicted by the FEM modeling. To this end, the FEM models were firstly examined in terms of correctly characterizing the elastic deformation of the specimens, which is the precondition for an accurate estimation of the stress intensity factor. This is ensured by a good agreement (the deviations are mostly within 5%) between the strain measurements via the applied strain gauges in experiments and the strain values extracted at the corresponding locations from FEM models after simulations (Figure 5.1). The positions of the strain gauges are shown in Figure 5.2.

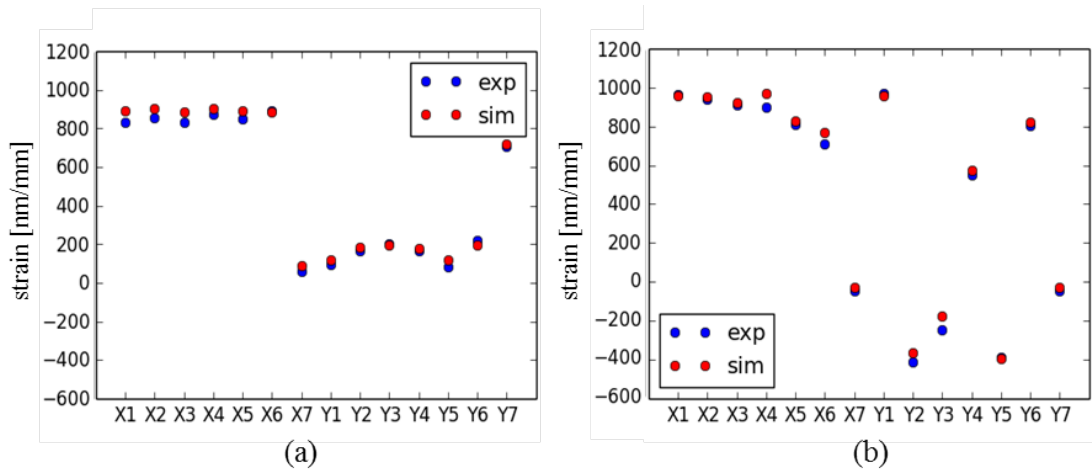


Figure 5.1. Comparison between the measured strains by strain gauges (exp) and the corresponding predicted values extracted from FEM models (sim) at different positions of the flat (a) and crenellated (b) specimens.

Then the FEM model was further validated based on a cross-validation between different specimens. The experimentally measured fatigue crack propagation rates ( $da/dN$ ) are plotted against the corresponding stress intensity factor ranges,  $\Delta K$ , extracted from the simulations as shown in Figure 5.3 a. The data points of all the different specimens fall into the same narrow scatter band with a linear trend as dictated by Paris Law. The Paris constants  $C$  and  $m$  were obtained through a linear fitting of the experimental data under double logarithm, which is marked by the blue line in Figure 5.3 a. Based on the numerically calculated  $\Delta K$  profile (from  $a_0$  to  $a_f$ ) and the fitted Paris constants, the fatigue life  $N$  is estimated by integrating the inverse of crack propagation rate calculated based on Paris's Law:

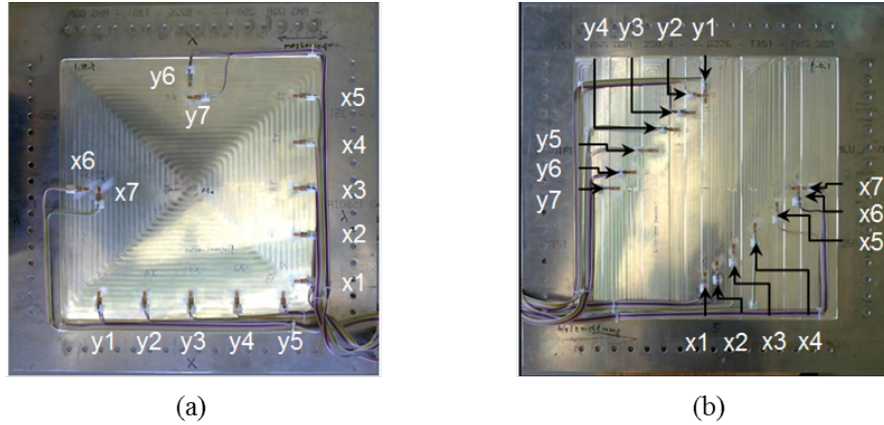


Figure 5.2. Positions of strain gauges on the surfaces of the flat (a) and crenellated (b) specimens respectively.

$$N = \int_{a_0}^{a_f} \frac{1}{da/dN} da = \int_{a_0}^{a_f} \frac{1}{C \cdot \Delta K^m} da \quad (5.1)$$

The calculated fatigue life of both panels based on the stress intensity factor ranges, which are extracted from simulation, is compared with the experimentally measured data. It can be seen that the fatigue life of both specimens can be predicted by the FEM model with good accuracy. Based on the two validation steps the FEM models can be used for the fatigue life predictions of different crenellation patterns in following optimizations.

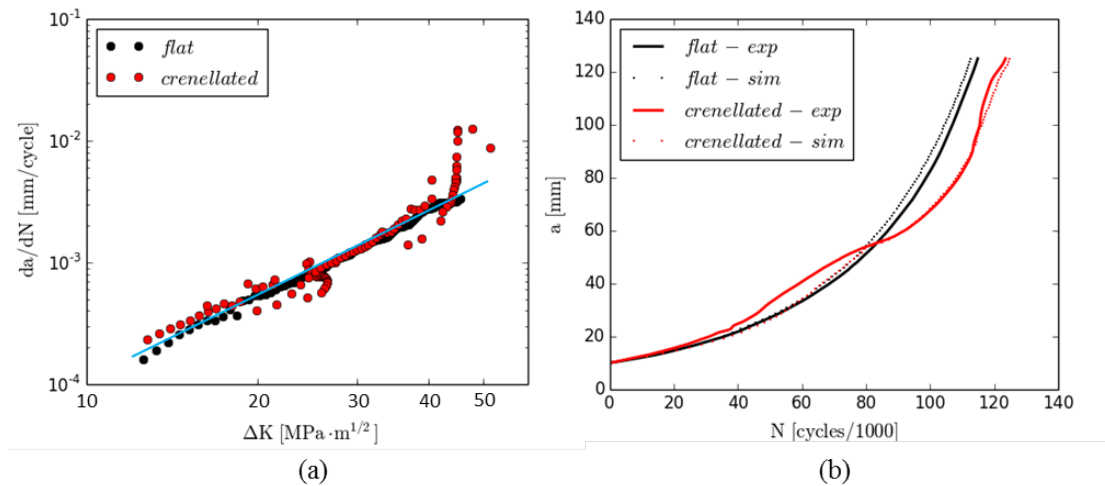


Figure 5.3. (a)  $da/dN$ - $\Delta K$  plot of both flat and crenellated specimens. (b) Comparison between the measured fatigue life (exp) and the predicted one using FEM models (sim) for both the flat and crenellated specimens.

## 5.2 Implementation of the genetic algorithm in the present optimization problem

### 5.2.1 Description of the optimization problem

The optimization of the crenellation pattern is based on the assumption that the crack starts at the root of the stringers, where favorable conditions for fatigue crack initiation have been developed during the welding process, such as high defects content and tensile residual stresses. The aim of the optimization is to maximize the number of cycles needed for growing an initiated crack from a detectable length to the final allowable length (from  $a_0 = 5$  mm to  $a_f = 145$  mm, Figure 5.4) so that the inspection interval can be maximized. The thickness of fuselage skin between those two stringers can vary freely within the following three constrains:

1. inequality constraint - the variation of thickness  $t$  is confined in the following range:  $1.9 \text{ mm} \leq t \leq 4.15 \text{ mm}$ .
2. equality constraint - the crenellated panel should be equivalent in weight to a flat panel with a thickness of 2.9 mm.
3. symmetrical constraint - the crenellation pattern should be symmetrical to the center line of each bay between two stringers since fatigue cracks can initiate from either of the two welding sites.

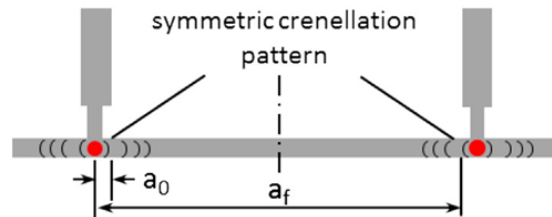


Figure 5.4. Assumed sites for fatigue crack initiation (red dots) and the definition of the optimization problem.

### 5.2.2 Encoding scheme

As shown in Figure 5.5 the fuselage skin between the two stringers is subdivided into many sections. Due to the symmetrical constraint, only half of those sections need to be coded into the chromosome. Binary coding is used to represent the thickness of each section. In the example shown in Figure 5.5 every 3 alleles are translated into the thickness of one section, which can provide 8 different thickness variations bounded by the inequality constraint as specified in the last section. In order to ensure the crenellation patterns always have the same weight, a compensation term is added to each thickness value that is directly translated from 3 alleles. The compensation term  $\varepsilon$  is formulated by:

$$\varepsilon = \left( \sum_{i=0}^{N_t} t_i - t_{\text{flat}} \cdot N_t \right) / N_t \quad (5.2)$$

where,  $t_i$  is the thickness of  $i$ -th section directly translated from the chromosome,  $N_t$  is the half of the number of sections and  $t_{flat} = 2.9$  mm. If the thickness of one section violates the previously mentioned inequality constraint after adding the compensation term, it will stay at the closest boundary of the valid range. The rest of the compensation term for this section will be evenly distributed to all other sections. In this way, any chromosomes will always encode valid solutions satisfying both the equality and inequality constraints.

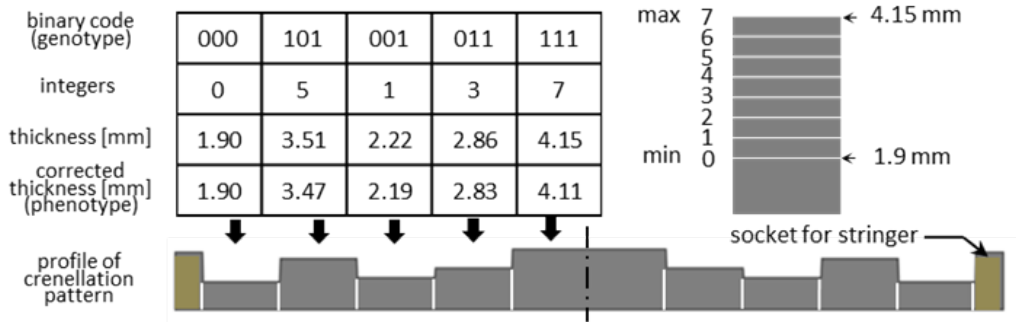


Figure 5.5. The encoding of thickness values into a series of binary code.

### 5.2.3 Progressive refinement of the search space

Encoding the candidate solutions into their corresponding genotypes requires a discretization of the search space, which can occur at two different levels when binary encoding is used. The first level of discretization is due to the fact that the solution needs to be represented by a finite number of design variables, for instance the subdivision of the panel into finite number of thickness sections in our case. The second level is the discretization of the continuous search range of a design variable into  $2^l$  discrete possible values when the variable is encoded by  $l$  alleles.

Similar to the meshing of FEM Models, a finer discretization of search space is expected to bring a higher quality of solutions whereas the computational cost can be larger. In order to avoid the waste of unnecessary computation cost due to the over fine discretization, the search space is progressively refined in three stages in this study. In the stage of coarse search, the region between two adjacent stringers is divided into 10 sections. The thickness of each section can vary among 8 discrete values as shown in Figure 5.5. In the first refined search, the same region is further divided into 20 sections. The best solution obtained from the coarse search will be put into the initial population as seed. In the second refined search, the number of sections remains the same as the first refined search while the thickness can vary among 16 discrete values. The best solution from the first refined search is then used as seed. To show the effectiveness of this strategy, the direct first and second refined searches without seeding are also performed as references.

### 5.2.4 GA parameters used in the optimization

The population size for different stages of the progressively refined searches is summarized in Table 5.1. In the coarse and first refined searches, a population size

roughly equal to the length of the chromosomes is used as suggested by some previous researchers [98,99]. In the second refined search a relatively large population size is used for obtaining a fully converged solution.

All other GA parameters are kept the same for all the optimization runs. A tournament selection scheme with a tournament size of 3 is used. The cross over rate is 0.5. The mutation rate is controlled at two levels: for an individual the probability of being selected for mutation is 0.2, for the selected individuals the mutation rate of each allele is 0.2.

Table 5.1. Population size used in different stages of the progressively refined searching.

	chromosome length	population size
<b>coarse search</b>	15	20
<b>1<sup>st</sup> refined search</b>	30	32
<b>2<sup>nd</sup> refined search</b>	40	100

### 5.2.5 The organization of the optimization process

The object-orientated language Python is chosen to organize the optimization process. It has many advantages to perform such a task. As shown in Figure 5.6, on the one hand with the ABAQUS built-in Python interpreter, Python scripts can directly communicate with different modules of ABAQUS and perform tasks like parametric modeling, job submission and results extraction. On the other hand Python has its own evolutionary algorithm module DEAP [100], which provides comprehensive and flexible tools for setting up the GA optimizations. As a programming language with very rich scientific computing libraries, Python also facilitates the post-processing of data and parallelization of the computations, which is essential in enhancing the time efficiency of the GA optimization [57].

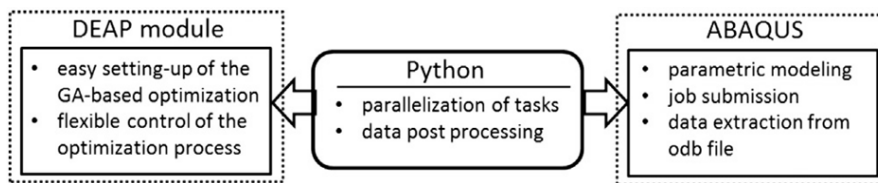


Figure 5.6. The coupling of GA with FEM simulation using Python.

The optimization process is schematically sketched in Figure 5.7. As shown in the flowchart, the first generation is randomized with stochastically produced binary bitstrings of a certain chromosome length. To maximize the initial diversity of the genotype, there are no duplicate individuals in the first generation. Then each binary string is decoded into series of thickness values representing the corresponding crenellation pattern. Based on the decoded thicknesses the INP files of a template model are edited accordingly and then submitted to the ABAQUS Standard solver. The fatigue life of each crenellation pattern is calculated based

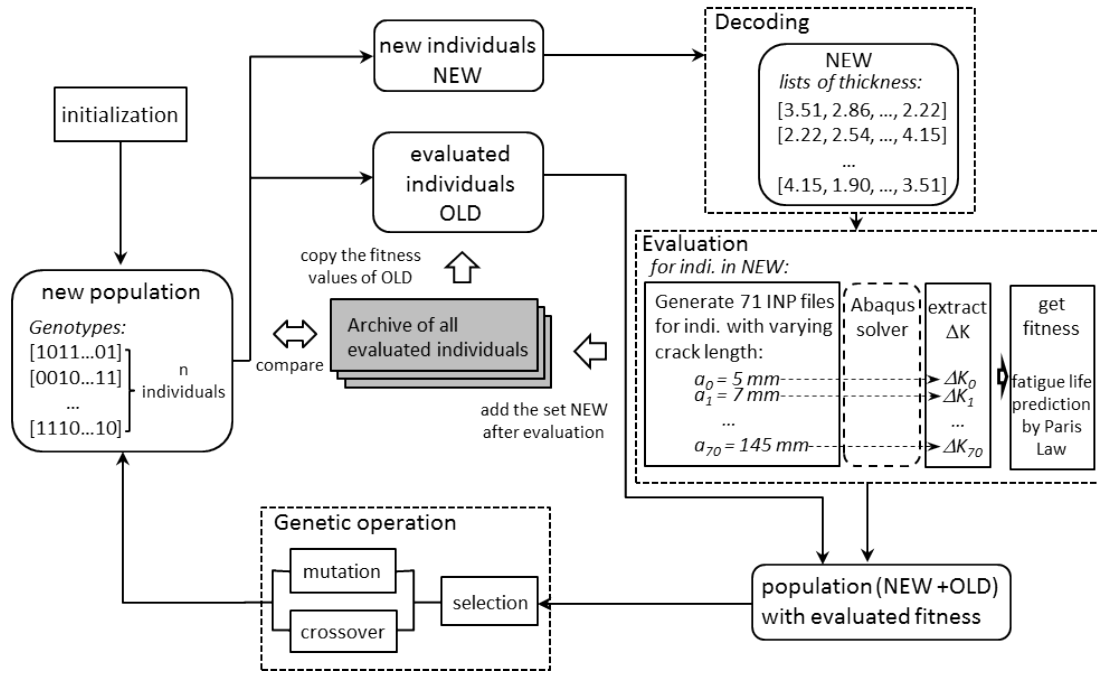


Figure 5.7. Flowchart of the GA-FEM coupled optimization process.

on the obtained  $\Delta K$  profile, which is then assigned to the individual as its fitness value. After the evaluation, the genotypes and the fitness values of the individuals are added together to an external archive, which are compared with the individuals of subsequent generations before their evaluations. Those already evaluated individuals will directly copy fitness values from the archive. This old-individual-filtering technique ensures each crenellation design is evaluated only once. After the evaluation of the whole generation is finished, the DEAP module of Python is used to perform the selection, mutation and crossover operations, which will produce the new generation. The optimization loops will be stopped when the number of generations reaches 40, or if there is no further fitness improvement of the best individual for 15 consecutive generations.

### 5.3 Optimization results

The optimized crenellation patterns indicate the successful application of the constant-weight constraint - all the solutions provided by the optimization process have exactly the same structural weight. As shown in Figure 5.8 these optimized patterns show the same trend of thickness variations: the thickness is the smallest close to the stringers, which then increases stepwise towards the symmetrical line in the center. These optimized solutions are expected to improve the fatigue life by about 10% compared to the crenellation pattern suggested by Uz et al. [7] and by 25% compared to the reference flat panel. The fraction of fatigue life improvement is also related with the final crack length, which is found to be even more pronounced at shorter crack lengths (Table 5.2). It is important to note that the fatigue life mentioned here is more exactly the fatigue crack growth life from an assumed detectable length to a maximum allowable length according

to the damage tolerance concept, which normally shows very small scattering in experiments [17]. Thus the fatigue life improvement brought by the optimized design is expected to be a significant effect in practice.

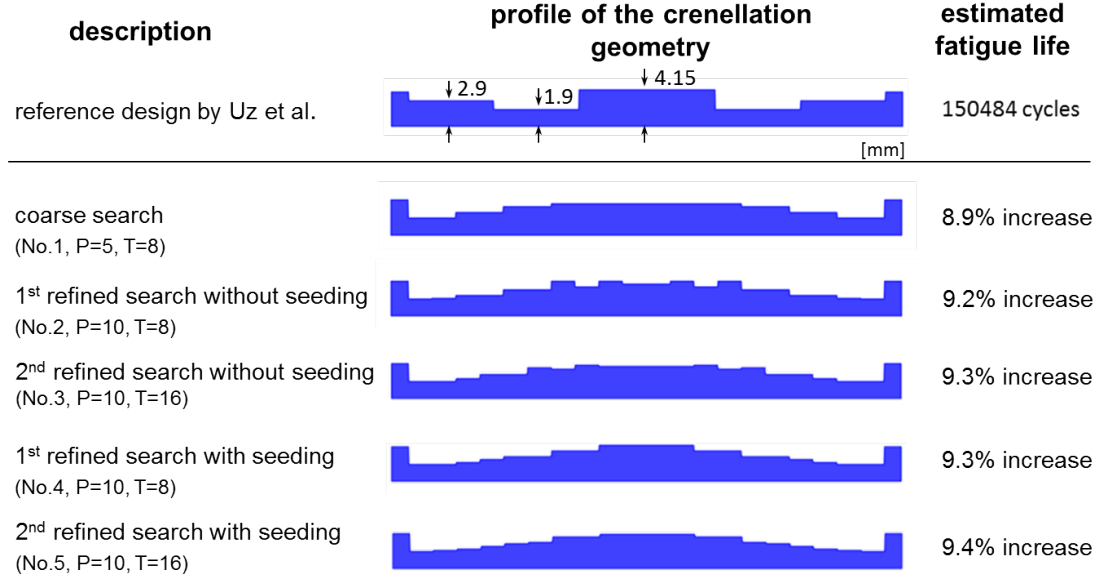


Figure 5.8. Optimized geometries of crenellation patterns (the thickness values are summarized in Table 5.3) and the estimated fatigue life increase in comparison with the initial design. P is the number of thickness sections and T denotes the number of the number of thickness levels.

Table 5.2. The fraction of fatigue life increase of the optimized design compared to the initial design.

a [mm]	compared to initial design
60	19%
80	16%
100	14%
140	12%

Comparing the solutions obtained at different stages of refined searches, it is found that the greater the refinement of the search space is, the better solution can be obtained. This is expected since the refinement of the search space provides a larger degree of freedom in searching the optimum.

At the same stage of refined searches, the seeded searches converged at better solutions than the unseeded searches. This can be understood from the dynamics of GA searching. According to Rothlauf [56], the representation of solutions by chromosomes in GA can be categorized into the uniformly scaled, where alleles at different positions of the chromosome have nearly the same contribution to the overall fitness, and the non-uniformly scaled, where the importance of alleles varies considerably. For the uniformly scaled representations the GA searching

Table 5.3. Optimized thickness in different sections of the crenellation patterns.

No.	thickness of different sections [mm]									
	1.9		2.5		3.15		3.47		3.47	
1	1.9	1.98	2.3	2.3	2.94	2.94	3.9	3.26	3.9	3.58
2	1.9	1.9	2.23	2.68	2.68	3.43	3.28	3.73	3.58	3.58
3	1.9	1.9	2.15	2.47	2.78	2.78	3.43	3.43	4.07	4.07
4	1.9	2.03	2.18	2.48	2.78	2.93	3.53	3.53	3.82	3.82

tends to solve all the alleles in parallel, whereas for the non-uniformly scaled representations so called domino convergence occurs [101, 102]. The solving and the final fixation of the alleles will occur sequentially from the high salient alleles towards low salient alleles as shown in Figure 5.9.

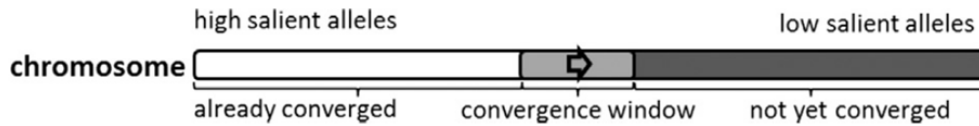


Figure 5.9. Sequential solving from high salient alleles to low salient alleles in non-uniformly scaled representations. (based on description of [101])

In our case, the representation is non-uniformly scaled. As shown in Figure 5.10 the majority of fatigue life is spent in the early stage of crack growth. For the same amplitude of thickness variation, the closer it is located with respect to the crack initiation sites - the roots of stringers, the larger influence it would have on the total fatigue life, which is the area below the curve in Figure 5.10. As a result based on the encoding scheme explained in section 5.2.2 the alleles close to the left end of the chromosome is more salient than the alleles close to the right end (Figure 5.11).

Such a non-uniformly scaled representation will result in a sequential solving of alleles generally from left to right. Such a trend can be clearly seen from the genotype evolution of the fittest individual over different generations (Figure 5.12). In the stage of the coarse search, the chromosome is relatively short. When the optimizations ended due to the convergence of the population, the sequential solving of the alleles had already gone through the whole chromosome length (Figure 5.12 a). All alleles have been fully solved. As a result the optimized crenellation pattern shows a clear trend of stepwise increase and decrease of thickness. In the first and second refined searches, not only does the chromosome become much longer, but the disparity of importance between different alleles also increases, since the flip of an allele with the lowest salience represents now smaller change in the solution space. This in turn leads to a longer time for the sequential solving to reach the lowest salient alleles.

With increasing time, the genetic diversity of the population decreases signifi-

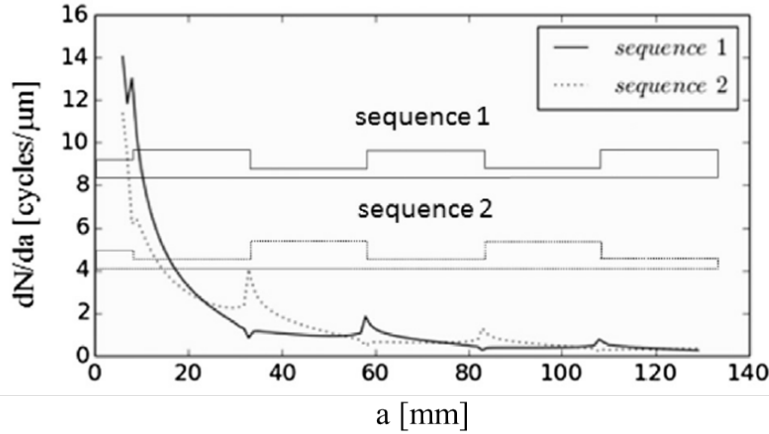


Figure 5.10. Influences of the crenellations on the number of cycles needed for every millimeter of crack extension along the crack path for two complementary cases (sequence 1 and 2) - the closer to the stringer the more salient the features are.

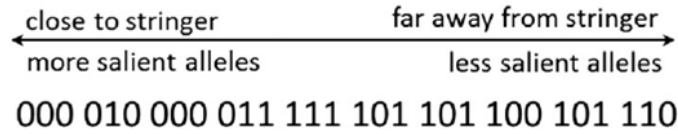


Figure 5.11. A sample chromosome from the first refined search and the variation of the salience of different alleles with their relative positions in the chromosome.

generation	genotype of fittest individual	generation	genotype of fittest individual
1-4	000000100111101	1, 2	000010000011111101101100101110
5, 6	0000010100111100	3, 4	000001011010110110101100111110
7	000011100111110	5	000001000010110110101100111110
8	000011110111110	6	00000100000101110110111100101110
9-22	000010100111111	7-9	000001000001011101111100111110
23-37	000010100110110	10-22	000001000001011101011001111110
38	000010100110111	23-30	000001000001011100110100111110

(a)

(b)

Figure 5.12. Evolution of the genotype of the fittest individual over generations (the changed alleles compared to previous generations are marked by a gray background) in (a) the coarse search and (b) the unseeded first refined search.

cantly due to the predominance of certain advantageous genotypes in the population (if no niching [103] is applied like in our case). It is quite possible that before the lowest salient alleles are fully solved through the selection pressure, they could have already been incorrectly fixed due to the loss of genetic diversity in the population, which is known as the genetic drift [56]. As shown in Figure 5.8 in both cases of unseeded refined searches, incomplete solving of the low salient alleles can be observed. It is presented as irregular variations of thickness in the center part of the crenellation pattern, since the influence of those regions on the overall fatigue life is relatively minor. In the seeded search, the solution provided by the seed is already close to the optimum solution. As a result, the fine adjustment of some single alleles directly starts particularly on those least salient alleles until they are fully solved (Figure 5.13). In this way, seeding can significantly alleviate the premature convergence due to the incomplete solving of low salient alleles in the refined searches and improve the solution quality.

generation	genotype of fittest individual
1	0000000000100100011001101011101111111111
2-4	00000000001001000110011010111011111111101
5, 8, 9	00000000001001000110011110111011111111111
10, 11	00000000001001000110011110111011111111100
12-25	00000000001001000110011110111011111011101
26	00000001001001000110011110111011111011101

Figure 5.13. Evolution of the genotype of the fittest individual over generations in the seeded second refined search.

## 5.4 Reviewing about the computational cost

Figure 5.14 compares the increase of solution quality with increasing number of evaluations up to convergence in both the coarse and refined searches. The total computational cost for the progressively refined searches is shown by connecting the curves of coarse and refined searching stages consecutively. As shown in Figure 5.14, the fast converging coarse search brings the major leap of fatigue life improvement. Further refinement of the search space only leads to limited increase of fatigue life.

Compared to the two direct refined searches without seeding, the progressively refined approach needs shorter computation time but converges to even better solutions. The fast evolution of solutions in the coarse searching stage is due to the smaller population size and shorter chromosome length, since the convergence time was found to increase with both factors [104, 105]. Further saving of computational cost comes from the stages of refined search due to the introduction of a seed. Seeding not only leads to an earlier convergence at a smaller number of generations but also reduces the number of evaluations needed for each generation when the old-individual filtering technique is applied. Figure 5.15 b plots the num-

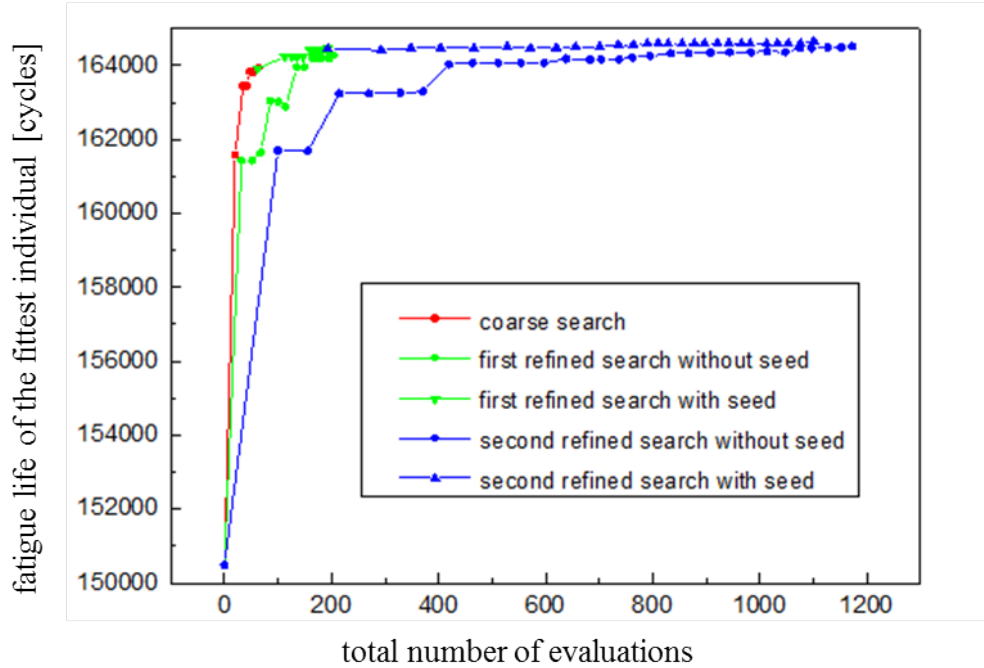


Figure 5.14. Comparison of the solution quality with and without seeding based on the coarse search.

ber of individuals evaluated per generation in both seeded and unseeded refined searches. It is found that with increasing number of generations, the number of evaluations per generation decreases due to the reappearance of old individuals. The magnitude of the decrease is determined by the state of convergence in the population. When the population has been dominated by a highly fit solution, crossover can hardly produce new solutions that have not been evaluated. The new genotypes are then mostly supplied by the mutation process. As a result, in the end the number of evaluations per generation stabilizes around 20 out of 100 due to the individual mutation rate of 0.2. Thus, the dominance of the nearly converged solutions in the populations marks the transition from the stage of global searching through the crossover to the stage of local searching through the mutation. As indicated by the arrows in Figure 5.15, the stage of local searching starts much earlier in the seeded search than in the unseeded search, which is probably due to the fast convergence of the population towards the highly fit solution provided by the seed. As a result, the number of evaluations per generation is significantly reduced in the seeded search compared with the unseeded search.

In conclusion, the coarse search with around a hundred evaluations can already provide a rather good solution close to the upper limit of improvement. However, if even higher solution quality is desired, the most cost-effective approach is to refine the search space progressively and put the previously obtained best solution in the initial population of the subsequent optimization as seed.

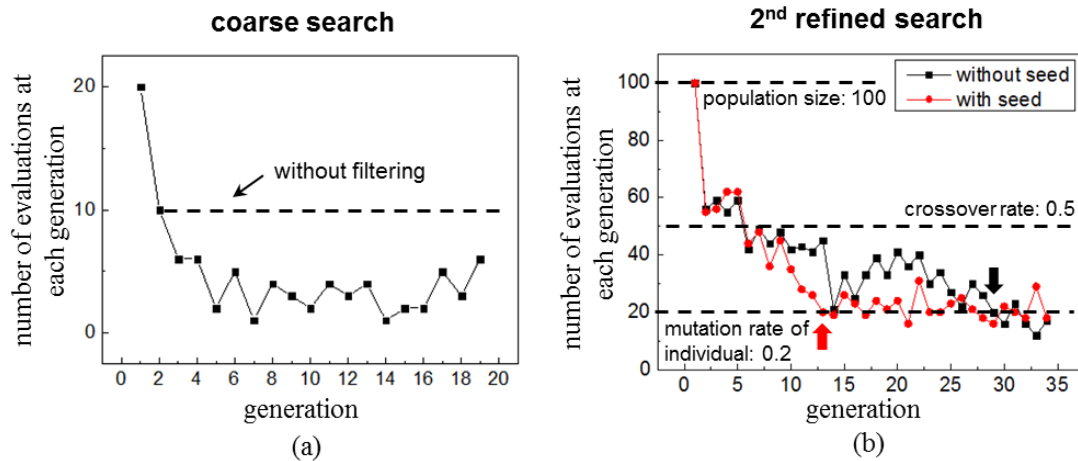


Figure 5.15. Number of evaluations per generation in the coarse search (a) and in the seeded and non-seeded second refined searches (b, arrows indicate the points when the number of evaluation per generation decreases to around 20).

## 5.5 Verification and validation of the approach

As mentioned in section 5.2.1, when handling the constant weight constraint, a compensation term was applied during the decoding process of the optimization. However, it is not known if the application of this compensation term will affect the optimized results. In order to verify this, one method is to simply release the constant weight constraint and turn the single objective optimization into a multi-objective optimization, where the algorithm maximizes the fatigue life and meanwhile minimizes the structural weight.

To perform the multi-objective optimization, two small modifications in terms of fitness assignment scheme and elitist strategy need to be made in the present optimization routine to transform the previously used canonical GA into a multi-objective variant named NSGA-II. This has been explained in the section 2.2.4 in detail. The results of the multi-objective GA optimization are a set of solutions contained in the final population known as the best-known Pareto set [64], which shows the best compromise between increasing fatigue life and decreasing structural weight.

The best-known Pareto set obtained after performing the multi-objective optimization of the crenellation pattern using NSGA-II is presented in Figure 5.16 as a series of blue dots in the objective space. Each blue point corresponds to one optimum design of crenellation pattern with the maximum fatigue life for a given weight. This can be seen by comparing with a series of randomly generated crenellation patterns (red dots in Figure 5.16). The majority of the solutions of the best-known Pareto set are found to show the same feature of stepwise increase and decrease of thickness as observed in the single objective optimizations. In addition, the optimum solution with nearly the weight as a 2.9 mm flat panel in the best-known Pareto set (the optimized design b in Figure 5.16) has almost the same geometry as the solution found in section 5.3 (see Figure 5.8, coarse search). As

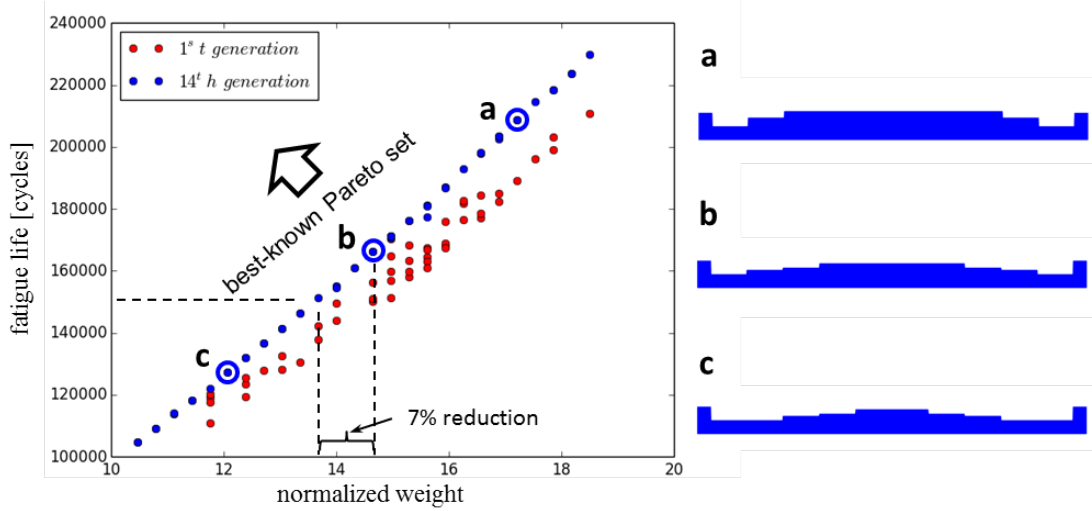


Figure 5.16. Results of the multi-objective optimization of the crenellation geometry, which maximizes the fatigue life and meanwhile minimizes the structural weight. The normalized weight is equal in value to the sum of thickness of all the five sections. Thus the flat panel with normalized weight of 1 has a thickness of 0.2 mm.

a result, the application of the compensation term in the decoding process should not influence robustness of GA in successfully finding the optimum solution.

Although the multi-objective GA needs a computational cost that is roughly 7 times of the single objective optimization in this study, much richer information is contained in the optimization results, which consists of 26 different optimum or near-optimum designs. This population of high quality solutions can help the designer in the following two aspects. Firstly, it helps to reveal the structure of good solutions. If the optimization of the crenellation design is viewed as the redistribution the "extra" material in the panel, which is located beyond the lower boundary of the thickness (1.9 mm), it can be seen that in the optimized design this part of "extra" material is always firstly allocated in the center of each bay, where the thickness of this region reach or almost reach the upper boundary. Then the rest material is distributed from center of the bay to stringers in an attenuating way. With increasing structural weight, larger and larger areas in the center of the bay reach the upper boundary of the thickness range. The two flanks of attenuating thickness also extend towards the stringer sockets accordingly. Thus, the stepwise increase and decrease of panel thickness should be an essential feature for the crenellation designs with highest fatigue lives.

Secondly, it provides quantitative information concerning the best trade-off among the conflicting design objectives. As it is shown in Figure 5.16 if the same fatigue life is aimed as in the reference design (around 150000 cycles, Figure 5.8), now a structure with the normalized weight of about 13.5 can be used, which corresponds to a 7% weight reduction compared to the original normalized weight (14.5, the weight of the optimized design b). Since the feature of crenellation will repeat thousands of times in a fuselage, totally it can save considerable materials

for the airframe structure, which in turn brings huge reduction of fuel consumption per year (the reader can refer to the report of Lufthansa Group in [106]). Thus, this information is important for the decision maker to work out the most economic-efficient design taking into account both the costs from maintenance and fuel consumption.

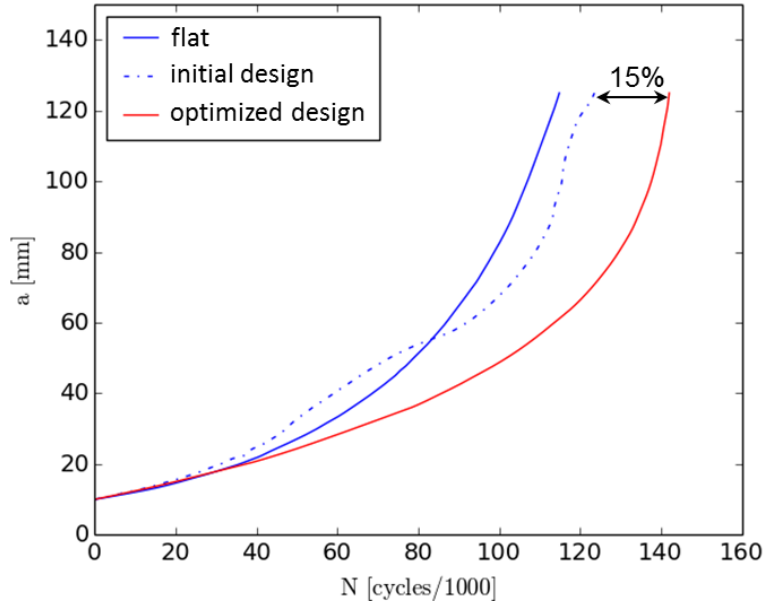


Figure 5.17. The experimentally measured fatigue life of crenellated specimens with the initial design and the optimized design in comparison with the flat specimen.

Table 5.4. Comparison of predicted fatigue life with the measured fatigue life for both the initial design and the optimized design.

	initial design	optimized design
<b>predicted fatigue life</b>	124199 cycles	141966 cycles
<b>measured fatigue life</b>	123509 cycles	141984 cycles

After the verification of the previous optimization results using the approach of multi-objective optimization, the effectiveness of the optimized design in the further extension of fatigue life is also experimentally validated. A panel with the optimized crenellation geometry was manufactured and tested under the same loading condition as the flat specimen and the crenellated specimen with the initial design. As show in Figure 5.17, although the three panels have the same weight, the optimized design shows significantly longer fatigue life compared to the other two specimens. In addition, the experimentally observed fatigue life improvement of the optimized design with respect to the initial design (15%) is nearly the same as what has been expected from simulation (Table 5.4). As a result, the proposed

FEM-GA coupled approach has provided an effective and reliable optimization of crenellation geometry.

## 5.6 Optimizing the combination of crenellation with laser heating techniques

The FEM-GA coupled optimization approach demonstrated in previous sections can in principle approach the upper limit of fatigue life improvement of the crenellation concept under the prescribed constraints in section 5.2.1. This limit of fatigue life improvement in crenellated airframe structure can be further extended by additionally introducing other fatigue crack retardation techniques, which also do not add up to the structure weight.

Laser heating [51, 52, 107] is such a promising technique to be applied together with crenellation. In this technique, the surfaces of thin metal plates are irradiated by a defocused laser along a linear path with a spot size around 5 mm. The material is locally heated up to a temperature much lower than the melting temperature. The transient heat input causes significant expansion of material directly irradiated by the laser beam compared to ambient material, which causes the local material to be plastically deformed. After cooling down to the room temperature, a tensile residual stress develops along the heating line, which is balanced by the compressive residual stress in the surrounding region. According to Schnubel [107], the widely spreading compressive residual stress field can effectively retard the fatigue crack growth over a large distance and thus lead to a significant fatigue life extension.

In this section two such heating lines are to be applied in each bay between two stringers, the arrangement of which should be also symmetric to the center of the bay as the crenellation pattern does. The aim of this part is to find out the best combination of the two methods in order to maximize the fatigue crack retardation. The configuration is optimized using GA in terms of crenellation geometry and the position of laser heating lines. By encoding both the information in one chromosome one can exploit the interaction between two aspects and thus find the optimum combination.

### 5.6.1 Including residual stress field of laser heating in the FEM model

To attain the aforementioned aim, the first step is to introduce the residual stress field from the laser heating process in the FEM model. Then it should be validated that the fatigue crack retardation effect can be well predicted by the FEM model. The residual stress field to be introduced is based on the residual stress measurement of laser heated specimens using synchrotron X-ray diffraction from Groth et al. [108, 109]. In the experiments of Groth, two lines of laser heating were performed on the surfaces of 2 mm thick AA2024 panels with a spacing of 80 mm symmetrically to the center line (Figure 5.18 a). The measured residual stress profile along a horizontal path through the center of the specimen is plotted in Figure 5.18 b. The fatigue crack growth behavior of both laser heated and reference specimens, which are tested under the same uniaxial loading condition

( $F_{\max} = 42.5$  kN,  $F_{\min} = 4.25$  kN), are compared in Figure 5.18 c. The fatigue test results will be used to validate the FEM model with the residual stress field from laser heating.

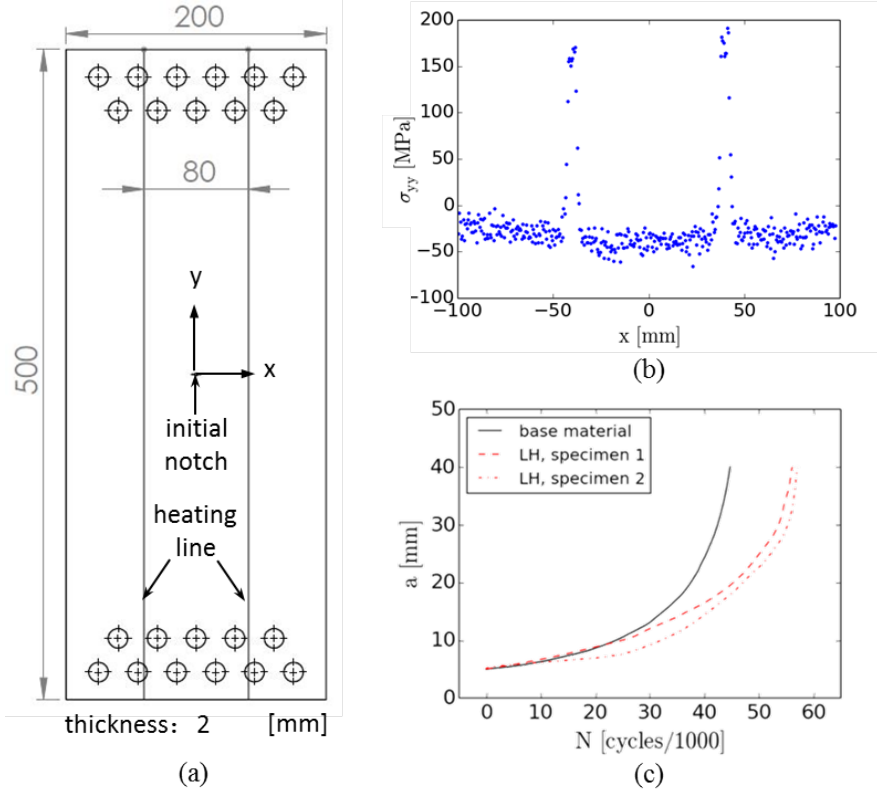


Figure 5.18. Experimental data of laser heated AA2024 panels [108,109]. (a) Specimen geometry. (b) Residual stress distribution in specimen with 2 laser heating lines measured by synchrotron X-ray diffraction. (c) Comparison of fatigue performance between the base material and the laser heated specimens.

In analogy to the welding process, the source of the residual stress field developed during the laser heating process is the net plastic strain left in the heated zone after a cycle of thermal expansion and the subsequent shrinkage, which is also referred to as the inherent strain [110]. As a result, once the distribution of the inherent strain in the laser heated zone is obtained, the evolved residual stress field can be calculated in a simple elastic analysis by mapping the distribution of inherent strain in the object. In this study, the introduction of residual stress field of the laser heating, which can be applied at an arbitrary position of the FEM model, is based on the idea of mapping the inherent strain field at the prescribed locations.

The model for the distribution of inherent strain in the laser heated zone can be obtained through the analyses of the temperature field. During the process of laser heating, the locally heated material can be considered as to expand in a fully constrained state. According to Ueda [110] after the thermal cycle  $T_{\text{room}} \rightarrow T_{\text{max}} \rightarrow T_{\text{room}}$  (assuming  $T_{\text{room}} = 0$ ) the inherent strain  $\varepsilon^*$  generated at such a

condition is formulated by:

$$\varepsilon^* = \begin{cases} 0, & \text{if } T_{\max} \leq T_y, \\ -\alpha(T_{\max} - T_y), & \text{if } T_y \leq T_{\max} \leq 2T_y, \\ -\alpha T_y, & \text{if } T_{\max} \geq 2T_y. \end{cases} \quad (5.3)$$

where  $T_y$  is the yield temperature, at which plastic deformation of the material start to occur due to thermal expansion,  $\alpha$  is the thermal expansion coefficient.

In the vicinity of the region directly irradiated by the defocused laser beam, due to the generally homogeneous temperature distribution a constant inherent strain  $\varepsilon_{\max}^*$  can be assumed. Then with further increasing distance from the heating line, the inherent strain drops significantly due to the decrease of the  $T_{\max}$ . According to Ueda, in analogy to the welding of thin plate,  $T_{\max}$  at a distance of  $r$  from the heating line can be expressed by: [110]

$$T_{\max}(r) = 0.242 \frac{Q}{c\rho h} \frac{1}{r} \quad (5.4)$$

where  $Q$  is the heat input,  $c$  is the specific heat,  $\rho$  is the density and  $h$  is the thickness of the plate. By putting equation 5.4 into equation 5.3 for the case  $T_y \leq T_{\max} \leq 2T_y$ , one can get the attenuation of inherent strain with increasing  $r$  in the following form:

$$\varepsilon^*(r) = -(A/r - B) \quad (5.5)$$

where  $A$  is equal to  $0.242 \frac{\alpha Q}{c\rho h}$ ,  $B$  is equal to  $\alpha T_y$ . Thus, the distribution of the inherent strain at the heating line has the profile as shown in Figure 5.19. When  $r$  is smaller than  $d_1$ ,  $\varepsilon^*$  reaches a maximum value  $\varepsilon_{\max}^*$ . When  $r$  is between  $d_1$  and  $d_2$ ,  $\varepsilon^*$  decreases inversely with increasing  $r$ . When  $r$  is larger than  $d_2$ ,  $\varepsilon^*$  is constantly 0 due to that  $T_{\max}$  drops below  $T_y$  according to equation 5.3. Here, the variation of inherent strain in the thickness direction is ignored for simplicity considering the 2-dimensional nature of the problem involving through-thickness crack growth. By putting the two solutions ( $r = d_1, \varepsilon^* = \varepsilon_{\max}^*$ ) and ( $r = d_2, \varepsilon^* = 0$ ) shown in Figure 5.19 into equation 5.5, one can obtain the values of  $A$  and  $B$  in terms of  $\varepsilon_{\max}^*$ ,  $d_1$  and  $d_2$ . The whole profile of inherent strain distribution can be formulated by the piecewise function:

$$\varepsilon^* = \begin{cases} \varepsilon_{\max}^* & \text{if } r \leq d_1, \\ \frac{\varepsilon_{\max}^* d_2 d_1}{d_2 - d_1} \frac{1}{r} - \frac{\varepsilon_{\max}^* d_1}{d_2 - d_1} & \text{if } d_1 \leq r \leq d_2, \\ 0 & \text{if } r \geq d_2. \end{cases} \quad (5.6)$$

The real distribution of inherent strain inside the specimen is approximated by fitting the three unknown parameters  $\varepsilon_{\max}^*$ ,  $d_1$  and  $\Delta d$  ( $d_2 = d_1 + \Delta d$ ) in equation 5.6 using the experimentally measured residual stress field. GA is used here as a parameter fitting technique to obtain the best set of  $\varepsilon_{\max}^*$ ,  $d_1$  and  $\Delta d$  values, which can minimize the deviation between the numerically calculated residual stress field and experimentally measured one. Based on the information in Fig-

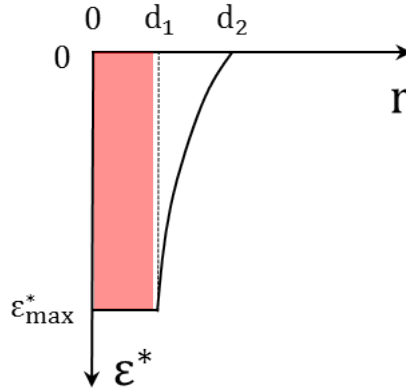


Figure 5.19. Distribution of intrinsic strain  $\varepsilon^*$  transverse to the heating line. The red shaded area presents the region irradiated by the laser beam.

ure 5.18 b, the search ranges for the three parameters are fixed as follows:  $\varepsilon_{\max}^*$ : (-0.0034, -0.0026),  $d_1$ : (1, 4) [mm] and  $\Delta d$ : (0.5, 3) [mm]. Each parameter is then represented by a 3-digit binary code, which is expected to provide sufficient solution accuracy considering the small search range. Thus each guess of the possible inherent strain distribution is represented by a chromosome with totally 9 digits. After the decoding of a chromosome, the corresponding inherent strain distribution is introduced into the FEM model (Figure 5.20 a) by mapping a pseudo temperature field at the sites of the heating lines using the keyword \*TEMPERATURE in the ABAQUS input file. The pseudo temperature field  $T_{\text{pseudo}}$  is related with the mapped inherent strain field by the following equation:

$$T_{\text{pseudo}} = \varepsilon^* / \alpha \quad (5.7)$$

Then, the quality of the guessed set of parameters is evaluated by comparing the evolved residual stress profiles with the experimentally measured one. The fitness of a guess is the inverse of the standard deviation between the predicted and measured values. In the parameter fitting process, a small population of 15 was used, which led to a fast convergence towards the follow set of values:  $\varepsilon_{\max}^*$ : -0.00314,  $d_1$ : 2 mm and  $\Delta d$ : 1.5 mm. Figure 5.20 b compares the numerically calculated residual stress profile using the fitted values with the experimentally measured one, which shows a rather good agreement.

In the following step the FEM model with the fitted inherent strain field is validated in terms of its capacity in predicting the fatigue life improvement brought by laser heating. To this end, a center crack with incrementally increased size from  $a = 5$  mm to  $a = 50$  mm is introduced in the model. The profiles of stress intensity factors under maximum and minimum loads ( $K_{\max}$  and  $K_{\min}$ ) are calculated respectively. It should be noted that the R-ratio ( $K_{\min}/K_{\max}$ ) in such a case is not a constant. Considering the R-ratio effect due to the crack closure (section 2.1.2 and section 2.1.3), the effective ranges of stress intensity factor  $\Delta K_{\text{eff}}$  are calculated using the empirical equation from Elber [34]:

$$\Delta K_{\text{eff}} = (0.5 + 0.4R)\Delta K \quad (5.8)$$

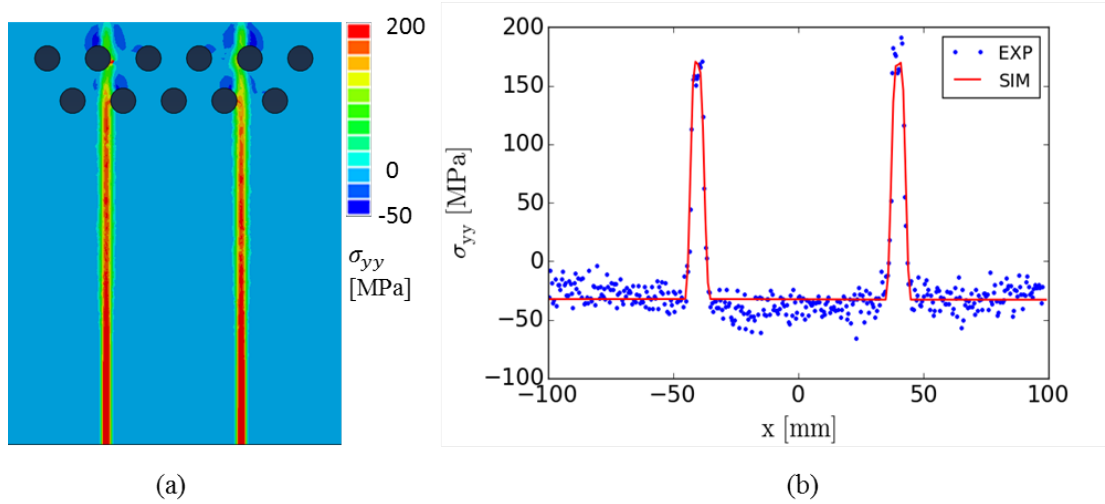


Figure 5.20. (a) FEM model of the specimen with 2 laser heating lines. (b) The numerically calculated residual stress profile based on the fitted parameters (SIM) in comparison with the experimental measured one (EXP) [108, 109] through the center of the specimen.

The crack growth rate can be correlated with  $\Delta K_{\text{eff}}$  using Paris Law:  $da/dN = C \cdot \Delta K_{\text{eff}}^m$ . It should be noted that both  $K_{\text{max}}$  and  $K_{\text{min}}$  are actually the linear superimposition of two parts: the part due to the applied load  $K_{\text{app}}$  and the part due to the residual stress field  $K_{\text{res}}$ . Considering the large compressive residual stress introduced by laser heating and the small magnitude of the minimum load, it is quite possible that at the minimum of load,  $K_{\text{app}}$  even cannot balance out  $K_{\text{res}}$ , which results in negative crack opening displacement. However, this is physically incorrect. In reality it means the close of the crack, where the stress intensity factor is equal to zero. As a result, it is important to detect the negative crack opening displacement in simulations and to set the  $K_{\text{min}}$  of such cases to zero.

Based on the aforementioned method, the  $\Delta K_{\text{eff}}$  values for both reference and laser heated specimens are calculated, which are then plotted against the corresponding  $da/dN$  values measured from experiments by Groth et al. [108, 109] (Figure 5.21). It can be seen in the  $da/dN$ - $\Delta K$  plot that, after introducing the fitted inherent strain fields in the laser heated specimens, the initial gap between the data points of the reference and the laser heated specimens before correction disappears. All the data points fall into a single straight line as characterized by Paris law. By fitting the Paris constants as explained in section 5.1 and integrating the inverse of the calculated  $da/dN$  over the crack path using the Paris Law, one can get the predicted fatigue life for both reference and laser heated specimens. As shown in Figure 5.22, the fatigue life improvement predicted by using the FEM model with the mapped inherent strain field is nearly the same as it is observed in experiments, which validates the introduced residual stress field.

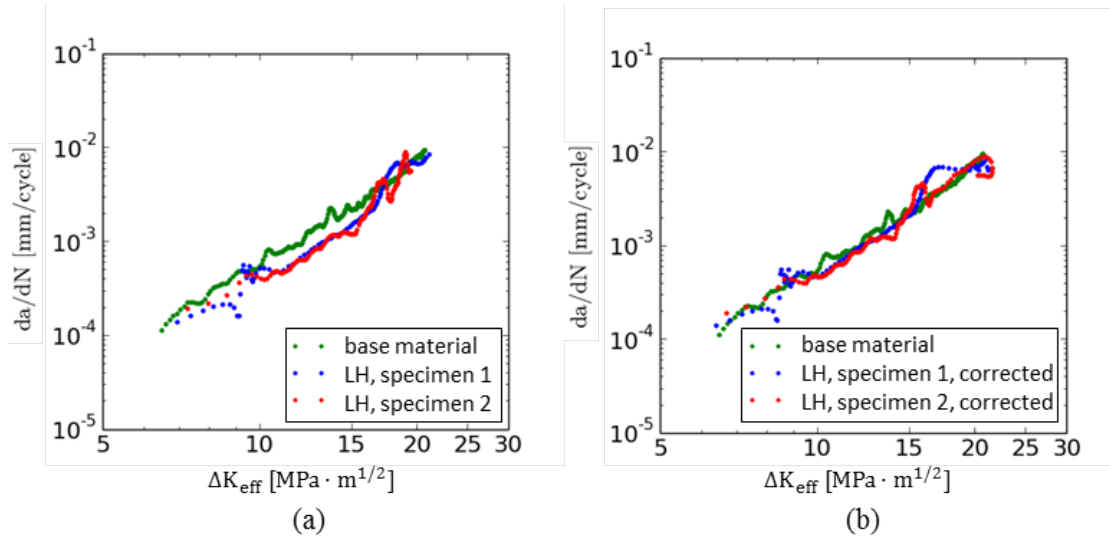


Figure 5.21.  $da/dN$ - $\Delta K_{eff}$  plots of a reference specimen (base material) and two laser heated specimens (LH). (a) The residual stress field of laser heating is not taken into account in the FEM models. (b) The FEM models are corrected with the residual stress field by mapping the fitted inherent strains into the corresponding locations of heating lines.

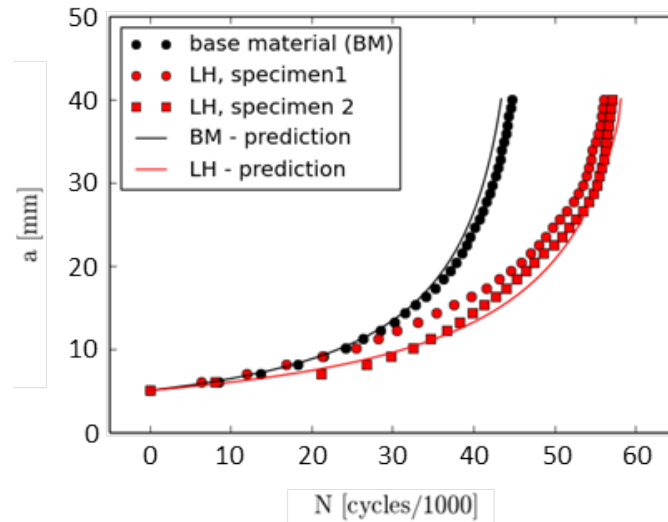


Figure 5.22. Comparison between the experimentally observed fatigue life improvement and the predicted one based on FEM simulations when two heating lines are introduced in the specimen.

### 5.6.2 Implementation of GA in the present optimization problem

In the previous section the numerical approach for predicting the fatigue crack retardation effects of laser heating has been validated, which is based on the mapping of the inherent strain distribution into the FEM model. In the following optimization process, the same method is applied to the FEM models to be coupled with GA, where the inherent strain distribution of heating lines is mapped at different locations of the models according to the design that is evolved. Here, it is assumed that a similar distribution of inherent strain can be introduced in a AA2139 panel of 2 mm thickness by the same laser heating process as the case of AA2024 panels investigated by Groth et al [108, 109].

In order to find out the best combination of the laser heating and crenellation techniques, the position of the heating line and crenellation geometry are encoded in a single chromosome. As shown in Figure 5.23 the three alleles at the left end of the chromosome represent the position of the two symmetrical heating lines with respect to the center of the bay. As marked by red arrows in Figure 5.23, they totally have 8 different variations of positions. The rest part of the chromosome, which encodes the crenellation geometry, uses the same representation scheme as in the stage of the coarse search (section 5.2.2).

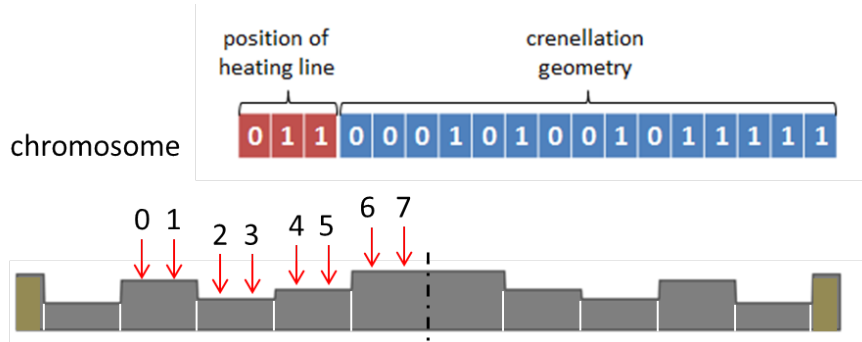


Figure 5.23. Encoding the position of the heating line and the crenellation geometry in one chromosome.

When decoding a chromosome into its corresponding FEM model, it is important to take into account the influence of the thicknesses of laser heated regions on the inherent strain to be included. This is due to the fact that, given a constant heat input, the larger the thickness of the heated region is, the smaller the temperature increase will be expected considering the larger volume of heated material. This then leads to a smaller expansion of the material and also smaller plastic deformation after the thermal cycle. Therefore, a smaller inherent strain will be introduced by the same process in thick regions compared to in thin regions.

In a first order of approximation, the inherent strain to be included in the FEM model is assumed to be inversely proportional to the local thickness, that is:

$$\varepsilon^*(t, r) = \varepsilon_{t_0}^*(r) \frac{2}{t} \quad (5.9)$$

where,  $\varepsilon^*(t, r)$  is the inherent strain at a distance of  $r$  from the heating line,  $t$  is the thickness in mm and  $\varepsilon_{t_0}^*(r)$  is the previously fitted profile of inherent strain using a specimen with a thickness of 2 mm.

This assumption implies that the integration of inherent strain over the cross section of the laser heated zone is a constant irrespective of the local thickness, given that the width of the laser heated zone is a constant for the same laser heating process. This is in accordance with the theoretical work of Ueda et al. [110] on the residual stress in butt-welded thin plates. According to their work, the integration of the tensile stress over the transverse section of the welding line, which is known as the tendon force  $F_T$ , is invariant with thickness at a constant heat input  $Q_{\text{net}}$ :

$$F_T = 0.335(E\alpha/c\rho)Q_{\text{net}} \quad (5.10)$$

where,  $E$  is the elastic modulus,  $\alpha$  is the thermal expansion coefficient,  $c$  is the heat capacity and  $\rho$  is the density.

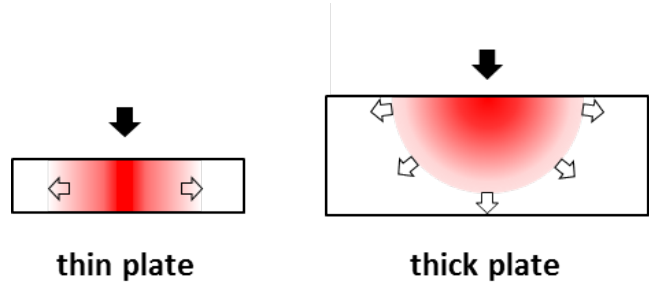


Figure 5.24. Different characteristics of heat flow when the laser heating is performed on a thin plate and on a thick plate.

However, laser heating is significantly different from welding processes in that the heat source of laser heating is located on the irradiated surface instead of penetrating through the thickness of the panel as the welding case. When the heated panel is relatively thin, the temperature difference in the thickness direction can be ignored, whereas at larger thicknesses there can be a pronounced through-thickness temperature gradient. This has been reported in the temperature field simulation of laser heating performed on a 5 mm-thick aluminum panel by Schnubel [107]. This leads to the fact that, with increasing thickness, the original planar heat flow in thin panels becomes radial with respect to the heating line as shown in Figure 5.24. The increased dimensionality of heat flow can accelerate the heat dissipation in the material and thus further lower the maximum temperature in the laser heated region. It implies that the damping of inherent strain with increasing thickness should be faster than in the previous scenario.

Being compatible with the expression used in the first scenario we can use a common form to formulate the assumed damping of inherent strain with increasing thickness:

$$\varepsilon^*(t) = \varepsilon_{t_0}^* \left(\frac{2}{t}\right)^M \quad (5.11)$$

where,  $M$  is defined as the damping coefficient, and  $M$  is equal to 1 for the first scenario.

In the second scenario with a consideration of the change of the heat flow direction, a damping coefficient of 2 is used, which assumes a linear increase of heat dissipation with increasing thickness. This can be seen as the lower bound, where the inherent strain shows the fastest damping with increasing thickness.

In the third scenario, instead of applying the same laser heating process, the processing parameters are assumed to be optimized for each respective thickness, which can significantly mitigate the damping effects and thus reduce the damping coefficient. This is found to be indeed the case if we compare the measured residual stress data from Groth et al. [108] with that from Schnubel [107]. In the two cases, the laser heating process was optimized for specimens with a thickness of 2 mm ( $t_2$ ) and of 5mm ( $t_5$ ) respectively. The maximum tensile residual stress measured at the heating lines in those two cases are 180 MPa ( $\sigma_{\max,2}$ ) and 125 MPa ( $\sigma_{\max,5}$ ) respectively. If the magnitude of inherent strain developed along the heating lines is assumed to be proportional to the measured maximum tensile residual stress, based on equation 5.11  $\sigma_{\max,5}/\sigma_{\max,2}$  can be correlated with  $t_2/t_5$  by the following equation:

$$\frac{\sigma_{\max,5}}{\sigma_{\max,2}} = \frac{\varepsilon_5^*}{\varepsilon_2^*} = \left(\frac{t_2}{t_5}\right)^M \quad (5.12)$$

thus the damping coefficient for this scenario should be:

$$M = \log_{t_2/t_5} \frac{\sigma_{\max,5}}{\sigma_{\max,2}} = \log_2 \frac{125}{180} \approx 0.4$$

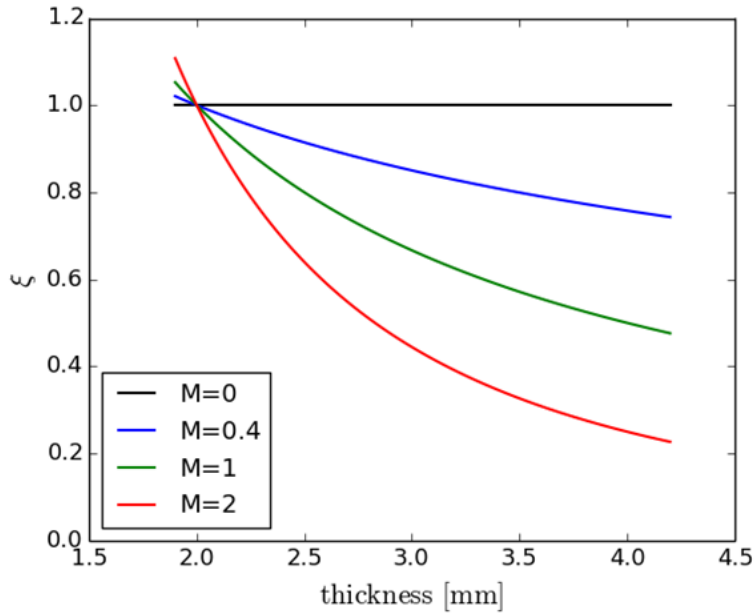


Figure 5.25. The attenuation of inherent strain in the laser heated zone with increasing thickness under different damping coefficients  $M$ . ( $\xi$  is the attenuation factor as defined by the equation:  $\xi = \frac{\varepsilon^*(t)}{\varepsilon_{t0}^*}$ )

In summary, the three aforementioned cases with  $M=0.4$ , 1 and 2 in equation 5.11 respectively represent 3 possible scenarios, where the increase of thickness has small, medium and large damping effects on the inherent strain to be mapped into FEM model as shown in Figure 5.25. In a following step, GA-based optimizations are performed under those three scenarios respectively and also under a reference case, where the damping effect is not taken into account ( $M=0$ ). The optimization results will be presented in the next section.

### 5.6.3 Results of the optimization

The optimization results under the previously described four scenarios are shown in Figure 5.26. The evolved crenellation designs show the same characteristic of a stepwise increase and decrease of thickness as observed in section 5.3. The different damping coefficients assumed in those scenarios have two impacts on the evolved optimized designs. Firstly, it influences the optimum positions of the heating lines. Secondly, it leads to small modifications of the optimized crenellation geometry. As shown in Figure 5.26, for the three cases of  $M = 0, 0.4$  and 1 both heating lines are placed at the center of the bay, whereas for the case of  $M = 2$  the heating lines are placed more close to the stringers (at the border between section II and III). The evolved crenellation designs can also be classified into the same two groups. For the cases of  $M = 0, 0.4$  and 1, the optimized crenellation designs are similar with each other. The major difference among them is that for the two cases  $M = 0$  and 0.4 the thickness of section V is at the upper boundary of the thickness range (4.15 mm), whereas for the case of  $M = 1$  it is significantly reduced. For the case of  $M = 2$  the crenellation has a more distinct appearance. It is characterized by a broad region from the stringers to the positions of heating lines, where the thickness stays at the lower boundary (1.9 mm).

Table 5.5. Optimized thickness in different sections of the crenellation patterns and the optimized position of laser heating lines (HL). Positions 0-7 are defined in Figure 5.23.

	thickness of different sections [mm]					position of HL
no HL	1.9	2.5	3.15	3.47	3.47	-
<b>M = 0</b>	1.94	2.27	2.91	3.23	4.15	7
<b>M = 0.4</b>	1.9	2.19	3.15	3.15	4.11	7
<b>M = 1</b>	1.9	2.59	2.91	3.55	3.55	7
<b>M = 2</b>	1.9	1.9	3.03	3.67	4	1

The evolved designs can be understood in terms of the overlapping of fatigue crack retardation regions and the maximization of the tendon force at the heating lines. According to section 5.5 the retardation region of the crenellation with the optimized geometry is from the root of the stringer, where the fatigue crack initiates, to the center of the bay, where the thickness is at the maximum. For

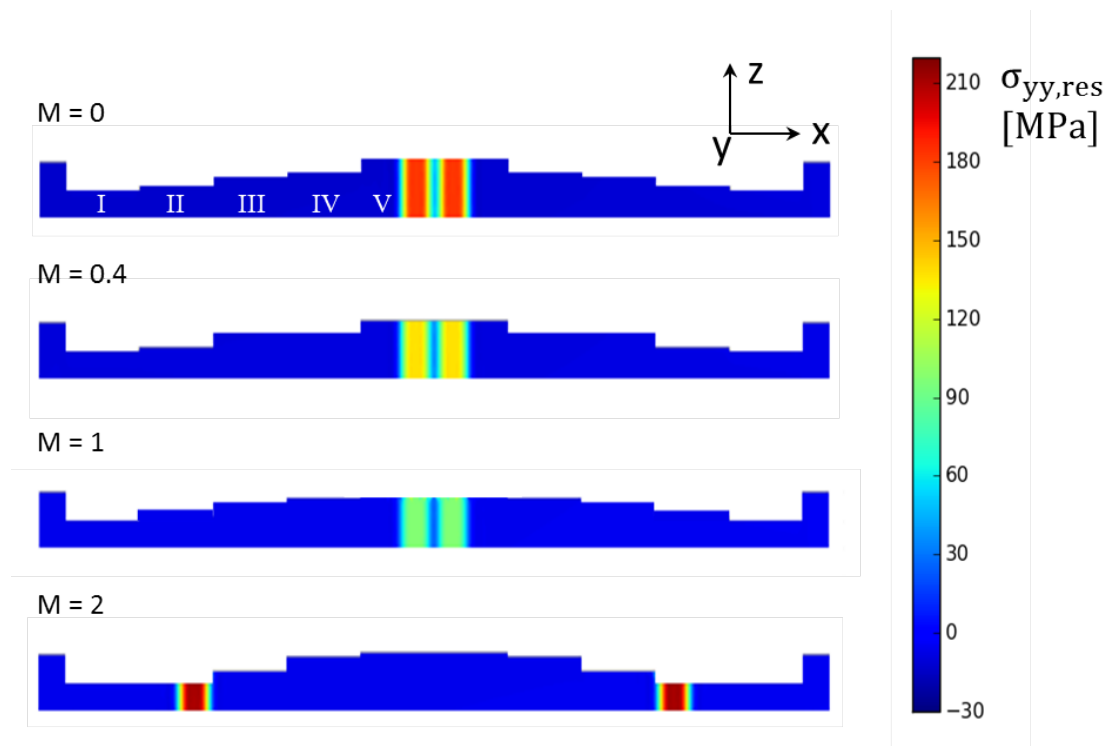


Figure 5.26. The optimized crenellation geometries together with the optimized positions of laser heating lines in the four scenarios with different damping coefficients  $M$ . The heating lines are indicated by the superimposed color maps of residual stress distribution over the cross sections, which are extracted from the corresponding FEM models.

heating lines, it starts from the crack initiation site until the heating line is severed by the crack according to Schnubel [107]. Therefore, by putting the heating lines at the center of the bay as in the cases of  $M = 0, 0.4$  and  $1$ , the retardation regions of crenellation and the two heating lines can have the largest overlap. This overlap is expected to bring the highest fatigue life improvement. According to equation 5.1, the number of cycles  $N$  for the extension of fatigue crack over one unit length is proportional to  $1/C\Delta K^m$ . Since the first and second derivatives of  $1/C\Delta K^m$  are negative and positive respectively, with continuously decreasing  $\Delta K$ ,  $N$  will increase at an accelerating rate. As a result, the accumulative reduction of  $\Delta K$ , when the retardation regions are overlapped, will lead to a larger fatigue life improvement than the case when they are more spatially separate. If the influence of the change in tendon force is not considered, the fatigue life improvement is thus expected to be the smallest when the heating line is placed at position 0 and to be the largest when it is placed at position 7 for the same crenellation geometry.

Besides the overlap of retardation regions, another factor influencing the evolved design is the tendon force. Since the widely spreading compressive stresses that result in the retardation effects of laser heating must be balanced by the tendon force at the heating lines, the higher the tendon force is the more pronounced the retardation effect is expected. If the inherent strain distribution in the laser heated zone is simplified as a constant value  $\bar{\varepsilon}^*$ , the relation between the tendon force  $F_T$  and the local thickness  $t$  of the section, where the heating line is applied, can be formulated by the following equation:

$$F_T = abtE\bar{\varepsilon}^*(t) \quad (5.13)$$

where  $a$  is a constant,  $b$  is the width of the heated region,  $E$  is the elastic modulus. By replacing  $\bar{\varepsilon}^*(t)$  with  $\bar{\varepsilon}_{t_0}^* \left(\frac{2}{t}\right)^M$  according to equation 5.11 ( $\bar{\varepsilon}_{t_0}^*$  is the averaged inherent strain in the laser heated panel with a thickness of 2 mm), equation 5.13 turns into:

$$F_T = abE\bar{\varepsilon}_{t_0}^* \frac{2^M}{t^{M-1}} \quad (5.14)$$

It can be seen from the above equation that for the cases  $M = 0$  and  $0.4$  the higher the thickness is the larger the tendon force becomes. As a result, in the optimized designs of both cases the thickness of the laser heated region (the center of the bay) is at the upper boundary of the thickness range in order to maximize the tendon force. For the case  $M = 1$ , the tendon force becomes invariant with changing thickness (the term  $t^{M-1}$  in equation 5.14 is constantly equal to 1). Then, the optimized crenellation geometry becomes more like the design obtained in section 5.3 (Table 5.5) with much reduced thickness of the thickest region, which is supposed to maximize the fatigue crack retardation purely from the geometric point of view. In the last case of  $M = 2$ , the tendon force decreases with increasing thickness. Thus, as shown in Figure 5.26 the heating lines are placed towards the stringer side, where the thicknesses are smallest. However, the heating lines should also be arranged such that the overlap of retardation regions is maximized. As a result, the optimized crenellation shows a much broader region with the thickness of 1.9 mm compared to other cases, which enables the heating lines to be placed

as close to the center of the bay as possible.

Therefore, the results show clear evidence that the optimization applied has successfully dealt with the co-adaption of the two fatigue retardation techniques, which maximizes their collaborative interaction and meanwhile minimizes the disruptive interaction. It should be noted that the interaction between the two techniques is complicated by the situation that the phenotypic expression of the gene governing the heating lines is dependent on the values of the genes controlling the crenellation geometry due to the thickness dependence of inherent strains. Such inter-genes interaction is also called epistasis by geneticists [111, 112]. For problems with very high epistasis, where many genes are strongly linked with other genes, the efficiency of GA can be reduced, since the building blocks can be potentially of high orders and thus are more vulnerable to the destruction by genetic operators. However, for problems with medium epistasis, according to Beasley et al. [113], GA is quite robust and efficient. Davidor [114] also considers that in a wide spectrum of cases up to very high epistasis the efficiency of GA outperforms that of conventional greedy algorithms like hill-climbing. In our case, the efficiency of GA seems not be much affected by the increasing epistasis, since no significant change of computational cost has been observed when the interaction between crenellation and heating lines gradually increases from  $M = 0$  to  $M = 2$ . Therefore, the unique holistic approach of the GA-FEM coupled optimization also has the advantage in successfully and efficiently exploiting the interactions between the different design variables.

The fatigue life extension resulting from the co-adaption of different fatigue crack retardation techniques during the optimization is shown in Figure 5.27. The percentage of fatigue life improvement is found to be significantly larger than the best cases, where only a single fatigue crack retardation technique (either crenellation or laser heating) is applied. Due to the increased damping of inherent strain from  $M = 0$  to  $M = 2$ , the fatigue life improvement for this hybridized approach decreases significantly. However, including the case with strongest damping ( $M = 2$ ), the overall fatigue life improvement achieved by the hybridized application of the two techniques is always larger than the sum of the fatigue life improvements by the two techniques respectively. The additional fatigue life gain is due to the collaborative interaction maximized by the optimization, which shows stiff increase with decreasing damping coefficient. As it can be seen in Figure 5.27, this additionally fatigue life gain becomes especially pronounced when  $M \leq 0.4$ . As a result much larger fatigue life improvement can be achieved by the hybridized application of crenellation and laser heating techniques, when the laser heating process is optimized for the large thickness at the center of the bay.

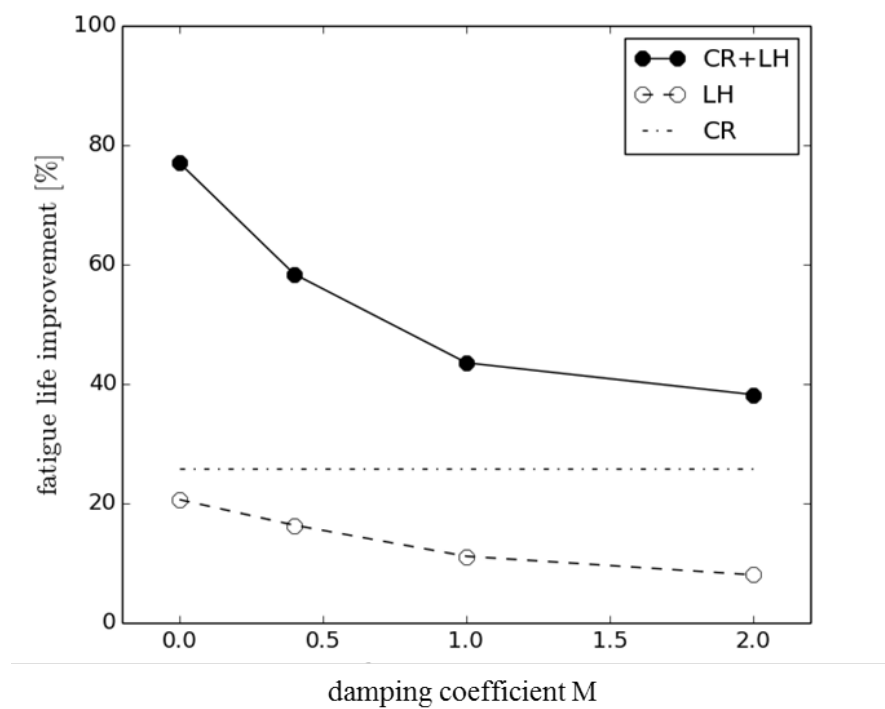


Figure 5.27. The fatigue life improvement achieved by the optimized combinations of the crenellation (CR) and laser heating (LH) techniques under various damping coefficients in comparison with the maximum fatigue life improvements that can be achieved by each individual technique.

## 5.7 Summary and suggestions for the FEM-GA coupled optimizations

The key findings of this chapter can be summarized as follows:

1. A GA-FEM coupled approach has been successfully applied in the optimization of the crenellation patterns in laser-beam-welded fuselage panels.
2. The constant-weight constraint on the evolved designs is applied by introducing a specially defined correction term in the decoding step.
3. The optimized designs show a monotonous and nonlinear increase in the skin thickness from the root of stringers towards the center of the bay, where the thickness reaches a maximum. Those designs are expected to have about 10% fatigue life improvement compared to the initial design that was developed based on experience.
4. In order to reduce the computational cost for the optimization process, a progressively refined searching approach combined with an old-individual-filtering technique has been used. This approach requires smaller computational cost and yet provides improved solution quality compared to the direct searching with the same degree of the search space refinement.
5. The method of applying the constant weight constraint is verified by performing a multi-objective optimization alternatively, in which the constraint of constant weight is released. The effectiveness of the optimized design in the fatigue life improvement is also validated through experiments.
6. A tentative study has been performed to optimize the hybridized application of crenellation and laser heating techniques through the GA-FEM coupled optimization. A much more significant fatigue life improvement compared to the sole application of each individual technique is observed. It is shown that GA can fully exploit the complexed interaction between the two techniques in maximizing their overall performance under the four assumed interaction scenarios.

Generally speaking, due to the robustness and wide applicability of GA, the proposed approach can be well applied to many other design optimization problems, where FEM simulation plays a key role in evaluating the performance of candidate designs.

In addition, this method can also be used as a parameter fitting technique for the FEM model calibration. Here, the deviation between the predicted values from simulations and the experimentally observed ones is taken as the objective to be minimized and the parameters of the FEM model, which are to be calibrated, are taken as the design variables. An example of this has been shown in the fitting of inherent strain in section 5.6.1.

To facilitate the application of this approach for potential users, the author would like to provide a generalized paradigm of the process as shown in Figure 5.28 together with some key recommendations for a cost-effective optimization in following paragraphs.

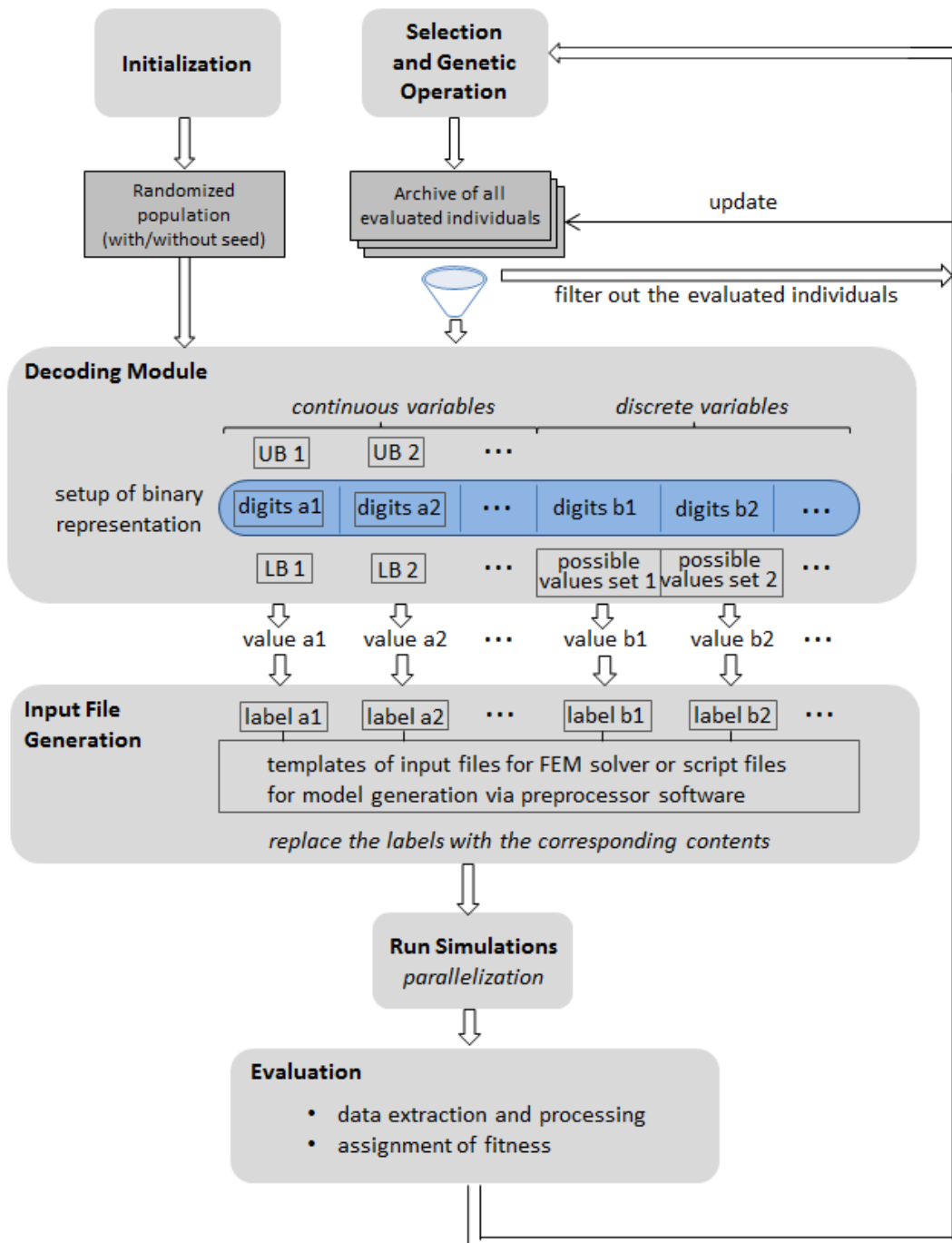


Figure 5.28. The generalized flowchart for the FEM-GA coupled optimization, which contains a series of continuous design variables  $a_1, a_2, \dots$  and discrete design variables  $b_1, b_2, \dots$ . UB and LB represent the upper and lower boundaries of the range of a continuous variable. Each description bordered by a box in the modules for decoding and input file generation (such as UB1, UB2, label a1 and label a2) denotes a piece of information that needs to be provided by the user.

As shown in Figure 5.28 the two most import steps for performing a FEM-GA coupled optimization are the setting-up of the representation scheme for candidate solutions and the automated generation of input files for simulations.

Herein, binary representation is recommended for the following three reasons. Firstly it can maximize the number of schemata per bit of information according to Goldberg [55] and thus can potentially enhance the efficiency of the optimization. Secondly, it enables the application of standard genetic operators, which are most extensively tested and most well understood in their performance. Thirdly, it can easily incorporate different types of design variables, which can be either continuous or discrete in nature, in one chromosome without the need of designing specialized genetic operators.

The setting up of the binary representation scheme for a specific optimization task can be facilitated by using an universal decoding module, which can, based on a few inputs from user, automatically establish a mapping from all genotypes to all candidate solutions that are uniformly distributed through the search space. As shown in Figure 5.28, all the design variables for a FEM-GA coupled optimization can have either a continuous or a discrete nature. For a continuous variable, the user needs to set the number of digits ( $l$ ) for its binary representation together with the upper and lower boundaries of its range. Then the decoding module automatically assigns  $l$  alleles at a specific location of the chromosome for this variable, which can represent  $2^l$  different values from the minimum to the maximum as specified in section 5.2.2. For a discrete variable, the user only needs to input a list of all its possible values. Then, the decoding module will determine the number of alleles  $l$  for this variable based on the criterion  $2^{l-1} < N_{\text{values}} \leq 2^l$ , where  $N_{\text{values}}$  is the number of entries in the list of values that has been given. Since  $N_{\text{values}}$  mostly dose not equal  $2^n$  ( $n$  is an integer), some possible values of the discrete variable need to have two different binary representations. Then the allocation of these redundant representations will be handled by the decoding module such that the pair of representations corresponding to the same phenotypic value are also neighbours in the genotypic space. This can ensure the proper functioning of the genetic operators according to the concept of synonymous redundancy by Rothlauf [115]. After setting up all the continuous and discrete variables, the representation scheme for the optimization problem has been automatically established. Since there is no need to pay special attention to the details of the representation, significant human efforts can be saved by applying such an universal decoding module as depicted in Figure 5.28.

The second important part of the FEM-GA coupled optimization is the automated generation of input files of FEM models for each candidate solution. This can be achieved by the text-replacement performed on a template input file as shown in Figure 5.28, in which special labels for each design variable are placed at the respective locations, where their values should appear. As shown in Figure 5.28, after the values of all design variables are decoded from the genotype by the decoding module, they will replace the corresponding labels in the template file to form the FEM input file of the candidate solution. Alternatively, a script file, which can interact with the FEM preprocessor such as ABAQUS/-CAE via a scripting interface to create and modify FEM models, can also be

used as a template. This approach enables a much more flexible parameterization of FEM models compared to the first approach. In principle, any parameters (numerical/non-numerical) or even blocks of text that appear in the script file describing the features of the FEM model can be taken as design variables in the FEM-GA coupled optimization.

Since each FEM simulation itself during the optimization can be very time consuming, measures need to be taken to make the whole process more time-efficient. First of all, a parallelization of simulation tasks can be performed if multiple processors are available. As mentioned in section 5.2.5 the user is recommended to use the programming language Python to organize the optimization process, the modules of which, like Threading, Multiprocessing and Scoop [116], can provide a very convenient and efficient parallelization of computational tasks on various environments from computer clusters to heterogeneous grids. Secondly, the user is recommended to establish an external archive to store all the candidate solutions that have been evaluated together with their fitness values as shown in Figure 5.28. By comparing the newly evolved population each generation with this archive, repeated simulation runs with the same candidate design can be avoided. This can save considerable computational cost as demonstrated in section 5.4.

Thirdly, for the optimization problem involving mainly continuous design variables, the user is recommended to encode each continuous design variable with as few alleles as possible. Take the encoding of the thickness of crenellated panels in this study as an example, only 3 alleles per variable can already provide sufficiently good results as shown in section 5.3. The accompanying shorter genes on chromosomes can reduce the orders of schemata, which facilitate the building blocks to propagate properly in subsequent populations and thus enhance the performance of GA according to Rothlauf [56]. In addition, the shorter total length of the chromosome also allows the use of a smaller population (e.g. 20 individuals) [98], which can lead to a more efficient convergence [117].

With a coarse discretization of search space, normally the user can already obtain a rather good solution that is close to the global optimum. However, it is also possible that the GA search converges towards a local optimum if the narrow peak of the global optimum on fitness landscape just situates at one mesh hole of the discretized search space. Due to this reason, a second refined search can be performed to verify the previously obtained result, where each variable is encoded by more alleles. In this stage, the optimized result of the previous stage is put as seed in the initial population of the refined search, which is relatively larger in size (e.g. 30 individuals). The seed solution is expected to be further improved in this refined search. As shown in section 5.4, such progressive refined search should be more computational efficient than the direct refined search due to the nature of GA to sequentially solve alleles based on their salience and due to the accelerated convergence by seeding in the refined search.

To perform this progressive refined search in the most cost-efficient way, it is important to switch to the refined stage at the correct time point. As presented in the characteristic curve of a GA search (Figure 5.29), which shows the increase of the fitness value with increasing number of evaluations, the most significant fitness improvement usually occurs in the first few generations. Then it is fol-

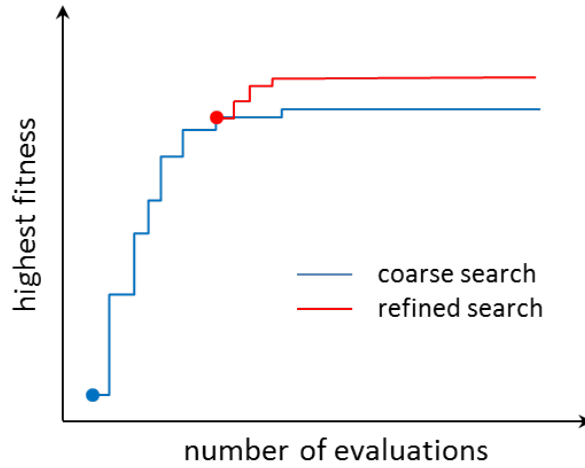


Figure 5.29. Typical trend of fitness increase with increasing number of evaluations and the proper time point for starting refined search.

lowed by a slow finishing, where much more computational cost leads to only little improvement in fitness values. Thus, the refined search should be started as the coarse search is about to enter the stage of the slow finishing. Since the slow finishing is due to the largely converged state of the population according to Beasley et al. [113], the number of evaluations per generation can be used as a signaling parameter to trigger the refined search. Because the stabilization of this value around a level related with mutation rate is considered as indication of a largely converged population as explained in section 5.4.

Finally, the user is encouraged to include more potentially influential factors in the candidate solutions, which can contribute to the overall performance (e.g. a different fatigue retardation technique as introduced in section 5.6). The collaborative interactions between different factors, which are maximized in the optimization, can lead to considerable additional fitness improvement as demonstrated in section 5.6.3.

The detailed approach of such a FEM-GA coupled optimization and the related recommendations specified above are expected to make full use of the intrinsic advantages of GA in terms of its simplicity, wide applicability, robustness and parallelism, and meanwhile to avoid shortcomings in terms of the need of designing problem-specific representations and the large computational cost.

## 6. Conclusion

This study addresses the possibility of further improving the fatigue performance of crenellated airframe structures through both a material approach and a geometric optimization approach.

In the material approach, two distinct candidate Al alloys for fuselage skin applications, that is AA2139 and AA2198, were tested with the same crenellation geometries. The fatigue life improvement by crenellation is found unexpectedly higher in the Al-Li alloy AA2198 with sharp deformation texture compared to that in the non-textured Al-Cu alloy AA2139. The additional fatigue life improvement in the AA2198 specimens is attributed to the extensive formation of rough shear lips especially when crenellations are present and to the resulting enhanced crack closure level.

The formation of the sharp shear lips in AA2198 has its origin in the intrinsic tendency of slip planarity of Al-Li alloy and especially in the sharp deformation texture resulting from the T3 heat treatment condition. The weak grain boundaries due to the strong texture favor a fast propagation of shear mode decohesion along the common  $\{111\}$  planes across different grains, from the initiation sites at the surface towards interior of the specimen. This leads to abrupt changes of cracking plane orientations at the macroscopic scale and thus to a rather rough crack surface morphology. In contrast, the distinct misorientations between adjacent grains in AA2139 confines the zones of shear mode decohesion in a shallow stripe near the surface and in isolated islands of grains in the interior of the specimens, where the grains probably have the most favorable crystallographic orientations. This results in a very smooth transition from the tensile mode to shear mode decohesion and a macroscopically flat fracture surface.

In addition, due to the locally enhanced plane stress condition at the side of the crenellation, the formation of sharp shear lips in the AA2198 crenellated specimen is promoted along the crenellation side of the fracture surfaces, especially at the crenellation steps. The enhanced plane stress condition also enables a much earlier formation of shear lips compared to the flat specimen. This promotes a more pronounced wedging of crack surfaces at those asperities of the rough shear lips, especially when the anti-plane movement of the crenellated panel under biaxial loads induces mode III displacements of crack surfaces. Such wedging can occur at a large crack opening displacement and at a considerable distance from crack tip because of the large asperity size (in the order of millimeter) and the increasing crack surface mismatch away from the crack tip. This leads to the observed enhanced crack closure level in the AA2198 crenellated specimen, which covers a broad span of  $\Delta K$  in Paris region, and thus to a significant additional extension

of fatigue crack growth life.

In the second part of the work for optimizing crenellation geometry, an automated optimization approach by coupling FEM simulation with genetic algorithm was developed. The evolved optimized designs by this approach show that the crenellation pattern with stepwise increase of thickness from the roots of stringers towards the center of each bay has the longest fatigue life. This is verified by multiple runs of optimizations with different refinements of the search space discretization as well as by using a multi-objective optimization approach, in which the imposed constant-weight constraint is released. It is also experimentally validated that the optimized design can indeed significantly improve the fatigue performance of crenellated structures (15% longer fatigue life at a final half crack length of 120 mm) as it is expected from the FEM simulations.

The study also demonstrates that the computational cost of FEM-GA coupled optimization can be significantly reduced by applying the duplicate individual filtering (DIF) technique and a progressive refinement of the search space. Instead of having a nearly constant number of evaluations per generation ( $N_{eva}$ ) determined by the crossover rate, the application of DIF technique leads to a continuous decrease of  $N_{eva}$  with increasing number of generations until it reaches a much lower value related with the mutation rate. This leads to a considerable saving of computational cost.

In addition, an efficient GA-FEM coupled optimization also relies on a proper refinement of the search space. It has been shown that the search dynamics of GA tends to solve the alleles in descending sequence according to their salience. With a very fine discretization of the search space (longer chromosome), the alleles with lowest salience can hardly be reached by the selection pressure and are usually randomly fixed due to the loss of genetic diversity in the end. Therefore, it is better to firstly perform a coarse search (shorter chromosome), which can arrive at full convergence efficiently in a few generations, and then to put the optimized result as seed in the initial population of the subsequent refined search. The seed can significantly accelerate the convergence in the refined search and meanwhile can lead to improved quality of the final solution due to the exposure of low salient alleles to the selection pressure. It is expected that a combined application of both methods can lead to a more cost-effective optimization.

Finally, the same approach has been applied to exploit the possible cooperative interaction between crenellation and another fatigue crack retardation technique named laser heating when they are used in a combined way. Four different scenarios about the damping of the introduced inherent strain in the heated zone with increasing local thickness are assumed. It has been shown that the FEM-GA coupled optimization can effectively explore the positive interaction and meanwhile avoid disruptive interaction under the four scenarios with different extent of epistasis. The optimized designs lead to significantly higher overall fatigue life improvement even compared to the linear superimposition of each individual improvement, especially when the damping coefficient  $M$  is smaller than 0.4.

## A. Python scripts for the FEM-GA coupled optimization

The python scripts for the FEM-GA coupled optimization contains three parts: "main.py", "grow.py" and "k\_values.py". "main.py" is the main body of the routine, which involves the representation scheme, GA parameters, parallization of jobs, assignment of fitness value and recording of the evolution history. "grow.py" is the specialized subroutine called by "main.py" for the automated generation of FEM models and execution of simulations. "k\_values.py" is another specialized subroutine for extracting useful data from the results files of FEM simulation.

### A.1 main.py

```
#!/usr/bin/python
from pylab import *
from deap import base, creator, tools, algorithms
from scipy import interpolate
import pickle
from os import system, access
from time import sleep
import glob
from Queue import Queue, Empty
from threading import Thread
from random import randint

indList = Queue() # set up the queue for parallization of jobs
Nind=20           # number of individuals in the population
NGEN=40          # maximum number of generations
CXPB = 0.5       # crossover rate
MUTPB = 0.2      # mutation rate at individual level
Glength = 19     # number of digits in the genotype of an individual
digits = 3       # number of digits representing the thickness of a
                  # section
ths = 1          # number of threads
s = Glength

# see detailed explanation of base, creator and toolbox method
# in DEAP documentation:
creator.create("FitnessMax", base.Fitness, weights=(1.0,))
```

---

```

toolbox = base.Toolbox()
# attribute generator:
toolbox.register("attr_bool", randint, 0, 1)
# randomly generate the genotype:
toolbox.register("get_indi", tools.initRepeat, creator.Individual,
                toolbox.attr_bool, Glength)

# setting up important GA parameters:
toolbox.register("mate", tools.cxOnePoint)
toolbox.register("mutate", tools.mutFlipBit, indpb=0.2)
toolbox.register("select", tools.selTournament, tournsize=3)

def cleanup():
    """Delete the files that are generated from simulation."""

    Ext = ['prt', 'msg', 'sta', 'com', 'sim', 'odb',
          'inp', 'dat', 'log']
    for ext in Ext:
        cmd = "rm -f *.%s" % ext
        system(cmd)

def individual_():
    """ The method to randomly generate a genotype."""

    individual = toolbox.get_indi()
    return individual

def population_(n):
    """The method to generate a randomized population with no duplication."""

    pop = []
    for i in range(n):
        if i == 0:
            pop.append(individual_())
        else:
            new = individual_()
            # if "new" has appeared, regenerate "new":
            flag = 0
            for ind in pop:
                if ind[:s] == new[:s]:
                    flag = 1
            while flag:
                new = individual_()
                flag = 0

```

```
        for ind in pop:
            if ind[:s] == new[:s]:
                flag = 1
        pop.append(new)
    return pop

# register the two methods in toolbox:
toolbox.register("individual", individual_)
toolbox.register("population", population_)

def grow(List):
    """Automated generation of FEM models
    and execution of simulations."""

    # get the queue of jobs for parallization:
    global indList

    # execute jobs until the queue is empty:
    while True:
        try:
            job=indList.get(block=False)
        except Empty:
            break
        else:
            # define the name in the form:
            # "index of generation_" "index of individual":
            name = "%d_%d" % (job[1], job[2])
            thickness = decoder(job[0])
            flag2 = 0
            count = 0
            # check if this individual has been evaluated:
            in this generation:
            for ind in List[:job[2]]:
                if ind == job[0]:
                    flag2=1
                    break
                else: count+=1

            # if it has been evaluated,
            # directly copy the extracted K profile:
            if flag2:
                while not os.access(sta_file_name, os.R_OK):
                    sleep(1)
                sleep(10)
                cmd = "cp K_values_%d_%d.txt K_values_%s.txt" \
```

```

        % (job[1], count, name)
        system(cmd)
    else:
        # call the subroutine grow.py to
        # generate FEM model and to run the simulation:
        print "start growing %s" % name
        cmd = "python grow.py"
        for t in thickness:
            cmd += ' %s' % str(t)
        cmd += ' %s' % name
        print "submitting job: %s" % cmd
        system(cmd)

def getN(gen,index,c_, m_):
    """Calculated the fatigue life
    based on the extracted K profile."""

    name = "%d_%d" % (gen, index)
    filename = 'K_values_' + name + '.txt'
    data = loadtxt(filename)
    a = data[:,0]
    K = data[:, -1]*0.001**0.5
    dadN = c_*(K)**m_
    dN = 1/dadN
    x_new = np.linspace(6, 145, 10000)
    tck = interpolate.splrep(a, dN)
    dN_new = interpolate.splev(x_new, tck)
    # integration dN/da over a from 6 mm to 145 mm:
    N = np.trapz(dN_new, x_new)
    return (N, )

def decoder(individual):
    """Decode the genotype into a list of thicknesses
    of different sections."""

    global digits, scheme
    # decode binary genotype firstly into a set of integers:
    gene = individual[:-4]
    integers = []
    for i in range((len(individual)-4)/digits):
        j = 0
        inte = 0
        while j < digits:
            inte += gene[i* digits+j]*2**(digits-j-1)

```

```
        j += 1
    integers.append(inte)

# decode the set of integers into the set of thickness values
# considering both the boundaries
# and constant weight constraints:
thickness = []
for inte in integers:
    thickness.append(1.9+inte/7.0*2.25)
M = 2.9*len(thickness)
tot = sum(thickness)
# small compensation term "com" added to each thickness section
# to maintain constant weight:
com = (M - tot)/len(thickness)
for t in range(len(thickness)):
    thickness[t] += com
while True:
    flag = 0
    i=0
    for t in thickness:
        if t < 1.899999:
            comp = 1.9-t
            for j in range(len(thickness)):
                if j != i:
                    thickness[j] -= comp/(len(thickness)-1)
            thickness[i] = 1.9

            flag =1
        elif t > 4.150001:
            comp = t - 4.15
            for j in range(len(thickness)):
                if j != i:
                    thickness[j] += comp/(len(thickness)-1)
            thickness[i] = 4.15
            flag =1
    i+=1
    if flag==0:
        break
return thickness

def history(pop, append = True):
    """Record the present generation and its relevant statistics
    in a plain text file."""

    # gather all the fitnesses and phenotypes in one list:
```

```

fits = [ind.fitness.values[0] for ind in pop]
thicknesses = [decoder(ind) for ind in pop]
final = [i+[j] for i, j in zip(thicknesses, fits)]
savetxt("life_Gen%d.txt" % initGEN, array(final))

# produce the statistic report:
length = len(pop)
mean = sum(fits) / length
sum2 = sum(x*x for x in fits)
std = abs(sum2 / length - mean**2)**0.5
ind = [i for i, j in enumerate(fits) if j==max(fits)]
fittest = pop[ind[0]]
if append:
    history = open("history.txt", 'a')
else:
    history = open("history.txt", 'w')
print >> history, "==== Generation %d results =====" \
% initGEN
print >> history, "  Min %s" % min(fits)
print >> history, "  Max %s" % max(fits)
print >> history, "  Avg %s" % mean
print >> history, "  Std %s" % std
print >> history, "genotype of fittest individual: %s" \
% fittest
print >> history, "phenotype of fittest individual: %s" \
% decoder(fittest)
history.close()

def parallization(work):
    """ Parallilization of jobs."""

    workers = [Thread(target=grow, args=(work,))
for i in range(ths)]
    for worker in workers:
        worker.start()
    for worker in workers:
        worker.join()

def main(restart = False, elitism = True):
    """ The main routine to perform FEM-GA coupled optimization.
    restart: to restart the optimization from a broken point,
    elitism: the switch on/off of the elitism in the optimization.
    """

```

---

```

initGEN = 0    # index of initial generation
if restart:
    clearup()
    # load the archive for evaluated individuals:
    f = open("valid_ind.txt" , 'rb')
    valid_ind = pickle.load(f)
    f.close()
    # list of files containing all the genotypes
    # in the beginning of each generation:
    nameListOff = glob.glob("offspring_Gen_*.txt")
    # list of files containing all the genotypes and
    # their fitnesses at the end of each generation:
    nameListPop = glob.glob("population_Gen_*.txt")
    a = max([int(i[14:-4]) for i in nameListOff])
    b = max([int(i[15:-4]) for i in nameListPop])
    if b < a:
        initGEN = a
        print "restart at generation %d " % initGEN
        f = open("offspring_Gen_%d.txt" % initGEN, 'rb')
        offspring = pickle.load(f)
        f.close()
        # only evaluate the individuals
        # with an invalid fitness value:
        invalid_ind = [ind for ind in offspring
                       if not ind.fitness.valid]

        # filter out the individuals that have been validated
        # according to the achive of all evaluated individuals:
        for indin in invalid_ind:
            for indv in valid_ind:
                if indin == indv:
                    indin.fitness.values = indv.fitness.values
        invalid_ind = [ind for ind in invalid_ind
                       if not ind.fitness.valid]

        # calculate the fitness values for the individuals,
        # the simulations of which have been performed:
        Klist = glob.glob("K_values_%d*.txt" % initGEN)
        finish_n = max([int(i[len("K_values_%d_" % initGEN):-4])
                        for i in Klist])
        for index in range(0, finish_n+1):
            invalid_ind[index].fitness.values= \
                getN(initGEN, index, 4e-7, 2.4)
            valid_ind.append(invalid_ind[index])

        # execute the FEM simulations

```

---

```

# for the rest of population in multiple threads:
rest = range(finish_n+1, Nind)
if rest:
    for index in rest:
        indList.put([invalid_ind[index],
                    initGEN, index])
parallization(invalid_ind)
for index in rest:
    invalid_ind[index].fitness.values= \
    getN(initGEN, index, 4e-7, 2.4)
    valid_ind.append(invalid_ind[index])

# replace the old population with
# the newly evolved population:
pop[:]=offspring
# pickle all the genotypes and
# the corresponding fitness values of the population:
f = open("population_Gen_%d.txt" % initGEN, 'wb')
pickle.dump(pop, f)
f.close()
history(pop)
initGEN = initGEN+1
clearup()
else:
    f = open("population_Gen_%d.txt" % b, 'rb')
    pop = pickle.load(f)
    f.close()
    initGEN += 1

for g in range(initGEN,NGEN):
    if g==0:
        print "starting generation %d." % g
        #randomly generate the initial population:
        pop = toolbox.population(n=Nind)
        valid_ind = []
        # pickle the state of the population
        # in the beginning of the generation:
        f = open("offspring_Gen_0.txt", 'wb')
        pickle.dump(pop, f)
        f.close()
        offspring = pop
        print "start Gen %d" %g
        for index in range(Nind):
            indList.put([offspring[index], g, index])
        parallilization(offspring)

```

```

fitnesses = [getN(g, index, 4e-7, 2.4)
              for index in range(Nind)]
for ind, fit in zip(offspring, fitnesses):
    ind.fitness.values = fit
    valid_ind.append(ind)
f = open("population_Gen_%d.txt" % g, 'wb')
pickle.dump(offspring, f)
f.close()
pop[:] = offspring
fittest = history(pop, append=false)

else:
    print "Generation %d is being generated..." % g
    # perform selection based on fitness:
    offspring = toolbox.select(pop, len(pop))
    # clone the selected individuals:
    offspring = list(map(toolbox.clone, offspring))

    # apply crossover and mutation on the offspring:
    for child1, child2 in zip(offspring[::2], \
                              offspring[1::2]):
        if random() < CXPB:
            toolbox.mate(child1, child2)
            del child1.fitness.values
            del child2.fitness.values
    for mutant in offspring:
        if random() < MUTPB:
            toolbox.mutate(mutant)
            del mutant.fitness.values

    f = open("offspring_Gen_%d.txt" % g, 'wb')
    pickle.dump(offspring, f)
    f.close()
    if elitism:
        if fittest not in offspring:
            offspring[0] = fittest
    invalid_ind = [ind for ind in offspring
                   if not ind.fitness.valid]
    for indin in invalid_ind:
        for indv in valid_ind:
            if indin == indv:
                indin.fitness.values = indv.fitness.values
    invalid_ind = [ind for ind in invalid_ind
                   if not ind.fitness.valid]
    for index, ind in enumerate(invalid_ind):

```

```

        indList.put([ind, g, index])
    parallilization(invalid_ind)
    fitnesses = [getN(g, index, 4e-7, 2.4)
                  for index in range(len(invalid_ind))]
    for ind, fit in zip(invalid_ind, fitnesses):
        ind.fitness.values = fit
        valid_ind.append(ind)
    pop[:] = offspring
    f = open("population_Gen_%d.txt" % g, 'wb')
    pickle.dump(pop, f)
    f.close()
    fittest = history(pop)
clearup()

# update the achive for evaluated individuals:
f = open("valid_ind.txt" , 'wb')
pickle.dump(valid_ind,f)
f.close()

if __name__ == "__main__":
    main(restart=0)

```

## A.2 grow.py

```

#!/usr/bin/python
from os import access, system, R_OK
import sys
from odbAccess import *
from time import sleep
import math
import numpy as np
from sys import argv
from Queue import Queue, Empty
from threading import Thread

# positions of borders between different thickness sections:
Cs = [19,33,47,61,75,89,103,117,131]
Nworker = 2          # number of threads
joblist = Queue()    # set up the queue for parallization of jobs

# receive the thickness values passed from main.py:
thickness = [float(a) for a in argv[1:-1]]
name = argv[-1]

L0 = 6 #mm                initial crack length
Ltot = 145 #mm            final crack length
steps = (Ltot-L0)/2+1 #   number of increments

```

```

def getAllNodes():
    """ Get the list of all nodes in the model.
        Each Node in the list has the format:
        ["node label", "x coordinate", "y coordinate"].
    """

    f = open('other/model.inp', 'r')
    allnode = []
    flag = 0
    for line in f.readlines():
        data = line.split()
        if data[0] == '*Node':
            flag = 1
            continue
        if flag:
            if data[0][0] != '*':
                allnode.append([float(i) for i in line.split(',')])
            else: break
    f.close()
    return allnode

def bonded(L0, Nlist):
    """ Get the label lists of nodes located on the crack line.
        L0 is the initial crack length.
        Nlist is the list of all nodes.
    """
    tol = 0.01
    NodeBonded = [] # all the nodes along the crack line
    NodeLabelBonded= [] # label of all the nodes on the crack line
    for N in Nlist:
        if fabs(N[2]) < tol:
            if N[1] > L0-1 - tol:
                NodeBonded.append(N)
    # sort the node list according to the x coordinate:
    NodeBonded = NodeBonded.sort(key=lambda x: x[1])
    NodeLabelBonded = [int(i[0]) for i in NodeBonded]
    return NodeLabelBonded

def ABQinp(bondedSet,pretip, jobName, name):
    "Prepare input file for simulation"

    symmynodes = ' '

```

```

for i in bondedSet:
    if ind%8 == 0:
        symmynodes += str(i)+ ',\n'
    else:
        symmynodes += str(i)+ ', '
f = open(jobName+'.inp', 'w')
model = open(name+'.inp', 'r')
lines = model.readlines()
for line in lines:
    print >> f, line.replace('symmynodes', symmynodes)\
        .replace('pretipnode', str(pretip))\
        .replace('tipnode', str(bondedSet[0])),
f.close()

def runSim(i):
    """ Run the simulation jobs that has been put into the queue. """

    global joblist
    while True:
        try:
            jobName=joblist.get(block=False)
        except Empty:
            break
        else:
            if not access("%s_min.odb" % jobName, R_OK):
                cmd = 'abaqus job='+jobName+' interactive'
                system(cmd)

def growup(name):
    """ Run the series of simulation jobs with the crack
        incrementally extending from an initial length to
        a final length. And extract the stress intensity
        factor profile from the result files of the simulations.
    """

    # prepare to write the common input file
    # for the series of simulation:
    f = open(name+'.inp', 'w')
    # read the content from the template of the input file:
    model = open('other/model.inp', 'r')
    lines = model.readlines()

    # write the thicknesses of the crenellation pattern
    # into corresponding positions of input file:

```

```

markers = ['th%d' % n for n in range(1,len(thickness)+1)]
for line in lines:
    for t, marker in zip(thickness, markers):
        line = line.replace(marker, str(t))
    print >> f, line,
f.close()

allnode = getAllNodes()
bondedset = bonded(L0, allnode)

# the crack extends with an increment of 2 mm,
# and if the crack tip is in the area near the crenellation steps
# the increment is reduced to 1 mm
# due to the sharp change of K values locally:
count = 0
for L in range(L0, Ltot+1):
    jobName = "%s_Crack%d" % (name, L)
    formertip = bondedset.pop(0)
    if count == 0 and L%2 == 0:
        for C in Cs:
            if C - L == 1:
                count = 2
            if C - L == 2:
                count = 4
    if count or L%2 == 0:
        ABQinp(bondedset, formertip, jobName, name)
        joblist.put(jobName)
        if count != 0:
            count -= 1
# parallization of simulations:
workers = [Thread(target=runSim, args = (i,))
           for i in range(Nworker)]
for worker in workers:
    worker.start()
for worker in workers:
    worker.join()

# check if the last simulation job is finished:
sta_file_name = '%s_Crack144.sta' % name
while not access(sta_file_name, R_OK):
    sleep(1)

# extracting K values from the result files
# by calling subroutine K_values.py:
print "start extracting Ks for %s" % name

```

```

cmd = "abaqus python getKs.py"
for t in thickness:
    cmd += ' %s' % str(t)
cmd += ' %s' % name
system(cmd)

```

```
growup(name)
```

### A.3 k\_values.py

```

#!/usr/bin/python
from os import access
import sys
from odbAccess import *
from time import sleep
import math
from numpy import *
from sys import argv
from grow import getAllNodes, bonded, Cs, L0, Ltot

steps = (Ltot-L0)/2+1
thickness =[float(i) for i in argv[1:-1]]
name = argv[-1]

def getF( jobName):
    """ Extract the reaction force at crack tip
    from the result file."""

    name = jobName + '.odb'
    odb = openOdb(name)
    F = fabs(odb.steps['Load'].frames[-1].fieldOutputs['RF']
            .values[0].data[1])
    return F

def getU(jobName,formertip):
    """ Extract node displacement after the crack tip
    from the result file."""

    name = jobName + '.odb'
    odb = openOdb(name)
    for node in odb.steps['Load'].frames[-1]\
            .fieldOutputs['U'].values:
        if node.nodeLabel==formertip:

```

```

        U = fabs(node.data[1])
    return U

def G(NodeF, NodeDisp, L):
    """ Calculate the energy releasing rate."""

    global Cs, thickness
    # determine the local thickness at the crack tip:
    i = 0
    for C in Cs:
        if L < C:
            break
        else:
            i += 1
    th = list(thickness)
    Ns = len(thickness)
    for n in range(Ns):
        th.append(thickness[Ns-1-n])
    t = th[i]
    G = NodeF*NodeDisp/t
    return G

def K(G):
    """ Calculate the stress intensity factor."""

    K = (G*72400)**0.5
    return K

allnode = getAllNodes
bondedset = bonded(L0, allnode)

K_values = open('K_values_%s.txt' % name, 'w')
count = 0
for L in range(L0, Ltot+1):
    jobName = "%s_Crack%d" % (name, L)
    formertip = bondedset.pop(0)
    if count == 0 and L%2 == 0:
        for C in Cs:
            if C - L == 1:
                count = 2
            if C - L == 2:
                count = 4
    if count or L%2 == 0:
        if count != 0:

```

```
        count -= 1
    NodeDisp = getU(jobName, formertip)

    print >> K_values, "%10.6f" % L,
    NodeF     = getF(jobName)
    print >> K_values, "%12.6f" % NodeF,
    print >> K_values, "%12.6f" % NodeDisp,
    G_VCCT = G(NodeF, NodeDisp,L)
    K_VCCT = K(G_VCCT)
    print >> K_values, "%12.6f" % G_VCCT,
    print >> K_values, "%12.6f" % K_VCCT

K_values.close()
```

## Bibliography

- [1] S. K. Bhaumik, M. Sujata, and M. A. Venkataswamy. Fatigue failure of aircraft components. *Engineering Failure Analysis*, 15(6):675–694, 2008.
- [2] U. G. Goranson. Damage tolerance - facts and fiction. In *Keynote presentation in 1st International Conference on Damage Tolerance of Aircraft Structures*. Delft Technical University, 2007.
- [3] J. C. Ehrström, S. Van der Veen, S. Arsène, and R. Muzzolini. Improving damage tolerance of integrally machined panels. In *Proc. 23rd Symposium of International Committee on Aeronautical Fatigue, ICAF 2005*, pages 79–90, 2005.
- [4] R. Muzzolini and J. C. Ehrstrom. Damage tolerance of integral structures with crack retardation features. In *Proceedings of the 15th Advanced Aerospace Materials & Processes Conference and Exposition AeroMat, Seattle*, 2005.
- [5] R. J. Bucci. Advanced metallic and hybrid structural concepts. In *Proceedings of Aircraft Structural Integrity Program Conference, San Antonio*, 2006.
- [6] J. C. Ehrström, R. Muzzolini, S. Arsene, and S. Van der Veen. Buckling and post-buckling of sub-stiffened or locally tailored aluminum panels. In *Proceedings of the 23rd Symposium of the International Committee on Aeronautical Fatigue, Hamburg*, 2007.
- [7] M. V. Uz, M. Kocak, F. Lemaitre, J. C. Ehrström, S. Kempa, and F. Bron. Improvement of damage tolerance of laser beam welded stiffened panels for airframes via local engineering. *International Journal of Fatigue*, 31(5):916–926, 2009.
- [8] D. Quinn, A. Murphy, and L. Cervi. Fatigue performance of aircraft panels with novel skin buckling containment features. *Proceedings of the institution of mechanical engineers, part G: Journal of Aerospace Engineering*, 225(7):791–806, 2011.
- [9] X. Zhang, M. Boscolo, D. Figueroa-Gordon, G. Allegri, and P. E. Irving. Fail-safe design of integral metallic aircraft structures reinforced by bonded crack retarders. *Engineering Fracture Mechanics*, 76(1):114–133, 2009.

- [10] M. V. Uz. *Improvement of damage tolerance of laser beam welded aerospace structures via local engineering*. PhD thesis, Technischen Universität Hamburg-Harburg, 2010.
- [11] R. J. H. Wanhill. Flight simulation fatigue crack growth guidelines. Technical Report NLR-TP-2001-545, National Aerospace Laboratory NLR, 2001.
- [12] S. Suresh. *Fatigue of materials*. Cambridge university press, 1998.
- [13] T. F. Morgeneyer. *Micromechanical studies and modelling of toughness in high strength aluminium alloys*. PhD thesis, University of Southampton, 2008.
- [14] D. Tsivoulas. *Effects of combined Zr and Mn additions on the microstructure and properties of AA2198 sheet*. PhD thesis, The University of Manchester, Manchester, UK, 2011.
- [15] M. V. Uz, Y. J. Chen, and N. Huber. Fatigue life improvement of metallic aerospace structures via crenellations. In *ICAF 2011 Structural Integrity: Influence of Efficiency and Green Imperatives*, pages 811–826. Springer, 2011.
- [16] D. Steglich, H. Wafai, and J. Besson. Interaction between anisotropic plastic deformation and damage evolution in Al2198 sheet metal. *Engineering Fracture Mechanics*, 77(17):3501–3518, 2010.
- [17] J. Schijve. *Fatigue of Structures and Materials*. Springer, 2009.
- [18] T. H. Lin and S. R. Lin. Micromechanics theory of fatigue crack initiation applied to time-dependent fatigue. In *Fatigue Mechanisms*. ASTM International, 1979.
- [19] J. Pokluda and P. Šandera. *Micromechanisms of fracture and fatigue: in a multi-scale context*. Springer Science & Business Media, 2010.
- [20] S. N. Atluri. *Structural integrity and durability*. Tech Science Press, 1997.
- [21] A. F. Blom, A. Hedlund, W. Zhao, A. Fathulla, B. Weiss, and R. Stickler. Short fatigue crack growth behaviour in Al2024 and Al7475. In *Behavior of Short Fatigue Cracks, Symposium of EGF1*, 1985.
- [22] R. M. N. Pelloux. Mechanisms of formation of ductile fatigue striations. *Transactions of the American Society for Metals*, 62:281–285, 1969.
- [23] R. H. Dodds Jr, T. L. Anderson, and M. T. Kirk. A framework to correlate a/W ratio effects on elastic-plastic fracture toughness. *International Journal of Fracture*, 48(1):1–22, 1991.
- [24] T. L. Anderson. *Fracture mechanics: fundamentals and applications*. CRC press, 2005.

- 
- [25] P. C. Paris, M. P. Gomez, and W. E. Anderson. A rational analytic theory of fatigue. *The trend in engineering*, 13(1):9–14, 1961.
- [26] P. C. Paris and F. Erdogan. A critical analysis of crack propagation laws. *Journal of basic engineering*, 85(4):528–533, 1963.
- [27] D. A. Virkler, B. M. Hillberry, and P. K. Goel. The statistical nature of fatigue crack propagation. *Journal of Engineering Materials and Technology*, 101(2):148–153, 1979.
- [28] R. J. H. Wanhill. Durability analysis using short and long fatigue crack growth data. In *International Conference on Aircraft Damage Assessment and Repair: 1991; Preprints of Papers*, page 100. Institution of Engineers, Australia, 1991.
- [29] J. Rice. Mechanics of crack tip deformation and extension by fatigue. In *Fatigue crack propagation*. ASTM International, 1967.
- [30] K Walker. The effect of stress ratio during crack propagation and fatigue for 2024-T3 and 7075-T6 aluminum. In *Effects of environment and complex load history on fatigue life*. ASTM International, 1970.
- [31] J. Zuidema. *Square and slant fatigue crack growth in Al 2024*. PhD thesis, Delft University of Technology, 1995.
- [32] J. Zuidema, F. Veer, and C. Van Kranenburg. Shear lips on fatigue fracture surfaces of aluminium alloys. *Fatigue and Fracture of Engineering Materials and Structures*, 28:159–167, 2005.
- [33] J. Schijve. Shear lips on fatigue fractures in aluminium alloy sheet material. Technical Report Report LR-287, Delft University of Technology, 1979.
- [34] W. Elber. The significance of fatigue crack closure. In *Damage tolerance in aircraft structures*. ASTM International, 1971.
- [35] R. O. Ritchie. Mechanisms of fatigue crack propagation in metals, ceramics and composites: role of crack tip shielding. *Materials Science and Engineering*, A103:15–28, 1988.
- [36] T. C. Lindley and C. E. Richards. The relevance of crack closure to fatigue crack propagation. *Materials Science and Engineering*, 14(3):281–293, 1974.
- [37] S. Suresh and R. O. Ritchie. A geometric model for fatigue crack closure induced by fracture surface roughness. *Metallurgical and Materials Transactions A*, 13(9):1627–1631, 1982.
- [38] S. Suresh. Fatigue crack deflection and fracture surface contact: micromechanical models. *Metallurgical and Materials Transactions A*, 16(1):249–260, 1985.
-

- [39] R. D. Carter, E. W. Lee, E. A. Starke, and C. J. Beevers. The effect of microstructure and environment on fatigue crack closure of 7475 aluminum alloy. *Metallurgical and Materials Transactions A*, 15(3):555–563, 1984.
- [40] A. K. Vasudevan and S. Suresh. Microstructural effects on quasi-static fracture mechanisms in Al-Li alloys: the role of crack geometry. *Materials Science and Engineering*, 72(1):37–49, 1985.
- [41] G. T. Gray, J. C. Williams, and A. W. Thompson. Roughness-induced crack closure: an explanation for microstructurally sensitive fatigue crack growth. *Metallurgical and Materials Transactions A*, 14(2):421–433, 1983.
- [42] R. Pippan, G. Strobl, H. Kreuzer, and C. Motz. Asymmetric crack wake plasticity—a reason for roughness induced crack closure. *Acta materialia*, 52(15):4493–4502, 2004.
- [43] K. T. V. Rao and R. O. Ritchie. Fatigue of aluminium-lithium alloys. *International materials reviews*, 37(1):153–186, 1992.
- [44] F. Bergner, G. Zouhar, and G. Tempus. The material-dependent variability of fatigue crack growth rates of aluminium alloys in the paris regime. *International journal of fatigue*, 23(5):383–394, 2001.
- [45] N. Kamp, N. Gao, M. J. Starink, and I. Sinclair. Influence of grain structure and slip planarity on fatigue crack growth in low alloying artificially aged 2xxx aluminium alloys. *International journal of fatigue*, 29(5):869–878, 2007.
- [46] K. T. V. Rao, W. Yu, and R. O. Ritchie. Fatigue crack propagation in aluminum-lithium alloy 2090: Part I. long crack behavior. *Metallurgical and Materials Transactions A*, 19(3):549–561, 1988.
- [47] G. R. Yoder, P. S. Pao, M. A. Imam, and L. A. Cooley. Unusual fracture mode in the fatigue of an Al-Li alloy. In *The 7th International Conference on Fracture*, 1989.
- [48] X. J. Wu, W. Wallace, M. D. Raizenne, and A. K. Koul. The orientation dependence of fatigue-crack growth in 8090 Al-Li plate. *Metallurgical and Materials Transactions A*, 25(3):575–588, 1994.
- [49] K. Masubuchi. *Analysis of welded structures: Residual stresses, distortion, and their consequences*. Pergamon Press, 1980.
- [50] M. Sticchi, D Schnubel, N Kashaev, and N Huber. Review of residual stress modification techniques for extending the fatigue life of metallic aircraft components. *Applied Mechanics Reviews*, 67(1):010801, 2015.
- [51] D. Schnubel, M. Horstmann, V. Ventzke, S. Riekehr, P. Staron, T. Fischer, and N. Huber. Retardation of fatigue crack growth in aircraft aluminium alloys via laser heating—experimental proof of concept. *Materials Science and Engineering: A*, 546:8–14, 2012.

- 
- [52] D. Schnubel and N. Huber. Retardation of fatigue crack growth in aircraft aluminium alloys via laser heating—numerical prediction of fatigue crack growth. *Computational Materials Science*, 65:461–469, 2012.
- [53] J. H. Holland. *Adaptation in natural and artificial systems: an introductory analysis with applications to biology, control, and artificial intelligence*. U Michigan Press, 1975.
- [54] K. A. De Jong. *An analysis of the behavior of a class of genetic adaptive systems*. PhD thesis, University of Michigan, Ann Arbor, 1975.
- [55] D. E. Goldberg. *Genetic algorithms in search optimization and machine learning*, volume 412. Addison-wesley Reading Menlo Park, 1989.
- [56] S. N. Rothlauf. *Representations for genetic and evolutionary algorithms*. Springer-Verlag, Berlin, Heidelberg, Netherlands, 2006.
- [57] S. N. Sivanandam and S. N. Deepa. *Introduction to genetic algorithms*. Springer Science & Business Media, 2007.
- [58] K. Deb. Multi-objective optimization using evolutionary algorithms: An introduction. *Multi-objective Evolutionary Optimization for Product Design and Manufacturing*, pages 3–34, 2011.
- [59] D. Beasley, R. R. Martin, and D. R. Bull. An overview of genetic algorithms: Part 1, Fundamentals. *University computing*, 15:58–58, 1993.
- [60] Y. Ahn, J. Park, C. G. Lee, J. W. Kim, and S. Y. Jung. Novel memetic algorithm implemented with GA (genetic algorithm) and MADS (mesh adaptive direct search) for optimal design of electromagnetic system. *IEEE Transactions on Magnetics*, 46(6):1982–1985, 2010.
- [61] Y. S. Ong and A. J. Keane. Meta-Lamarckian learning in memetic algorithms. *Evolutionary Computation*, 8(2):99–110, 2004.
- [62] G. M. Morris, D. S. Goodsell, R. S. Halliday, R. Huey, W. E. Hart, R. K. Belew, and A. J. Olson. Automated docking using a Lamarckian genetic algorithm and an empirical binding free energy function. *Journal of computational chemistry*, 19(14):1639–1662, 1998.
- [63] C. C. Palmer and A. Kershenbaum. Representing trees in genetic algorithms. In *Proceedings of the First IEEE Conference on Evolutionary Computation, Piscataway*, 1994.
- [64] A. Konak, D. W. Coit, and A. E. Smith. Multi-objective optimization using genetic algorithms: A tutorial. *Reliability Engineering & System Safety*, 91(9):992–1007, 2006.
- [65] K. Deb. *Multi-objective optimization using evolutionary algorithms*, volume 16. John Wiley & Sons, 2001.
-

- [66] S. Tiwari, P. Koch, G. Fadel, and K. Deb. Amga: an archive-based micro genetic algorithm for multi-objective optimization. In *Proceedings of the 10th annual conference on Genetic and evolutionary computation*, pages 729–736. ACM, 2008.
- [67] E. Zitzler, M. Laumanns, L. Thiele, E. Zitzler, E. Zitzler, L. Thiele, and L. Thiele. SPEA2: Improving the strength pareto evolutionary algorithm, 2001.
- [68] J. D. Knowles and D. W. Corne. Approximating the nondominated front using the pareto archived evolution strategy. *Evolutionary computation*, 8(2):149–172, 2000.
- [69] D. W. Corne, N. R. Jerram, J. D. Knowles, and M. J. Oates. Pesa-ii: Region-based selection in evolutionary multiobjective optimization. In *Proceedings of the Genetic and Evolutionary Computation Conference (GECCO'2001)*. Citeseer, 2001.
- [70] K. Deb, A. Pratap, S. Agarwal, and T. A. M. T. Meyarivan. A fast and elitist multiobjective genetic algorithm: NSGA-II. *Evolutionary Computation, IEEE Transactions on*, 6(2):182–197, 2002.
- [71] G. Rudolph. Evolutionary search under partially ordered fitness sets. Technical report, Universität Dortmund, 2001.
- [72] E. Zitzler, K. Deb, and L. Thiele. Comparison of multiobjective evolutionary algorithms: Empirical results. *Evolutionary computation*, 8(2):173–195, 2000.
- [73] E. Zitzler and L. Thiele. Multiobjective evolutionary algorithms: a comparative case study and the strength pareto approach. *evolutionary computation, IEEE transactions on*, 3(4):257–271, 1999.
- [74] D. A. Van Veldhuizen and G. B. Lamont. Multiobjective evolutionary algorithms: Analyzing the state-of-the-art. *Evolutionary computation*, 8(2):125–147, 2000.
- [75] N. D. Alexopoulos, E. Migklis, A. Stylianos, and D. Myriounis. Fatigue behavior of the aeronautical Al-Li (2198) aluminum alloy under constant amplitude loading. *International Journal of Fatigue*, 56:95–105, 2013.
- [76] R. Krueger. Virtual crack closure technique: history, approach, and applications. *Applied Mechanics Reviews*, 57(2):109–143, 2004.
- [77] J. Heerens and M. Schoedel. Characterization of stable crack extension in aluminium sheet material using the crack tip opening angle determined optically and by the  $\delta_5$  clip gauge technique. *Engineering Fracture Mechanics*, 76(1):101–113, 2009.

- [78] ASTM Standard. E647, standard test method for measurement of fatigue crack growth rates. *Annual Book of ASTM Standards, Section Three: Metals Test Methods and Analytical Procedures*, 3:628–670, 2002.
- [79] J. Li. *The effect of microstructure and texture on high cycle fatigue properties of Al alloys*. PhD thesis, University of Kentucky, 2007.
- [80] S. Suwas, R. Satyam, and R. Kumar. *Crystallographic Texture of Materials*. Springer, 2014.
- [81] L. P. Pook and A. F. Greenan. Fatigue crack-growth characteristics of two magnesium alloys. *Engineering Fracture Mechanics*, 5(4):935–946, 1973.
- [82] R. M. Tchorzewski and W. B. Hutchinson. Anisotropy of fracture toughness in textured Ti-6Al-4V alloy. *Metallurgical and Materials Transactions A*, 9(8):1113–1124, 1978.
- [83] J. Zuidema and J. P. Krabbe. The effect of regular and irregular shear lips on fatigue crack growth in Al. *Fatigue and Fracture of Engineering Materials and Structures*, 20(10):1413–1422, 1997.
- [84] D. C. Slavik and R. P. Gangloff. Environment and microstructure effects on fatigue crack facet orientation in an Al-Li-Cu-Zr alloy. *Acta materialia*, 44(9):3515–3534, 1996.
- [85] N. E. Prasad, A. A. Gokhale, and R. J. H. Wanhill. *Aluminum-Lithium Alloys: Processing, Properties, and Applications*. Elsevier Inc., 2014.
- [86] N. Kamp, N. Gao, M. J. Starink, M. R. Parry, and I. Sinclair. Analytical modelling of the influence of local mixed mode displacements on roughness induced crack closure. *International journal of fatigue*, 29(5):897–908, 2007.
- [87] Y. Xu, P. J. Gregson, and I. Sinclair. Dispersoid and grain size effects on fatigue crack growth in AA2024-type alloys. In *Materials science forum*, volume 331, pages 1525–1530. Trans Tech Publ, 2000.
- [88] E. Wolf. Fatigue crack closure under cyclic tension. *Engineering Fracture Mechanics*, 2(1):37–45, 1970.
- [89] A. J. McEvily. Current aspects of fatigue. *Metal Science*, 11(8):274–284, 1977.
- [90] H. L. Ewalds and R. T. Furnée. Crack closure measurements along the fatigue crack front of center cracked specimens. *International Journal of Fracture*, 14:R53–R55, 1978.
- [91] R. M. Kemp. Fatigue crack closure—a review. Technical Report 90046, Royal Aerospace Establishment of United Kingdom, 1990.
- [92] J. Schijve. Fatigue crack closure, observations and technical significance. Technical Report Report LR-485, Delft University of Technology, 1986.

- [93] J. D. Frandsen, R. V. Inman, and O. Buck. A comparison of acoustic and strain gauge techniques for crack closure. *International Journal of Fracture*, 11(2):345–348, 1975.
- [94] W. T. Riddell, R. S. Piascik, M. A. Sutton, W. Zhao, S. R. McNeill, and J. D. Helm. Determining fatigue crack opening loads from near-crack tip displacement measurements. *ASTM special technical publication*, 1343:157–174, 1999.
- [95] H. Toda, I. Sinclair, J. Y. Buffière, E. Maire, T. Connolley, M. Joyce, K. H. Khor, and P. Gregson. Assessment of the fatigue crack closure phenomenon in damage-tolerant aluminium alloy by in-situ high-resolution synchrotron X-ray microtomography. *Philosophical Magazine*, 83(21):2429–2448, 2003.
- [96] L. P. Borrego, J. M. Costa, S. Silva, and J. M. Ferreira. Microstructure dependent fatigue crack growth in aged hardened aluminium alloys. *International Journal of Fatigue*, 26(12):1321–1331, 2004.
- [97] J. Lu, N. Kashaev, and N. Huber. Damage tolerance improvement of laser beam welded fuselage structures via crenellations. In *The 29th Congress of the International Council of the Aeronautical Science*, 2014.
- [98] J. T. Alander. On optimal population size of genetic algorithms. In *Computer Systems and Software Engineering*, pages 65–70. IEEE, 1992.
- [99] D. E. Goldberg, K. Deb, and J. H. Clack. Genetic algorithms, noise, and the sizing of populations. *Complex Systems*, 6:333–362, 1991.
- [100] F. A. Fortin, D. Rainville, M. A. G. Gardner, M. Parizeau, and C. Gagné. Deap: Evolutionary algorithms made easy. *The Journal of Machine Learning Research*, 13(1):2171–2175, 2012.
- [101] D. Thierens, D. E. Goldberg, and A. G. Pereira. Domino convergence, drift, and the temporal-salience structure of problems. In *Evolutionary Computation Proceedings, 1998*, pages 535–540. IEEE, 1998.
- [102] M. W. Rudnick. *Genetic algorithms and fitness variance with an application to the automated design of artificial neural networks*. PhD thesis, Oregon Graduate Institute of Science and Technology, 1992.
- [103] J. rey Horn. Finite Markov chain analysis of genetic algorithms with niching. *Forrest Science*, 727:110–117, 1993.
- [104] D. E. Goldberg and K. Deb. A comparative analysis of selection schemes used in genetic algorithms. *Foundations of genetic algorithms*, 1:69–93, 1991.
- [105] S. J. Louis and G. J. E. Rawlins. Predicting convergence time for genetic algorithms. *Foundations of Genetic Algorithms*, 2:141–161, 1993.
- [106] Lufthansa. Fuel efficiency at the Lufthansa Group - cutting costs and protecting the environment. Technical report, 2012.

- 
- [107] D. Schnubel. *Laser heating as approach to retard fatigue crack growth in aircraft aluminium structures*. PhD thesis, Hamburg University of Technology, 2012.
- [108] A. Groth, N. Kashaev, and N. Huber. Introducing residual stresses in thin aluminium structures by laser generated temperature fields. In *Proceedings of the 29th Congress of the International Council of the Aeronautical Sciences, St. Petersburg*, 2014.
- [109] A. Groth. personal communication.
- [110] Y. Ueda, H. Murakawa, and N. Ma. *Welding deformation and residual stress prevention*. Elsevier, 2012.
- [111] W. S. Klug and M. R. Cummings. *Concepts of genetics*. Pearson Education, Inc, 2003.
- [112] J. M. Smith. *Evolutionary genetics*. Oxford University Press, 1989.
- [113] D. Beasley, D. R. Bull, and R. R. Martin. An overview of genetic algorithms: Part 2, Research Topics. *University computing*, 15(4):170–181, 1993.
- [114] Y. Davidor. Epistasis variance: Suitability of a representation to genetic algorithms. *Complex Systems*, 4(4):369–383, 1990.
- [115] F. Rothlauf and D. E. Goldberg. Redundant representations in evolutionary computation. *Evolutionary Computation*, 11(4):381–415, 2003.
- [116] Wikipedia. Python SCOOP (software) — wikipedia, the free encyclopedia, 2016. [Online; accessed 6-June-2016].
- [117] G. Abu-Lebdeh and R. F. Benekohal. Convergence variability and population sizing in micro-genetic algorithms. *Computer-Aided Civil and Infrastructure Engineering*, 14(5):321–334, 1999.



# Curriculum vitae

<b>Family name</b>	Lu
<b>Given name</b>	Jin
<b>Nationality</b>	Chinese
<b>Date of birth</b>	April 1 1986
<b>Place of birth</b>	Henan, China

<b>09.1992 - 09.1998</b>	Primary school in Henan
<b>09.1998 - 09.2001</b>	Middle school in Henan
<b>09.2001 - 09.2004</b>	High school in Henan
<b>09.2004 - 09.2008</b>	University of Science and Technology Beijing, Bachelor of Material Physics
<b>09.2008 - 10.2012</b>	RWTH Aachen University, Master of Metallurgical Engineering
<b>10.2012 - present</b>	Helmholtz–Zentrum Geesthacht, PhD student in the Joining and Assessment Department

